2019

Room Temperature Rechargeable Lithium Sulfur Battery

Fang Li
University of Wollongong

UNIVERSITY OF WOLLONGONG

Institute for Superconducting & Electronic Materials

Room Temperature Rechargeable Lithium Sulfur Battery

Fang Li

This thesis is presented as part of the requirements for the

Award of the Degree of Doctor of Philosophy

University of Wollongong

July 2019

CERTIFICATION

I, Fang Li, declare that this thesis, submitted in partial fulfilment of the requirements for the award of Doctor of Philosophy, in the Institute for Superconducting & Electronic Materials (ISEM), Faculty of Engineering, University of Wollongong, NSW, Australia, is original and based wholly on my own work unless otherwise referenced or acknowledged. This thesis has never been submitted for qualifications at any other academic institution.

Fang Li

July 2019

ACKNOWLEDGEMENTS

This thesis work was completed with the support of all the people in the Institute for Superconducting and Electronic Materials (ISEM) at the University of Wollongong in Australia.

Firstly, I would like to express my deepest gratitude to my supervisor, Professor Jia Zhao Wang, for her profound knowledge and professional guidance and supervision, continuous support, great encouragement, and constructive advice throughout my PhD studies. I would like to express my utmost appreciation to my co-supervisor, Professor Hua-kun Liu, for her professional and invaluable suggestions, including on the design and discussion of the experiments and analysis of the results. Furthermore, I wish to express my deeply grateful to Prof. Jun Chen, for his valuable suggestions and guidance during group meetings.

My grateful thanks go to my co-workers, Dr. Mohammad Rejaul Kaiser and Mr. Yuyang Hou, who both spent lots of time on imparting new research techniques and sharing their experience, knowledge, and suggestions during the progress of my research. Special thanks should be given to Dr. Tania Silver for critical reading of manuscripts.

Furthermore, I wish to thanks the staff members and technicians in ISEM for their kind assitance, including Dr. Germanas Pelekis (XRD), Mr. Tony Rome (SEM), Dr. David

Wexler and Dr. Gilberto Casillas Garcia (TEM), Dr. Kosta Konstantinov (BET, TGA/DTA), Dr. Dongqi Shi (XPS), Dr. Xun Xu (Tube furnace) and Dr. Patricia Hayes (Raman spectroscopy). I also would like to thank Mrs. Crystal Login, Mrs. Narelle Badger, Mrs. Joanne George，Mr. Robert Morgan, Mr. Mathew Davis, and Mrs. Candace Gabelish for their help in official and laboratory matters.

Moreover, many thanks to Dr. Lili Liu, Dr. Jun Wang, Dr. Wenbin Luo, Dr. Boyang Ruan, Mr. Haipeng Guo, Mr. Laiwei Hong, Mr. Viet Pham, Mr. Jicheng Jiang, Mr. Zhe Hu, Mr. Chang Wu, Miss Lina Sang, Miss Yuqing Liu, Dr. Hong Gao, Dr. Yunxiao Wang, Mr. Zhixin Tai, Dr. Lanling Zhao, Mr. Qining Fan, Mr. Zhi Zheng, and other staff members and students at ISEM and IPRI for their kindly help and willingness to share knowledge and advices with me during my PhD research.

I would like to express my gratitude to my parents and sisters, who have always stood by me and encouraged me to make progress throughout my life. I would never have gone so far without their selfless dedication. I also want to thank my husband, Mr. Lishuai Ma, for his moral support and warmest solicitude for my life and for always being there whenever I needed him.

Finally, I would like to thank everyone who was important to the success of my PhD study in the University of Wollongong.

ABSTRACT

Lithium-sulfur batteries (Li-S) are regarded as a promising candidate for next-generation energy storage systems due to their high specific capacity (1675 mA h g^{-1}) and energy density (2600 Wh kg^{-1}), as well as the abundance, safety, and low cost of their sulfur materials. Nevertheless, many disadvantages still exist that are hindering the further development of Li-S batteries, such as the insulating nature of the active materials, the dissolution of intermediate products, large volume expansion, and safety concerns related to the lithium metal anode. Therefore, tremendous efforts need to be made to overcome these drawbacks, including designing suitable conductive matrices to improve the utilization of active materials, modifying the separator to suppress the dissolution of intermediates, and synthesizing Li_2S cathode paired with lithium-free anode to avoid the safety concerns. In this thesis, flexible polypyrrole (PPy) film, S-coated PPy nanofibers cathode, PPy modified separator, uniform PPy-coated S/graphene aerogel, Li_2S-PPy composites, and Li_2S coated nitrogen-doped carbon nanofibers have been synthesized and applied in Li-S batteries to improve their capacity and cycling stability.

A free-standing sulfur-polypyrrole cathode and a polypyrrole coated separator were designed for flexible Li-S batteries. The free-standing sulfur-polypyrrole cathode was prepared by directly pasting sulfur coated polypyrrole (S@PPy) nanofiber composite on a flexible and conductive polypyrrole (PPy) film. Compared with carbonaceous matrices, PPy has a strong interaction with polysulfides to mitigate their dissolution, due to its unique chain structure and the lone pair electrons in nitrogen atoms in PPy. In

addition, the as-prepared PPy film not only shows excellent mechanical elasticity, but also possesses a rough surface, which can accommodate the volume expansion, enhance the adhesion of active materials, and further trap the dissolved polysulfides. Due to the synergistic effects provided by PPy flim, the free-standing sulfur-polypyrrole cathode shows better electrochemical performance than the traditional cathode with S@PPy composite coated on Al foil. In order to further improve the cycling stability of Li-S batteries, a PPy coated separator was prepared, which acts as a fishing net to capture polysulfides and alleviate the shuttle effect, leading to a stable cycling performance. Moreover, the PPy layer coated on commercial separator is much lighter than many other free-standing interlayers reported previously. Considering the flexibility of the free-standing sulfur cathode and the PPy coated separator, a soft-packaged flexible Li-S battery based on them has been designed and fabricated to power a device consisting of 24 light emitting diode (LED) light. After repeated bending, the Li-S battery can still maintain good performance, indicating its excellent mechanical flexibility.

A sulfur/graphene aerogel composite coated with a uniform polypyrrole layer has been designed and synthesized *via* the vapor phase deposition method. Compared with carbonaceous materials, the conductive polypyrrole could react with polar lithium polysulfides (LiPSs) *via* the strong interaction between heteroatoms in the polypyrrole and lithium ions in the LiPSs, thus efficiently suppressing the dissolution of the LiPSs and improving the cycling stability. In addition, the vapour phase deposition method shows several advantages over the solution-based chemical deposition method. First, in the vapor phase deposition method, the monomer is applied as a vapor instead of a solution, so that it can easily penetrate into the pores of the sulfur/graphene hydrogel,

resulting in a uniform polypyrrole coating layer. Second, the sulfur/graphene hydrogel will shrink in the deposition process, which can enhance the contact between the sulfur and the conducting agent, and afford short ionic and electronic transport distances, improving the utilization of active materials and the rate capability. As a result, the designed polypyrrole coated sulfur/graphene composite prepared using the vapor phase method delivered a capacity of 698 mA h g^{-1} after 500 cycles with an ultra-slow decay rate of 0.03% per cycle at 0.5 C.

Li_2S-polypyrrole (PPy) hybrids were prepared via a facile and large-scaled ball milling method. By adjusting the ball milling time, Li_2S-PPy composites with 6 h of ball-milling time showed the most suitable morphology, with sub-microsized Li_2S particles uniformly distributed in the PPy nanofibers matrices. The PPy nanofibers could not only improve the electronic conductivity of Li_2S, but also could trap polysulfides to stabilize the cycling performance. In addition, a three-dimensional (3D) carbon paper was applied as a current collector instead of the normal Al foil to increase the loading amount of active materials (~ 3 mg cm^{-2}). The Li_2S-PPy hybrid cathodes showed excellent cycling and rate capability. For further improvement of the cycling stability, a PPy nanofiber coated separator was used to minimize the polysulfide shuttle effect due to the strong Li-N interaction between the N atoms in PPy and the lithium polysulfides. As a result, Li-S battery based on the Li_2S-PPy-6h cathode and the PPy-separator delivered an initial capacity of 885.5 mA h g^{-1} at 0.1 C, and 529.7 mA h g^{-1} was still maintained after 200 cycles, presenting a capacity retention rate of about 59.8%.

A facile solution-based chemical method was reported to prepare Li_2S nanoparticles coated N-doped carbon nanofibers. Compared with the commercial Li_2S particles, the prepared composites possess several advantages: first, the small size of Li_2S could lower the energy barrier in the first charging process and can be easier activated; second, the uniform distribution of Li_2S on the conductive matrixes could enhance the contact and improve active materials utilization; third, the N-doped carbon nanofibers could trap polysulfides to reduce the dissolution due to the strong chemical bonding between nitrogen atom and ploysulifdes. In addition, a Li_2S@N-C electrode with high mass loading of 3 mg cm^{-2} was prepared, which delivered a high specific capacity of 916.2 mA h g^{-1} at 0.1 C and 321 mA h g^{-1} at 2 C, because the high mass loading is important to practical application. As results, the prepared samples show excellent cycling stability and rate capability (a high capacity of 380.4 mA h g^{-1} at 5 C).

TABLE OF CONTENTS

LIST OF FIGURES

LIST OF TABLES

LIST OF ABBREVIATIONS

Abbreviation	Full name
3D	Three-dimensional
APS	Ammonium peroxydisulfate
a.u.	Arbitrary unit
BET	Brunauer Emmett Teller
cm	Centimeter
CNFs	Carbon nanofibers
GA	Graphene aerogel
CTAB	Cetyltrimethylammonium bromide
CV	Cyclic voltammetry
EDS	Energy dispersive X-ray spectroscopy
EIS	Electrochemical impedance spectroscopy
EV	Electric vehicle
FE-SEM	Field emission scanning electron microscopy
FTIR	Fourier transform infrared spectroscopy
GO	Graphene oxide
HEV	Hybrid electric vehicle
HR-TEM	High-resolution transmission electron microscopy
rGO	Reduced graphite oxide
LIBs	Lithium-ion batteries
LSB	Lithium-sulfur batteries
um	Micrometer
nm	Nanometer

NMP	1-methyl-2-pyrrolidione
PTS Na	Sodium p-toluenesulphonate
PPy	Polypyrrole
PVDF	Polyvinylidene fluoride
Py	Pyrrole
SWCNTs	Single-walled carbon nanotubes
FeToS	Ferric salt iron (III) p-toluenesulfonate
SEI	Solid electrolyte interphase
SEM	Scanning electron microscopy
SHE	Standard hydrogen electrode
STEM	Scanning transmission electron microscope
DOL	1,3-dioxolane
DME	1,2-dimethoxyethane
TEM	Transmission electron microscopy
TGA	Thermogravimetric analysis
XPS	X-ray photoelectron spectroscopy
XRD	X-ray diffraction
N-CF	N-doped carbon fiber
LiTFSI	Lithium bis(trifluoromethylsulphonyl)imide

LIST OF SYMBOLS

Symbol	Name	Unit
2θ	Detection angle in XRD	Degree
C-rate	Charge or discharge rate	mA g^{-1}
d	Lattice spacing	nm
S_{BET}	Specific BET surface area	m^2 g^{-1}
F	Faraday's constant = 96485	C mol^{-1}
I	Current	A
T	Temperature	K or °C
t	Time	h or s
wt.%	Weight percent	-
λ	X-ray Wavelength	Å
R_{ct}	Charge transfer resistance	Ω
f	Frequency in the EIS test	Hz
W	Warburg impedance	Ω
η	Coulombic efficiency	%
σ	Ionic conductivity	S cm^{-1}

LIST OF ORGANIZATIONS

Abbreviation	Full name
ISEM	Institute for Superconducting and Electronic Materials
AIIM	Australian Institute for Innovative Materials
EMC	Electron Microscopy Centre
UOW	University of Wollongong

CHAPTER 1 INTRODUCTION

1.1 General background

Over the past several decades, due to the rapid development of society and the advance of science and technology, we have made great progress in various fields such as chemical industry, environmental protection, aerospace, medicine, electronics, energy, and so on. Our enormous consumption of fossil fuel has had certain impacts on our daily lives, however, such as environmental pollution and global warming.[1] In addition, traditional energy sources, such as fossil fuel, are non-renewable and will be exhausted someday. Therefore, these considerations are motivating us to find sustainable energy sources that do not involve excessive environmental damage.[2] Some renewable energy resources, such as wind, water, and solar energy, have drawn much attention,[3] but they are intermittent with the weather or time. The lithium rechargeable battery is considered as one of the most promising devices for energy storage, which was first proposed and studied by Gilbert N. Lewis and commercialized in the 1970s.[4] Lithium is the most positively charged (-3.04 V relative to the standard hydrogen electrode) and the lightest (molar mass, M = 6.94 g mol^{-1}, density, ρ = 0.53 g cm^{-3}) metal, which could facilitate the development and application of high-energy-density storage devices. Lithium-ion batteries (LIBs) have dominated the portable electronics markets for several decades due to their high capacity, wide operating temperature range and long cycling life.[5-7] The common cathode materials used in LIBs are layered metal oxides ($LiMO_2$ with M = Co, Fe) and spinel structures (LM_2O_4 with M = Mn, Ni)[8, 9], however, which are high-cost, with limited specific capacity and cannot meet the requirements of large-scale energy storage applications such as electric vehicles (EVs) and grid-scale energy storage systems. Thus, exploring novel batteries based on conversion reactions rather

than intercalation reactions is a strategy that is inevitably needed to obtain high-performance Li-ion batteries.

Lithium-sulfur batteries (Li-S) are regarded as a promising candidate for next-generation energy storage system due to the abundance, safety, and low-cost of sulfur.[10-12] Based on the conversion reaction between lithium and sulfur, the Li-S batteries could deliver a high theoretical specific capacity of 1675 mA h g^{-1}. After considering the average discharge voltage of Li-S (2.15 V *vs.* Li^+/Li), the energy density of Li-S could reach as high as 2600 Wh kg^{-1}, which is significantly higher than that of the existing lithium ion battery today (Figure 1.1).[13] If the Li-S batteries could be applied for powering electric vehicles instead of LIBs, the driving distance between charges could be significantly increased compared with that of the current Li-ion batteries. Therefore, the full development of Li-S batteries will promote their practical application and make a significant contribution to solving the problem of exhaustion of traditional energy resources.

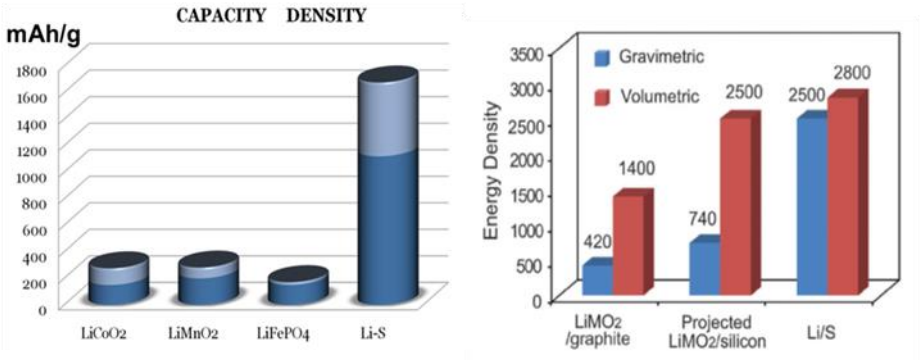

Figure 1.1. Comparison of capacity and energy density of Li-S batteries and current Li-ion batteries.[13]

Despite the great progress that has been achieved on the Li-S batteries,[14, 15] including cathode materials, anodes, electrolytes, separators, whole cell structures, etc., the

electrochemical performance of current Li-S batteries are not high enough to realize its commercialization. Therefore, the work reported in this doctoral thesis had the aim of realising higher specific capacity, and longer and more stable cycling performance via rational design of sulfur cathode materials, modifying the separator, and using Li_2S instead of sulfur as the cathode material.

1.2 Challenges for Li-S batteries

There are still several obstacles hampering the practical application of Li-S batteries,[11, 16] although exciting progress has been made over the past few years,[17-19] as shown in Figure 1.2.[20] First, the conductivity of sulfur and of its final discharge product Li_2S is very low (5×10^{-30} S·cm^{-1} for sulfur), so that they can be regarded as insulating materials,[21] which can cause the low utilization of the active materials and low capacity. Second, the reaction of lithium and sulfur is a multistep process during cycling. The intermediate products − lithium polysulfides (Li_2S_x, $2 < x \leq 8$) are soluble in the electrolyte and can be shuttled between the cathode and anode electrodes, leading to the so-called "shuttle effect".[22] In addition, the polysulfides could pass though the separator and react with the lithium anode, resulting in the corrosion of lithium metal and the irreversible loss of active material over the course of cycling. Last, the volume expansion (~80%) of sulfur during discharge, which is due to the density difference between sulfur (2.07 g cm^{-3}) and Li_2S (1.66 g cm^{-3}), is also a big problem. The volume changes could make the mechanical structure of the cathode unstable and lead to failure of the battery.[23, 24] The above-mentioned problems can lead to unfavourable results, such as low utilization of active materials, poor cycling stability, and short lifespan of the Li-S batteries.

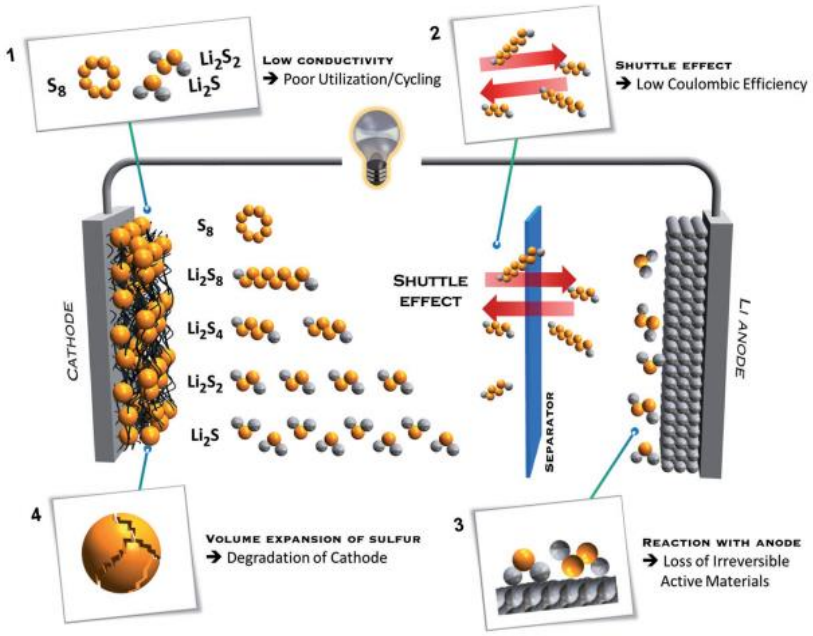

Figure 1.2 Schematic illustration of the challenges faced by Li-S batteries.[20]

In summary, to realize the commercialization of the Li-S battery, the following efforts need to be made to overcome these drawbacks:[22, 25-27] (1) Improving the conductivity of cathode materials. Conductive additives need to be added into the sulfur cathode, and well-dispersed sulfur in the conductive matrix is desirable to ensure fast electron transportation between the interfaces between the conductor and the active material. (2) Suppressing the shuttle effect of lithium polysulfides during cycling. Feasile hollow structures can be designed to load active materials inside and physically block the dissolution of polysulfides. Another efficient method is to introduce some additives into the cathode, which can be chemically bonded with polysulfide, thus restricting the dissolution of polysulfides into the electrolyte. (3) Buffering volume expansion. Flexible materials can be used in the cathode to buffer the volume changes. Utilizing porous or void-containing sulfur composites is also applicable to avoid cracking of the cathode during cycling. In this thesis work, most efforts have mainly been devoted to mitigating the aforementioned challenges to improve the electrochemical performance

of Li-S batteries, such as by exploring suitable conductive matrices to improve the utilization of active materials, modifying the separator to suppressing the shuttle effect, using Li_2S instead of sulfur as cathode to address the volume changes, etc.

1.3 The goals of this work

In this doctoral work, the main goal is to improve the electrochemical performance of Li-S batteries by exploring novel conductive matrices, designing suitable cell structures, preparing bifunctional separators, etc. In my first two works, sulfur was selected as the active material for Li-S batteries. By carefully choosing conductive matrices, modifying the separator, and designing a flexible current collector, the capacity and cycling stability of the designed Li-S batteries were significantly improved. To further improve the safety of the Li-S batteries, Li_2S was applied as the active material in my next two works because Li_2S can paired with lithium-free anode materials, which can overcome the safety problems related to the lithium anode. Moreover, technologies such as ex-situ X-ray diffraction (XRD), ex-situ X-ray photoelectron spectroscopy (XPS), and ex-situ transmission electron microscopy (TEM) were implemented to investigate the physical characteristics and morphologies of the cathode materials.

1.4 Outline of the thesis

The scope of this doctoral work is covered in eight chapters, which are briefly outlined as follows:

Chapter 1 concisely introduces the general background, main challenges, some strategies for improving the electrochemical performance of Li-S batteries, and the outline of this study.

Chapter 2 contains a literature review on Li-S batteries, which includes the general background, a brief history, general principles, basic concepts, and the current research status of Li-S batteries.

Chapter 3 presents the list of chemicals and methods that were applied in the synthesis of materials in this thesis work, and the physical and electrochemical characterization techniques used in this study are also briefly introduced.

Chapter 4 discusses a free-standing sulfur-polypyrrole cathode and a polypyrrole coated separator applied for flexible Li-S batteries. The free-standing cathode could effectively enhance the adhesion of active materials and further trap dissolved polysulfides due to the rough surface of prepared PPy film and the strong interaction between PPy and the polysulfides. In addition, the bifunctional PPy-coated separator could prevent the dissolved polysulfudes from passing through the separator and improve the utilization of active materials. A soft-packaged flexible Li-S battery based on the free-standing sulfur-polypyrrole cathode and the polypyrrole coated separator has been designed and fabricated to power a device consisting of 24 light emitting diode (LED) lights. The designed flexible Li-S battery shows good performance in the bent state, which can be ascribed to the excellent mechanical flexibility of the PPy film and the bifunctional separator.

Chapter 5 presents a thin PPy-film-coated sulfur/graphene aerogel composite as a cathode material for Li-S batteries. The polypyrrole layer acts as a container to efficiently suppress polysulfide dissolution by strong chemical adsorption, improving the long-term cycling stability. The graphene could improve the conductivity of the cathode material, yielding good rate capability. In addition, a novel vapour phase method was applied to load the PPy layer, in which the sulfur/graphene hydrogel could

shrink and further enhance the contact between the sulfur and the conductive agent. As a result, the designed PPy-coated sulfur/graphene aerogel composite showed a high capacity of 689 mA h g^{-1} after 500 cycles at 0.5 C with an ultra-slow decay rate of 0.03 % per cycle.

A Li_2S-PPy hybrid prepared *via* a facile and large-scaled ball-milling method was investigated in Chapter 6. The PPy nanofibers not only act as a conductive agent to improve the conductivity of the cathode materials, but as a chemical absorber to trap polysulfides. In addition, 3D carbon paper was applied as a current collector to increase the loading of active materials (~ 3 mg cm^{-2}). A PPy-modified separator was also used to improve the cycling stability of Li-S batteries. As a result, the designed Li-S battery with the Li_2S-PPy cathode and the PPy separator delivered a high capacity of 529.7 mA h g^{-1} after 200 cycles at 0.1 C, with a capacity retention rate of about 59.8%.

Chapter 7 presents a facile solution-based chemical method was reported to prepare Li_2S nanoparticles coated N-doped carbon (Li_2S@N-C) nanofibers. Due to the solution-based method, the synthesized Li_2S nanoparticles could uniformly distribute on the surface of carbon nanofibers. And a small energy barrier was observed for the Li_2S@N-C composites due to its small size. In addition, the N-doped carbon could absorb dissolved polysulfides to reuse, guaranteeing a stable cycling performance and high specific capacity. The Li_2S@N-C composites with different mass loading of active materials also show excellent rate capability, for example, the Li_2S@N-C with a mass loading of 1 mg cm^{-2} delivered a specific capacity of 380.4 mA h g^{-1} at 5 C.

Chapter 8 summarizes the main conclusions and achievements of this thesis. A brief outlook based on this study is also provided for researchers, followed by lists of references and publications during the period of this study.

CHAPTER 2 LITERATURE REVIEW

Batteries as one class of energy storage device can transform chemical energy into electric energy. In the case of Li-S batteries, the electrical energy is stored in electrode materials through the conversion reaction between lithium and sulfur. In this chapter, the mechanism of Li-S batteries and recent developments related to the cathode, separator, anode, and electrolyte will summarized.

2.1 Mechanism of the Li-S batteries

A typical Li-S battery primarily consists of a cathode and an anode, which are separated by the separator. As shown in Figure 2.1, there are two kinds of Li-S batteries.[16] One uses using lithium metal as the anode electrode and a sulfur-containing material as the cathode electrode; the other uses a silicon-based or tin-based material as the anode electrode and lithium sulfide as the cathode electrode. Both systems can be used with organic liquid or solid electrolytes. So far, Li-S batteries with lithium metal as the anode electrode and sulfur-containing materials as the cathode electrode have been the most widely studied.

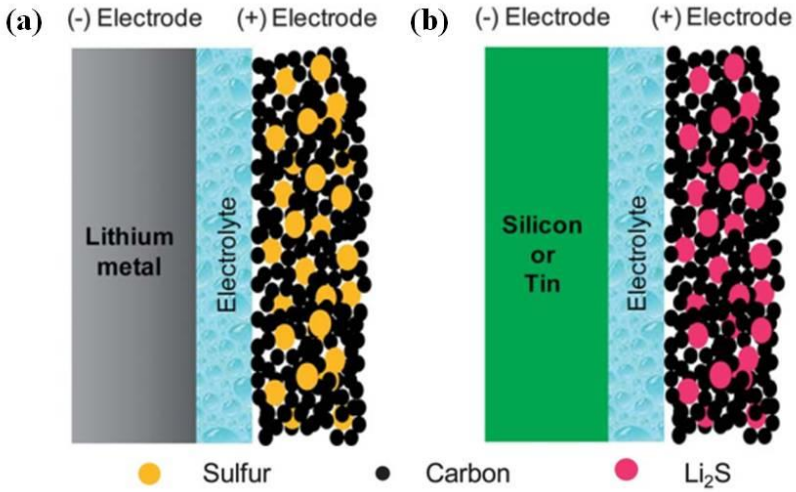

Figure 2.1. Schematic diagrams of the two kinds of configurations of Li-S batteries.[16]

In a Li-S battery system using S as the cathode material, during discharge, the lithium is oxidized into lithium ions and releases electrons. The lithium ions will spontaneously migrate from the anode side to the cathode side through the electrolyte and react with the cathode material, while the electrons flow through the external circuit to deliver electrical energy. In the meantime, sulfur will be reduced to lithium sulfide by accepting lithium ions and electrons. The reaction that occurs during the discharge process is expressed by the following formula, and the charging process involves the reverse reaction.

Anode: oxidation reaction, loss of electrons

$$2\ Li \rightarrow 2\ Li^{+} + 2\ e^{-} \qquad (1)$$

Cathode: reduction reaction, electrons are gained

$$S + 2\ Li^{+} + 2\ e^{-} \rightarrow Li_2S \qquad (2)$$

Total battery reaction (discharge process)

$$2\ Li + S \rightarrow Li_2S, \quad E^0 = 2.15\ V \qquad (3)$$

Even though the reaction described by the formula is very simple, it is an ideal situation, that only appears in solid-state Li-S batteries. In most liquid Li-S batteries, the real reaction process is multi-step, which is much more complicated than it looks. Sulfur is in the form of octasulfur (cyclo-S_8) molecules because it is the most stable structure at room temperature. During the discharge process, there are many intermediate products (Li_2S_n, $8 > n > 2$), which are soluble in electrolyte and cause many side reactions and damage to the active materials.

A real discharge profile of a conversional Li-S battery is displayed in Figure 2.2a, which consists of three regions. In the upper plateau region at ~ 2.3 V, elemental sulfur (S_8) is gradually reduced to the soluble long-chain sulfide anion (S_8^{2-}).[28]

$$S_8 + 2\ Li \rightarrow Li_2S_8 \qquad (4)$$

Li_2S_8 is unstable in many aprotic electrolytes and undergoes disproportionation to form Li_2S_n, which can also experience electrochemical reduction.

$$Li_2S_8 \rightarrow Li_2S_n + (8-n)\ S \qquad (5)$$

Then, S_8^{2-} is continuously reduced to S_n^{2-} (n = 6 and 4) in the sloping region (2.1 V < V < 2.3 V).

$$3\ Li_2S_8 + 2\ Li \rightarrow 4\ Li_2S_6 \qquad (7)$$

$$Li_2S_8 + 2\ Li \rightarrow Li_2S_4 \qquad (8)$$

These long-chain polysulfides (S_n^{2-} , n = 8 - 4) are soluble in the electrolyte, which can cause the so-called "shuttle effect" and decreases the utilization of active materials.

Thus, the upper plateau and slope regions between ~ 2.3 and ~ 2.1 V is undesirable for obtaining high performing Li-S batteries. In the lower plateau (~2.1 V) region, the Li_2S_4 is further reduced to short-chain polysulfides (S_n^{2-}, n = 2 and 1), which are solid phases.

$$Li_2S_4 + 2\ Li \rightarrow 2\ Li_2S_2 \qquad (9)$$

$$Li_2S_2 + 2\ Li \rightarrow 2\ Li_2S \qquad (10)$$

Finally, Li_2S is formed by the complete reduction of S_8, leading to a theoretical capacity of 1675 mA h g^{-1} and an energy density of ~ 2600 Wh kg^{-1}.[29] The electrochemical reactions during the charge process are reversed compared to thoes during discharge (Figure 2.2b). A long flat lower plateau is seen initially, representing the oxidation of Li_2S to polysulfides. The upper charge plateau marks the further oxidation reactions of polysulfides into sulfur in the dissolution region.

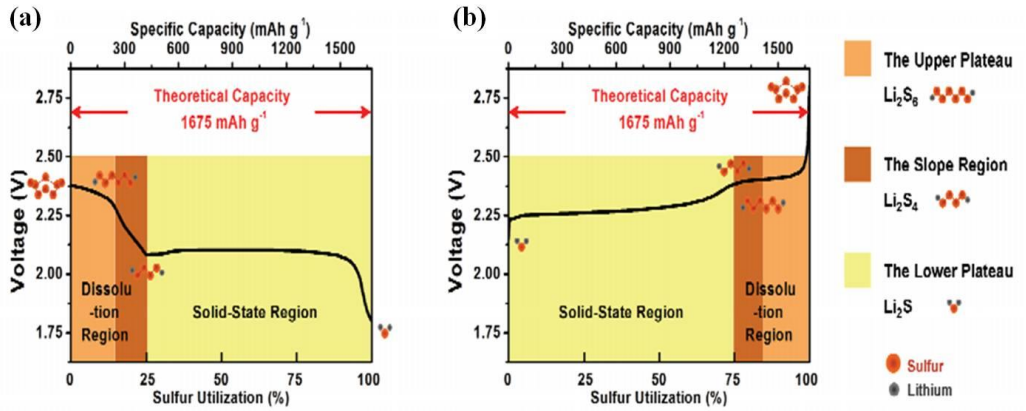

Figure 2.2. Schematic illustration of the (a) discharge and (b) charge profiles of a conventional Li-S battery.[28]

In the reaction process in Li-S batteries, the electrochemical reduction of polysulfides is actually very complicated, and the polysulfides coexist during the reaction process. The reaction path of Li-S batteries will also vary according to the electrolyte composition

and electrode materials. Therefore, the detailed reaction mechanism of Li-S batteries needs to be further clarified.

2.2 Main problems for Li-S batteries

Although Li-S batteries have great advantages in terms of energy density and low cost, there are still many problems that are difficult to solve, preventing their practical application.[17, 19, 30] According to the reaction mechanism of the above-mentioned Li-S batteries and a large number of research results, the following factors are the mainly ones affecting the electrochemical performance of Li-S batteries:

2.2.1 Insulating nature of active materials

Sulfur is an insulator with a resistivity as high as 2×10^{23} μΩ·cm at room temperature, which could lead to poor utilization and rate performance of the active material. In addition, the discharge product Li_2S is also an insulator, which could seriously affect the transmission of electrons in the electrode during cycling. Therefore, it is necessary to add an appropriate amount of conductive additive and to see that it is thoroughly mixed and uniformly dispersed within the active material to ensure good electron transport channels at the interface between the conductive agent and the active material to improve the utilization rate of the active material, enhance the electrode dynamics and improve the cycling performance.[31, 32] The most commonly used conductive additives are porous carbon with a high surface area.[33-35] The addition of the conductive agent is important for obtaining electrodes with high specific energy, high specific power, and reasonable cycle life.

2.2.2 Dissolution of intermediate products

During the reduction of sulfur, a variety of lithium polysulfide (Li_2S_x, $2< x \leq 8$) will be produced, which are extremely soluble in the electrolyte. The dissolved polysulfides are beneficial for increasing the utilization of the active material because the dissolved polysulfide can be in better contact with the conductive agent and can facilitate contact between the sulfur inside the electrode and the conductive agent/electrolyte.[36] However, this dissolution also brings a number of disadvantages. When the dissolved polysulfide diffuses out of the positive electrode region, it can no longer be utilized, resulting in rapid decay of the battery capacity during the cycling. Therefore, to obtain a high-performance Li-S battery, optimization of the electrode structure and electrolyte to confine these polysulfides in the cathode region is very important.[37-40]

2.2.3 Shuttle effect

As described above, during the discharge process, the elemental sulfur is reduced to lithium polysulfide (Li_2S_x, $4< x \leq 8$), which is soluble in liquid electrolyte. The concentration of polysulfides on the cathode side is higher than that on the anode side. Due to the concentration gradient, the polysulfide diffuses through the electrolyte to the lithium anode, where it could react with lithium on the anode side to form a short-chain polysulfide or even a solid state product (Li_2S_2 or Li_2S), which cause corrosion of the lithium anode. If the solid state product is deposited on the lithium anode, it could block the electron and ion transport in the electrode, leading to the failure of the Li-S battery. These short-chain polysulfide can diffuse back to the sulfur electrode, generating long-chain polysulfide again. This phenomenon in which the polysulfide alternates between the cathode and the anode is referred to as a "shuttle effect", as shown in Figure 2.3.[41] The "shuttle effect" is a special property of metal-S batteries with liquid

electrolyte, which is an important factor causing capacity decay, loss of active materials and poor coulombic efficiency.

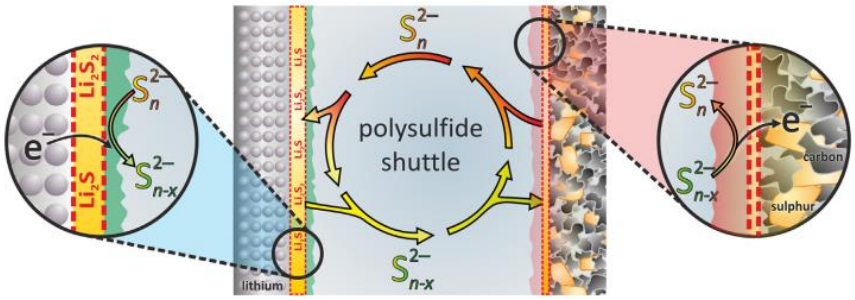

Figure 2.3. Schematic illustration of the shuttle effect in Li-S batteries.[41]

2.2.4 Volume expansion

Due to the different densities of sulfur (α phase, 2.07 g cm^{-3}) and lithium sulfide (1.66 g cm^{-3}), volume expansion (80%) during cycling is another problem for Li-S batteries.[23, 24] This recurring volume expansion/shrinkage and phase changes during charge and discharge can affect the mechanical stability of the electrode structure. If the electrode structure cracks, the active materials will lose contact with the conductive agent, leading to capacity decay or failure of the battery. Flexible cathode materials are commonly used to buffer the volume changes of the electrode.[15, 42, 43] An only partially sulfur-filled conductive agent is also a wise choice to avoid damage to the electrode structure.[44]

2.2.5 Lithium sulfide and sulfur plating

During the Li-S cell charge and discharge process, the lithium sulfide and elemental sulfur at the end of the discharge are easily deposited on the surface of the electrode and form an insulating layer. This deposition can lead to the formation of "inactive areas" in the electrode, which degrades the cycling performance of the battery; if the agglomeration of lithium sulfide or sulfur blocks the transmission of electrons and ions

in the electrode, it will directly cause battery failure. The dissolution of polysulfide is unavoidable in a Li-S battery using an organic electrolyte. By properly designing the structure of the electrode to trap the polysulfide in the cathode region, the deposition of Li_2S/S on the surface of the electrode can be effectively avoided.[37-40]

2.2.6 Self-discharge

Low self-discharge efficiency is another criterion for judging the utility of energy storage devices. Unfortunately, Li-S batteries also have strong self-discharge behaviour. When a Li-S battery is assembled with a non-aqueous electrolyte, with increasing storage time, the sulfur in the cathode reacts with the lithium ions in the electrolyte to produce the dissolved polysulfide, which results in thegradual dissolution and migration of the active material, leading to a decrease in the open circuit voltage (OCV) and discharge capacity, as shown in Figure 2.4.[10] Rational design of the cell configuration, which can prevent the reaction of sulfur and lithium ions, is critical to avoid self-discharge in the Li-S battery.

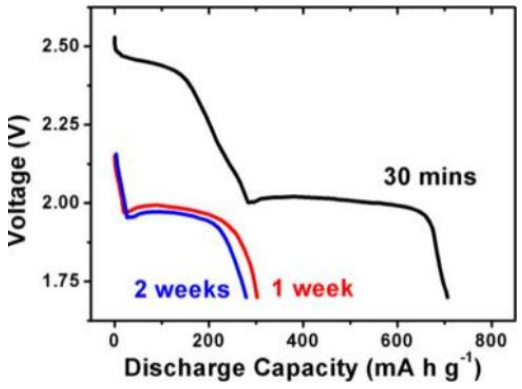

Figure 2.4. Self discharging behaviour of Li-S batteries.[10]

2.3 Approaches to overcome these drawbacks

Great efforts have been devoted to overcoming these disadvantages of Li-S batteries, which have included exploring favourable conductive agents (carbonaceous or polymer materials) to load the sulfur, designing novel cell configurations, searching for suitable electrolytes, modifying the surface of the anode *etc*. The following sections will give some representative examples of these approaches.

2.3.1 Sulfur cathode materials

It is well known that the poor conductivity of sulfur makes it impossible to use it alone as the cathode material. Therefore, combining the sulfur with various conductive materials, such as carbon-based materials,[45] polymers,[46, 47] and metal oxides/sulfides[48] is the most common way to improve the conductivity of sulfur cathode material. In addition, the conductive agent could prevent the lithium polysulfide from dissolving into the electrolyte by physical adsorption or chemical bonding, improving the capacity and cycling stability of Li-S batteries.

2.3.1.1 sulfur-carbon composites

The ideal host material for sulfur should have the characteristics of high conductivity, facile synthesis, stable material structure, and high loading mass of active materials. Due to these consideration, the carbonaceous materials have been the most intensively investigated host materials for Li-S batteries due to their high conductivity, diverse structures, and relatively low-cost synthetic method.[45] Meanwhile, the carbonaceous materials have the capability of physically adsorbing soluble polysulfides to enhance the cycling stability.

In 2009, Linda and co-workers[34] prepared an ordered mesoporous carbon material, CMK-3, consisting of hollow 6.5 nm-thick carbon rods separated by 3-4 nm-wide channel voids as the matrix for sulfur (Figure 2.5). The sulfur was filled into the channel voids via heat treatment of a mixture of sulfur and CMK-3 at 155 °C, which generated the essential electrical contact between the carbon and the insulating sulfur, leading to faster Li^+ ingress/egress within the cathode. This achievement has prompted many researchers to try to achieve breakthrough in the performance of Li-S batteries based on the structural design of carbon materials, thereby preparing a variety of carbon carriers with different morphologies and rich pore structure, including (1) porous carbon-sulfur composite, (2) hollow carbon structures, (3) graphene, and (4) heteroatom doped carbon materials.

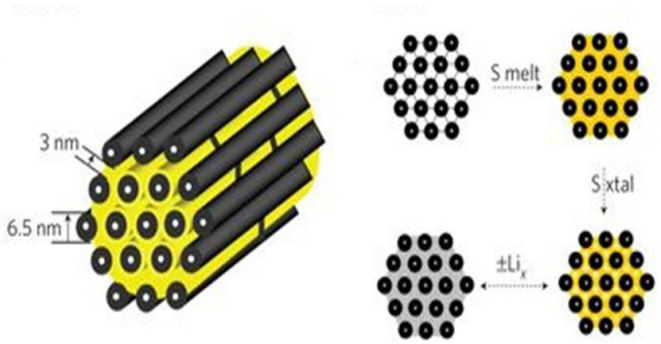

Figure 2.5. Schematic diagram of the sulphur (yellow) confined in the CMK-3.[34]

Porous carbon-sulfur composites: Porous carbon materials can be classified into three main types according to pore size: 1) microporous carbon (pore size < 2 nm), which has been proven to be an ideal matrix to mitigate the dissolution of polysulfides because this pore size is consistent with that of polysulfides[49, 50]; 2) mesoporous carbon (with pore size between 2 and 50 nm), which could provide abundant channels for the transportation of lithium ions and full contact with the electrolyte.[51, 52]. It can also increase the loading amount of sulfur in the cathode; 3) macroporous material (pore size

greater than 50 nm) is rarely used in sulfur cathode because the pore size is too large to trap the active materials or the electrolyte. Therefore, microporous carbon and mesoporous carbon are widely used as conductive agents in Li-S batteries. Guo 's group[49] used microporous carbon with a pore size of only 0.5 nm to load sulfur (Figure 2.6a-c). Due to the limitation to micropores, the sulfur molecules entering the pores could only exist in the form of S_{2-4} small molecules, and could not go back to the S_8 ring state during the charge process, avoiding the formation of long-chain soluble polysulfides and preventing the capacity fading during cycling. As a result, the sulfur cathode with a samller particles delivered a capacity of 1142 mA h g^{-1} with a capacity retention rate as high as 96% over 200 cycles at 0.1 C, showing excellent cycling stability. In addition, the rate performance is also very good, showing a specific capacity of 800 mA h g^{-1} at current density up to 5 C (Figure 2.6 d and e).

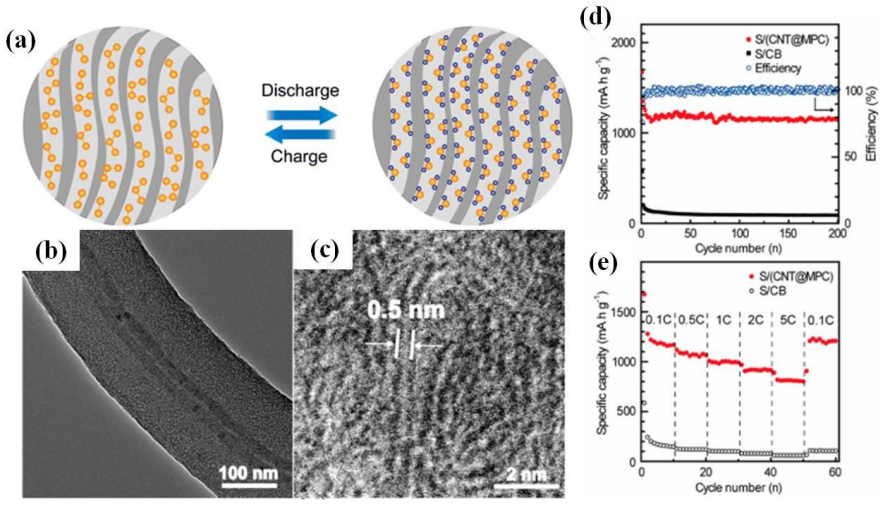

Figure 2.6. Structural characterization and charging- discharging performance of microporous carbon as a host material for small sulfur particles.[49]

Important work on mesoporous carbon was reported by Li[53] et al., who were studying the effects of different pore sizes (22 nm, 12 nm, 7 nm, and 3 nm) and pore volumes (from 1.3 to 4.8 cm^3 g^{-1}) on the electrochemical performance of Li-S batteries. The

results indicated that different mesoporous carbon-sulfur (MCS) composites show similar battery performance under the full sulfur-filling conditions. Therefore, we can choose mesoporous carbon with large pore volume to increase the sulfur loading without sacrificing the cell performance. Under partial sulfur-filling conditions, however, the battery shows an improved initial discharge capacity and cycling stability, probably because of improved electrical and ionic transport during electrochemical reactions to ensure a stable supply of lithium ions. This work shed light on how to prepare high mass loading and advanced Li-S batteries.

The porous carbon materials that contain both micropores and mesopores have been widely studied to improve the electrochemical performance of Li-S batteries by the synergistic effects. Zheng and co-workers[54] designed hybrid micro-mesoporous graphitic carbon spheres (M-MGCSs) featuring ordered mesoporous graphene-like cores and uniform microporous carbon shells as a sulfur reservoir for Li-S batteries (Figure 2.7 a). The obtained M-MGCSs combined the merits of both micro- and mesoporous carbons: the inner core with interconnected spherical mesopores 9.0 nm in size provided sufficient space for loading S_8 molecules, while the shell with micropores 0.6 nm in size could entrap only small S_{2-4} molecules, which are converted into electrolyte-insoluble polysulfides during discharge, minimizing the outward diffusion of long-chain polysulfides from the core (Figure 2.7 b-d). As a results, the M-MGCSs composite with a 20 nm shell thickness showed the best electrochemical performance, with a reversible capacity of 702 mA h g^{-1} at 1 C after 300 cycles, representing a capacity retention of 78.1% (Figure 2.7 e).

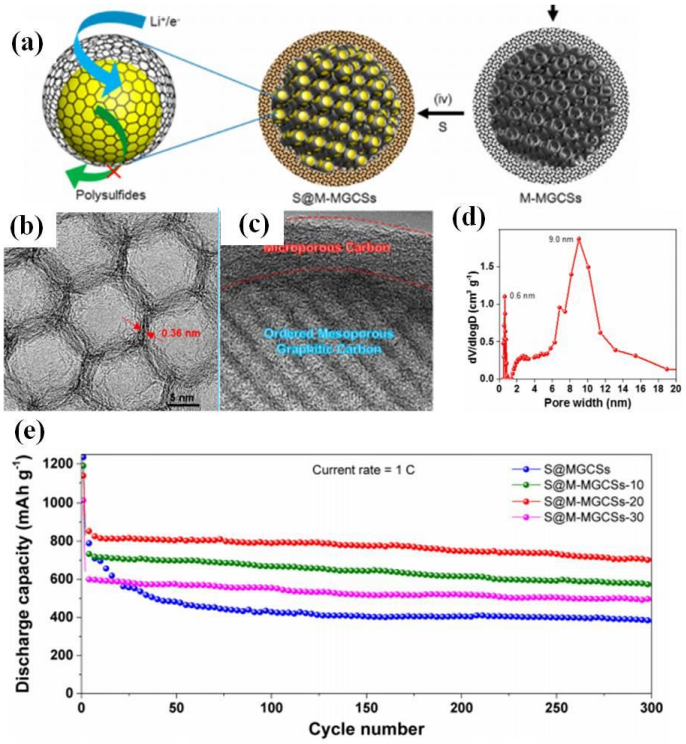

Figure 2.7. (a) Schematic illustration of the synthesis of S@M-MGCSs. (b) High resolution transmission electron microscope (HRTEM) image of M-MGCSs, showing that the pore walls were constructed from few-layer stacks of graphene with an interlayer spacing of 0.36 nm. (c) HRTEM image of M-MGCSs, showing the microporous carbon shell. (d) Pore size distribution of M-MGCSs. (e) Cycling performance of various composite cathodes at 1 C.[54]

Hollow carbon-sulfur composite: Due to the large internal cavity volumes, hollow carbon materials could increase the loading of active materials, alleviate the volume changes of the active material, and shorten the transport distance for lithium ions as conductive matrixes for Li-S batteries. Therefore, various kinds of hollow carbon structures have been widely investigated to load sulfur.[33, 55-57] In 2012, Zhang et al.[58] used hollow spherical tin dioxide as a hard template to prepare double-shell hollow carbon spheres (DHCS) as a sulfur host material (Figure 2.8a). The carbon spheres have a specific surface area of 748 m^2 g^{-1} and a pore volume of 1.685 cm^3 g^{-1}. After loading

64% of the sulfur into the hollow carbon spheres, the specific discharge capacity was maintained at 690 mA h g^{-1} at 0.1 C after 100 cycles (Figure 2.8b). A novel tube-in-tube structured carbon nanomaterial (TTCN) composites with higher sulfur content was reported by Zhao et. al,[55] which showed enhanced electrical conductivity to improve the utilization of sulfur and provided a large pore volume to increase the amount of sulfur loading (Figure 2.8 c-i). The obtained S-TTCN composite with 71 wt% sulfur content delivered high reversible capacity, good cycling performance, excellent rate capability. At a current density of 2 A g^{-1}, it still retained a high discharge capacity of 647 mA h g^{-1} after 200 cycles.

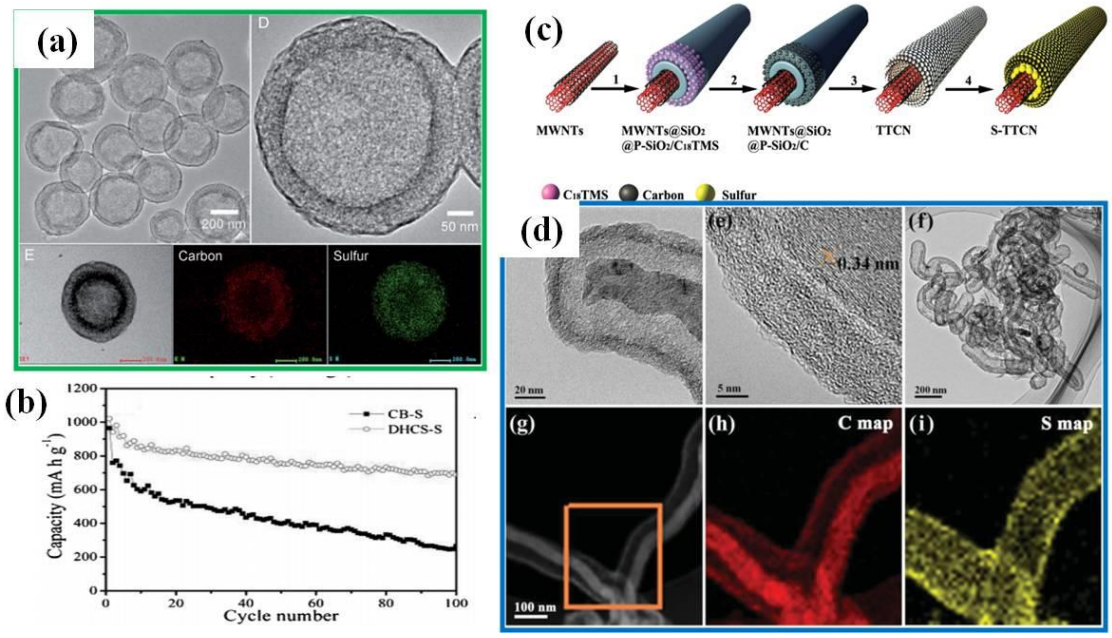

Figure 2.8. (a) Transmission electron microscope (TEM) image of DHCS and DHCS-S composites and element mapping of DHCS-S. (b) Comparison of the cycling performances of DHCS-S and carbon black-sulfur (CB-S) composites.[58] (c) Schematic illustration of the formation of S-TTCN composite, and (d) TEM images of TTCN and the element distributions in S-TTCN composite.[55]

Graphene-sulfur composite: Graphene, compared with other carbon materials, possess high electrical conductivity to facilitate the transportation of electrons and ions.[59] The electron conduction rate of graphene is close to 1/300 of the speed of light, far exceeding the speed of electrons in general conductors. Moreover, the oxygen functional groups, such as C=O, -OH and C-O-C, on the surface of graphene provide active sites to anchor the sulfur particles and trap the soluble polysulfide intermediates within the cathode. These characteristics make it an ideal conductive agent to host sulfur for the Li-S battery. Numerous research works on graphene-sulfur composites have been reported to improve the conductivity and significantly increase the rate capability and specific capacity of sulfur cathode materials.[43, 60, 61]

For example, In an early work, Wang[62] reported the synthesis of a graphene-sulfur composite that was constructed by wrapping poly(ethylene glycol) (PEG) coated sub-micrometer sulfur particles with mildly oxidized graphene oxide sheets decorated by carbon black nanoparticles. The PEG and graphene coating layer played a synergistic role in suppressing the volume expansion, trapping soluble lithium polysulfides, and rendering the sulfur particles electrically conducting. The obtained composite material retained a specific capacity of 600 mA h g^{-1} after 100 cycles. To further improve the specific capacity and cycling stability, Zhang and co-workers[63] reported interconnected carbon nanotube/graphene nanosphere scaffolds as a free-standing paper electrode for the Li-S battery (Figure 2.9 a). The materials combine the advantages of carbon nanotubes (CNTs) and graphene: the hollow graphene sphere offered enclosed spaces to accommodate the sulfur species, accommodated the volume fluctuations during cycling, and retarded the dissolution of polysulfides and the shuttle effect. The graphene walls of the graphene spheres and super-long CNTs synergistically constructed hierarchical short-/long-range electron/ion path ways (Figure 2.9 b and c). When the novel hybrids

were used as cathode materials for Li-S batteries, the as-obtained flexible paper electrode exhibited high sulfur utilization of 81% (corresponding to 1346 mA h g^{-1}) at a current density of 0.17 A g^{-1}, with high-rate capacity retention of 40% when the current density increased to as high as 16.7A g^{-1} and superior capacity retention of 89.0 % over 500 cycles (Figure 2.9 d).

Nowadays, modifying the functional groups on the surface of graphene is an interesting method to further improve its conductivity and/or binding properties with respect to polysulfides. Qiu et al. [64] modified reduced graphene oxide by heat treatment under ammonia atmosphere to further improve the electrical conductivity of graphene sheets (~ 270 S cm^{-1}). The obtained nitrogen-doped graphene-sulfur composite demonstrated an ultra-long cycle life exceeding 2000 cycles and an extremely low capacity-decay rate (0.028% per cycle), which can be attributed to the well-restored C-C lattice and the unique lithium polysulfide binding capability of the N functional groups in the nitrogen doped graphene sheets. Moreover, sandwich-like graphene (oxide)-carbon composites were also made to enhance the performance of Li-S batteries. Tang *et al.*[65] synthesized nitrogen-doped aligned carbon nanotube/graphene (N-ACNT/G) sandwiches (Figure 2.9e). In this study, a metal-embedded supported bifunctional catalyst was used for the in-situ growth of the ACNT/G sandwiches, in which metal-oxide lamellae acted as a hard template catalyst for graphene deposition and metal nanoparticles acts as catalysts for CNT formation. The prepared N-ACNT/G composite was used as a 3D scaffold to accommodate sulfur for the Li-S battery. The electrochemical performance results showed that N-ACNT/G hybrid in the Li-S battery showed enhanced cycling capacity and rate capability, and was a promising candidate for high performance Li-S batteries (Figure 2.9h). This could be ascribed to three aspects: (1) the nitrogen-modified interfaces could enhance the interfacial affinity for efficient confinement and utilization

of sulfur; (2) the 3D interconnected mesoporous space is beneficial for the diffusion and penetration of electrolyte; and (3) the seamless junction of CNTs and graphene facilitate mechanical robustness and rapid electron transfer (Figure 2.9f and g).

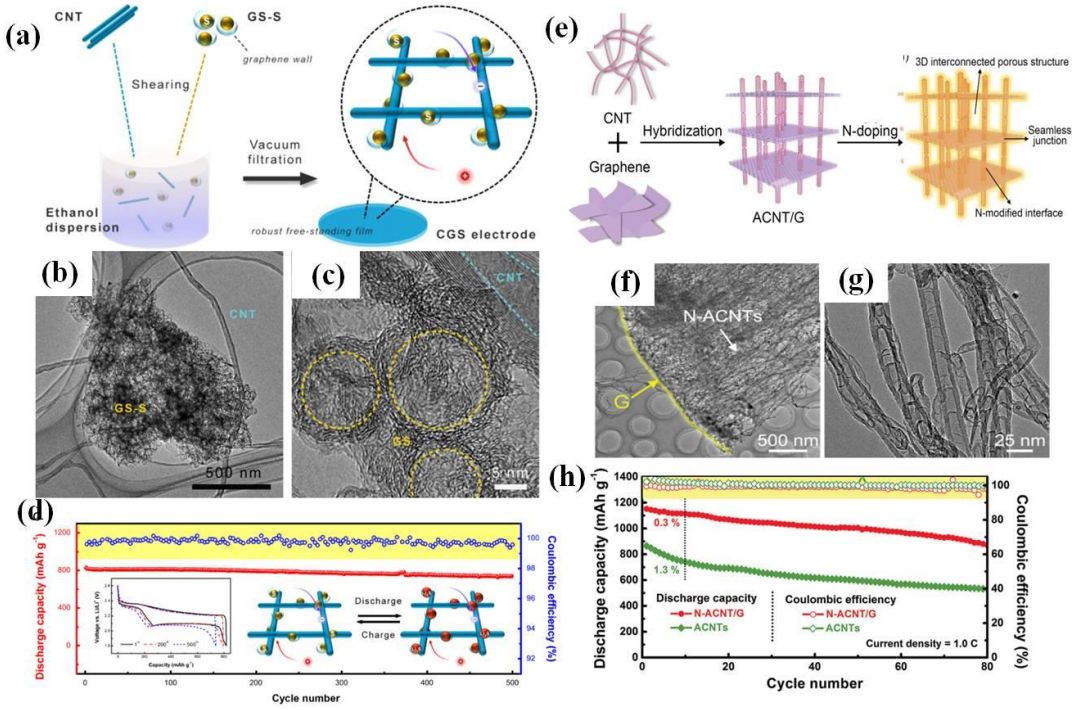

Figure 2.9. (a) Schematic illustration of the fabrication route for the carbon nanotube/graphene nanosphere (CGS) electrode, (b) TEM and (c) HRTEM images of the CGS structure, (d) long-term cycling test at 0.5 C (insets show galvanostatic discharge–charge curves of CGS paper);[63] (e) Conceptual scheme of the design of N-ACNT/G hybrids with graphene and aligned CNTs as building blocks, (f) TEM images of N-ACNT/G hybrid, (g) Typical TEM image of the bamboo-structured ACNTs in the hybrid; (h) Cycling performance of N-ACNT/G hybrids and ACNTs at a current density of 1.0 C.[65]

Heteroatom doped carbon materials: Modifying the carbon surface with heteroatoms, such as nitrogen[66-69], sulfur[70] and boron[71], represents a promising approach to improving lithium-sulfur batteries as it can render stronger binding with lithium polysulfide species

to minimize their dissolution into the electrolyte. Zhang's group[72] used N-doped carbon nanotubes as conductive matrixes to achieve stable cycling in Li-S batteries. Theoretical calculations also showed strong Li-N interaction between pyridinic nitrogen atoms and various lithium polysulfide/sulfide species. The as-prepared nitrogen-doped carbon-nanotube-sulfur composite showed a discharge capacity of 937 mAh g^{-1} with 70% capacity retention after 200 cycles at 1 C, which is much better than for using pristine carbon nanotubes. Sun *et al.*[73] used melamine as a precursor and nitrogen source, and silica colloid as a template to prepare a nitrogen-doped porous carbon material and applied it in lithium-sulfur batteries. In this research, the result showed that the appropriate amount of nitrogen atom doping could improve the conductivity of the carbon material. The excellent electrochemical performance of the prepared nitrogen doped porous carbon-sulfur composites can be possibly ascribed to the enhanced surface interaction between the basic nitrogen functionalities and the polysulfide species. Inspired by these studies, sulfur and nitrogen co-doped carbon-sulfur framework[70] was also prepared as a promising sulfur container for the Li-S battery.

2.3.1.2 Polymer-sulfur composites

Although great achievements have been made on the carbon-sulfur composites, in 2013, Cui's group found that the capacity fading mechanism is the detachment of Li_xS from the carbon surface during the discharge process due to the low interactions between the polar polysulfides and the nonpolar carbon.[74] In addition, they also found that the cycling performance of hollow carbon nanofiber-sulfur composite was significantly improved by modifying the interface between the carbon and sulfur with amphiphilic polyvinylpyrrolidone (PVP). Therefore, conducting polymers came to be regarded as a promising class of host materials for sulfur cathode because of their good conductivity and flexible nature, facilitating electron transfer, accommodating the volume expansion

of sulfur, and offering rich functional groups to effectively adsorb polysulfides. Moreover, carbon nanostructures require carbonization processes at high temperature (> 600℃), while the polymer-based sulfur materials are feasibly synthesized below 100 ℃ due to their easy solubility or dispersible capacity in various solvents. Hence, structures (e.g. conformal coating layers to trap polysulfides) that were hard to synthesize as carbon-sulfur composites due to sulfur's low melting point could be achieved using polymer-based sulfur materials. The most common conductive high-molecular-weight polymers include polyaniline[46, 75-77], polyacrylonitrile[78, 79], polypyrrole[80, 81], and polythiophene[82, 83].

One of the earliest polymers studied in this area is polypyrrole (PPy)[80], which was used as a coating layer for sulfur nanoparticles. The capacity was improved after PPy coating, even though the cycling performance was still limited (only 20 cycles). To further improve the cycling performance, a sulfur-polythiophene (PT) core-shell composite[82] was prepared with a uniform polymer coating on the surfaces of the sulfur particles. The initial discharge capacity of the active material was 1119.3 mA h g^{-1} at the current density of 100 mA g^{-1}, and the remaining capacity was 830.2 mA h g^{-1} after 80 cycles. Later, self-assembled polyaniline (PANI) nanotubes[76] were prepared to confine sulfur at the molecular level, which provided strong physical and chemical confinement of the sulfur and soluble polysulfides during cycling. As a result, the electrodes manifested very stable cycling capacity up to 500 cycles at 1 C. Apart from the experimental analysis to prove the advantages of polymers, theoretical calculations were also reported by Cui and co-workers.[84] Three different conducting polymers, poly(3,4-ethylenedioxythiophene) (PEDOT), polyaniline (PANI), polypyrrole (PPY) were coated on monodisperse hollow sulfur nanospheres using oxidative polymerization (Figure 2.10a and b). To indicate the interaction between Li_xS ($0 < x \leq 2$) species and

conductive polymers (PEDOT, PPy, and PANI), ab initio simulations were performed in the framework of density functional theory (Figure 2.10c). The Results indicated that the heteroatoms in the polymer with lone electron pairs (such as oxygen, nitrogen, and sulfur atoms) were able to bind with the lithium atoms in Li_xS ($0 < x \leq 2$) though coordination structures, which gave the theoretical basis for modifying sulfur cathode with different kinds of polymers. The capability of these three polymers towards improving the cycling stability and high-rate capability of the sulfur cathode decreased in the order of PEDOT > PPy > PANI (Figure 2.10 d), because both oxygen and sulfur atoms in the PEDOT could strongly bind with the lithium atom in Li_2S to form a chelated coordination structure. while, both PANI and PPy have weaker interaction with Li_2S that is only based on separate π-σ coordination between the heteroatoms and the lithium atoms.

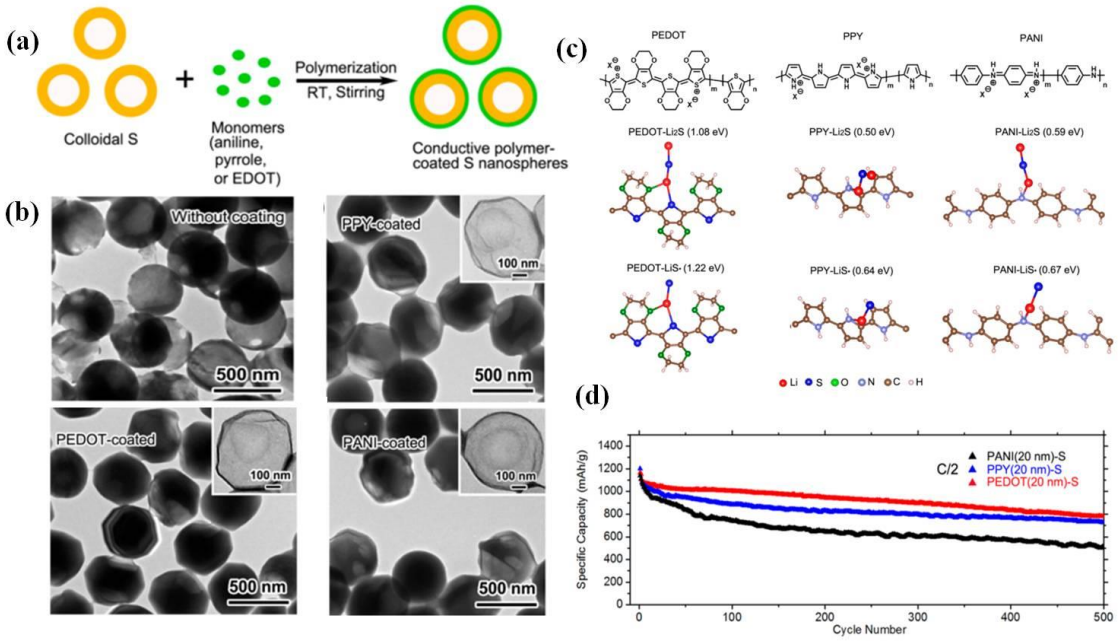

Figure 2.10. (a) Schematic illustration of the fabrication process for conductive polymer-coated hollow sulfur nanospheres, (b) TEM images of hollow sulfur and hollow sulfur coated with different polymers. (c) Chemical structures and the calculated

binding energies of Li_2S and Li-S species with the heteroatoms in PEDOT, PPY, and PANI.[84]

Although polymers exhibit better performance than nonpolar carbon materials in trapping soluble polysulfides via strong chemical bonding, the conductivity of polymers is still not satisfactory for obtaining good rate capability when they are used alone as a conductive matrix alone. Coating polymer on the surfaces of sulfur-carbon composites is a promising way to optimize their long-term cycling stability as well as their high-rate capability. Dong *et al.* [85] reported an efficient approach towards long-life sulfur cathodes, sandwich-type, two-dimensional PPy-graphene hybrid nanosheets. These hybrid nanosheets were fabricated by the infiltration of nanosized sulfur into graphene-backboned mesoporous carbon with a PPy nanocoating (GCS@PPy) (Figure 2.11a). The modified sulfur cathodes in Li-S batteries exhibited a stable capacity retention capability and an ultra slow decay rate of 0.05% per cycle at the high rate of 3 C after 400 cycles (Figure 2.11b). In this architecture, the 2D graphene nanosheet with 3 nm pore size facilitated the diffusion kinetics of electrons and ions, and enabled homogenous nanosized sulfur loading. In addition, graphene served as a nanoscale current collector to allow fast electron transport. The PPy coating could prevent the soluble polysulfides from escaping and thus improved the cycling stability (Figure 2.11c). This work reminds us to design sulfur cathodes by combining a highly conductive agent with chemical absorbers.

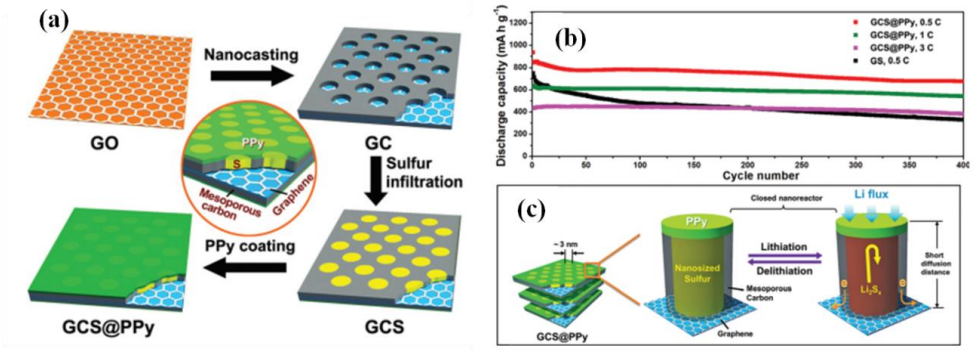

Figure 2.11. Schematic illustration of the synthesis procedure for GCS@PPy hybrid nanosheets, (b) long-term cycling stability of GCS@PPy electrode and (c) schematic illustration of the structural merits of the GCS@PPy hybrid nanosheets towards lithium storage.[85]

2.3.1.3 Polar inorganic metal compounds for sulfur cathode

Inspired by polar polymers that can anchor polysulfides via chemical bonding, a tremendous variety of polar inorganic metal compounds, such as transition-metal oxides, sulfides[48], and carbides[86-88] have been widely studied as polar adsorptive materials for polysulfides. These inorganic materials not only have a strong affinity for lithium polysulfide species and avoid the detachment of active materials into the electrolyte, but render the possibility of accelerating the conversion process of polysulfide into lithium sulfides or the inverse process. Some typical inorganic compounds (with the main focus on metal oxides and sulfides) that have been used in Li-S batteries will summarized, especially relating to their interaction with polysulfides.

Nanostructured metal oxides: Metal oxides that usually contain an oxygen anions in the oxidation state of O^{2-} typically have a strongly polar surface, which can efficiently react with polar polysulfides to suppress their dissolution. Initially, metal oxides, such as $Mg_{0.6}Ni_{0.4}O$[89], Al_2O_3[90] and SiO_2[91], were investigated as additives (less than 10 wt%) in

carbon-sulfur cathodes, which could act as polysulfides reservoirs to increase the utilization of active materials and suppress fast capacity fading. Due to the limited conductivity of these metal oxides, using carbonaceous materials in the sulfur cathode was inevitable. To further improve the adsorption effect of metal oxides, it waas necessary to explore highly conductive metal oxides that could be directly used as sulfur host materials.

TiO_2 is a naturally occurring oxide of titanium, usually classified into rutile (α-TiO_2), anatase (β-TiO_2), and brookite (γ-TiO_2). Nanostructured TiO_2 with different morphologies has been reported for lithium-sulfur batteries.[92-95] In 2013, Cui's group[96] reported a TiO_2-S eggshell nanostructure, which contained voids inside to alleviate the volume expansion of sulfur during cycling and confined the lithium polysulfides within the TiO_2 shell (Figure 2.12 a and b). As a result, the TiO_2-S cathode delivered a capacity of 1030 mA h g^{-1} at 0.5 C with a capacity decay of only 0.033% per cycle after 1000 cycles (Figure 2.12 c). The good electrochemical performance could have been due to the presence of sufficient free space in the structure to buffer the volume expansion of sulfur and maintain the mechanical stability of the TiO_2 shell. Furthermore, the hydrophilic Ti-O functional group in the TiO_2 and the hydroxyl groups on the surface formed a chemical bond with the polysulfide anion to relieve the capacity fading.

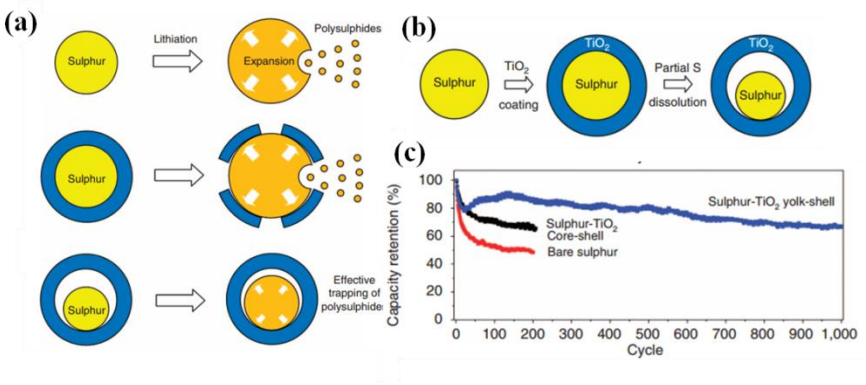

Figure 2.12. (a) Schematic illustration of the lithiation process in various sulphur-based nanostructured morphologies; (b) Synthesis of S-TiO_2 yolk-shell nanostructures, and (c) electrochemical performance of S-TiO_2 yolk-shell structures at 0.5 C.[96]

Based on the effective sulfur anchoring effect of TiO_2 in Li-S batteries, Ti_4O_7 has been proposed and applied as a host material for Li-S batteries. Nazar's[97] group prepared a high-specific-surface area form of Ti_4O_7 (290 m^2 g^{-1}) as a polar carrier for Li-S batteries. The electron density transfer between Ti_4O_7 and Li_2S_4 was explained by theoretical calculation. The superior intrinsic capability of Ti_4O_7 to adsorb polysulfides (using Li_2S_4 as an example) was clear, because after the addition of Ti_4O_7 into the Li_2S_4 solution, a light yellow colour was immediately obtained, but the Li_2S_4 solution became almost completely colourless after 1 h of stirring, indicating strong adsorption. The material with a sulfur loading of 60% could be stably cycled for 500 cycles at 2 C. The decay rate per cycle was only 0.06%. Cui's[98] team reported a series of Ti_nO_{2n-1} nanomaterials with good electrical conductivity as polysulfide absorbers, which all showed strong chemical bonds with polysulfides.

Apart from Ti-based metal oxides, MnO_2 has recently been reported for use in Li-S batteries. Lou's [99] group designed and prepared one-dimensional hollow carbon nanofibers (HCFs) filled with MnO_2 nanosheets to support sulfur (Figure 2.13a). This

material provides an effective support for sulfur and an interconnected three-dimensional conductive network that provides both physical and chemical adsorption. Benefiting from both the HCFs and the MnO_2 nanosheets, the MnO_2@HCF hybrid host not only facilitated electron and ion transfer during the charge-discharge process, but also efficiently prevented polysulfide dissolution. Compared with a simple carbon-nanotube-supported sulfur material, MnO_2 acts as a chemisorber, and the sulfur and polysulfide are confined inside the carbon nanotubes, inhibiting the dissolution of polysulfide (Figure 2.13b).

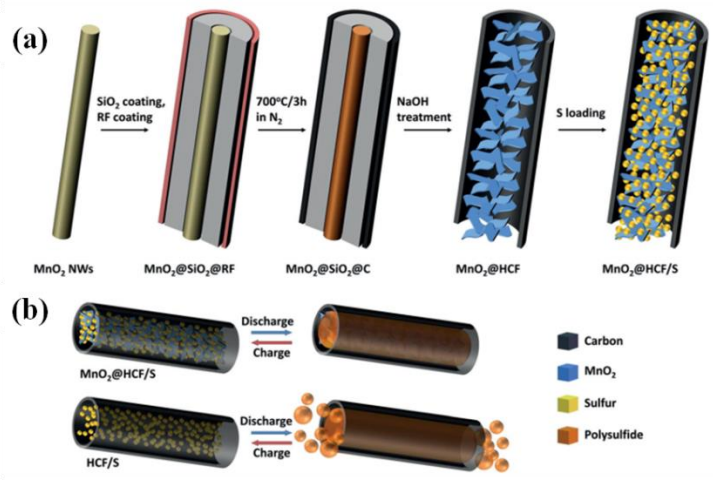

Figure 2.13. (a) Synthesis of the MnO_2@HCF/S composite. (b) Advantages of the MnO_2@HCF/S compositeover HCF/S. [99]

The use of an oxide host for Li-S batteries is also of wide interest. There are some other metal oxides, such as $NiFe_2O_4$,[100] MoO_2,[101] vanadium-based oxides,[102] SnO_2[103, 104], Fe_2O_3,[105] MgO,[106] ZnO,[107, 108] and Co_3O_4,[109] have been explored as host materials for Li-S batteries, although most metal oxides will need to be coupled with conductive carbon materials for use in Li-S batteries due to their relatively lower conductivity. Therefore, highly conductive metal oxides or rational metal-oxide-carbon

nanostructures need to be rationally designed to effectively adsorb the polysulfides in the sulfur cathode.

Nanostructured metal sulfides: In recent years, metal sulfides have been explored for Li-S batteries due to the improvement in the synthesis methods. Moreover, the metal sulfides have two inherent benefits[110]: (1) low Li/Li^+ lithiation voltages, which could not overlap with the working voltage window of the Li-S cells; and (2) the strong chemical interaction with sulfur-containing species, which can efficiently suppress the dissolution of polysulfides. Compared to metal oxides, the nanostructured metal sulfides usually have high electrical conductivity, which can further improve the utilization of active materials and offer higher specific capacity. Considering the above-mentioned conditions, many metal sulfides have been applied in Li-S cells.[48] In the following, several important works relating to metal sulfides as the host material for Li-S batteries will be reviewed.

TiS_2 was one of the earliest metal sulfides used in Li-S batteries because TiS_2 exhibited high electronic conductivity and a high ion diffusion rate. Archer and colleagues[111] reported a TiS_2/S hybrid foam as cathode material for Li-S batteries. The TiS_2 has high electrical and ionic conductivity, which can greatly increase the conductivity of cathode materials. In addition, the discharge potential of TiS_2 occurs nearly at the same potential as that of sulfur cathode, which means that the TiS_2 could offer additional capacity during cycling. Moreover, theoretical calculations indicated that the bonding energy between TiS_2 and lithium polysulfides is nearly ten times stronger than that of carbon-based materials such as graphene, which can help to reduce the dissolution of lithium polysulfides and suppress the shuttle effect. As a result, their TiS_2/S hybrid cathode could maintain a high area specific capacity (~ 6 mAh cm^{-2}) after 100 cycles, even at the high current density of 10 mA cm^{-2}. The active materials loading amount

could reach as high as 40 mg cm^{-2}, which is the highest reported. Later, graphene-like metallic Co_9S_8 was reported as a sulfur host materials by Pang and co-workers.[112] The obtained Co_9S_8 nanosheets had an ultra-high conductivity of 290 S cm^{-1} at room temperature. They also had a high surface area with hierarchical porosity, which could load more active materials and facilitate the transportation of electrons and ions. Most importantly, the bonding interaction of purely Co-terminated (008) planes with lithium polysulfides (LiPSs) (6.06 eV) was much higher than previously reported for other Ti_4O_7 (4.1 eV) or TiS_2 (3.5 eV) host materials. As a result, an ultralow capacity fading rate of 0.045% per cycle over 1500 cycles was achieved.

In the same year, Zhang's group proposed another mechanism of action of cobalt disulfide (CoS_2) as a host materials to reduce the dissolution of LiPSs.[113] They believe that the low redox kinetics of LiPSs was the main reason for the capacity fading. The CoS_2 was a bifunctional matrix: on the one hand, the CoS_2 could absorb LiPSs through the strong interaction between them (Figure 2.14a); on the other hand, the interfaces between CoS_2 and the electrolyte served as strong adsorption and activation sites for LiPSs and accelerated the redox reactions of LiPSs (Figure 2.14 b and c). The fast redox reactions of polysulfides not only guaranteed effective utilization of the active materials but also led to a stable cycling performance over 2000 cycles and a slow capacity decay rate of 0.034% per cycle at 2 C.

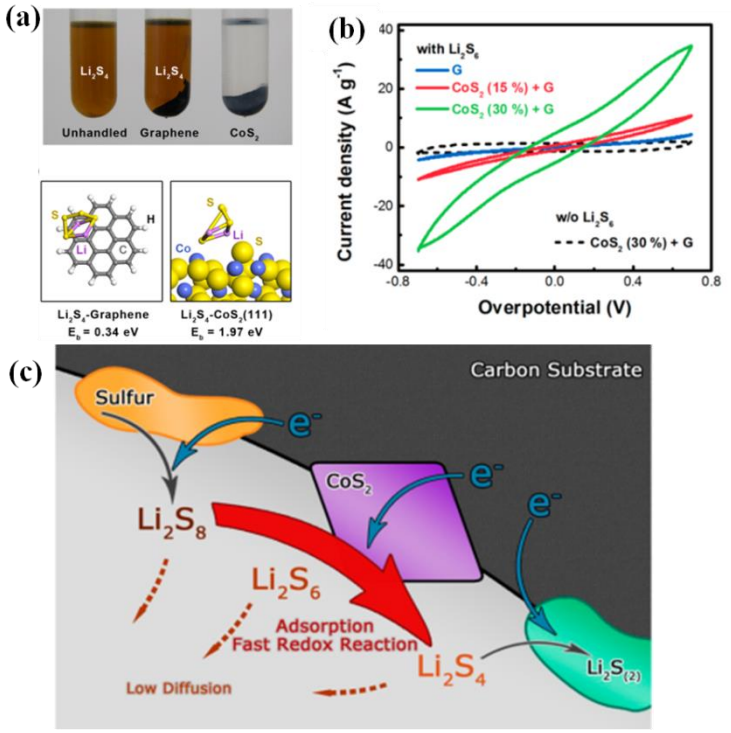

Figure 2.14. (a) High chemical adsorption of Li_2S_4 by CoS_2, (b and c) the catalytic property of CoS_2 towards accelerating the redox reaction of lithium polysulfides.[113]

Apart from the above-mentioned metal sulfdes, there are many metal sulfides that have been studied as sulfur hosts by researchers, such as MnS,[114] SnS_2,[115] FeS_2,[116] NiS_2,[117] CuS[118] *etc*. Although the metal sulifdes have been regarded as promising polar materials to absorb polysulfides, the application of sulfides as host materials is still in its early stages. In addition, like the metal oxides, the conductivity of the metal sulfides is relatively low, and carbon materials are still needed in the cathode. Moreover, the mass loading of active materials in metal oxides/sulfides is low (0.3-1.5 mg cm^{-2}), which is far from the demands of practical application (5 mg cm^{-2}). Therefore, some novel synthesis methods such as chemical vapour deposition (CVD), free-standing cathodes with a high volume ratio or other conductive materials such as metal carbides/nitrides were also explored to further improve the energy density and life-span of Li-S batteries over long cycling.

2.3.2 Modification of separator

The separator is a vital part in various kinds of batteries that is needed to separate the anode and the cathode, to avoid internal short-circuits and to allow ions to pass through. The most commonly used separators are the polyethylene separator (PE), polypropylene separator (PP), and PP/PE/PP three-layer composite separator. Among them, the PP separator has moderate thickness, high porosity, strong anti-oxidation capability and chemical stability, which is widely used in lithium-based batteries. In the case of Li-S batteries, when the PP separator is applied, the soluble intermediate products can easily pass though the pores on the separator to react with lithium anode, leading to lost active materials, the shuttle effect and the corrosion of lithium anode. Therefore, the separator in Li-S batteries directly affects the charge-discharge capacity, cycling stability, and safety performance of the batteries. Therefore, modifying the PP separator or inserting a conductive interlayer between the cathode and the separator can effectively absorb soluble polysulfides to slow down the shuttle effect to improve the electrochemical performance of Li-S batteries.[25, 119] This is because the modified separator or interlayer acts as a fishing net to capture the dissolved polysulfides and enable the trapped active materials to be reused (Figure 2.15).[120] At present, modification of the Li-S battery separator is mainly based on loading various functional materials, such as lightweight carbon materials[121, 122], polymer[123, 124] and metal oxides/sulfides[102, 125], on the separator to physically or chemically absorb polysulfide to reduce the shuttle effect,. Specific examples related to the modified separator or interlayer materials are listed as follows:

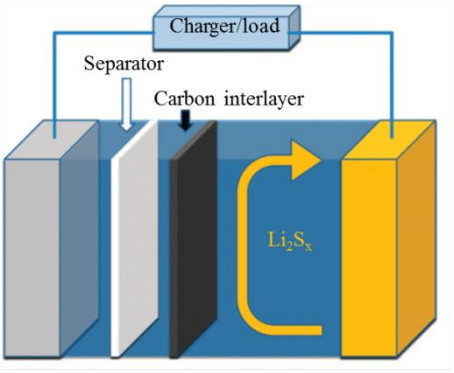

Figure 2.15. Schematic configuration of a Li-S cell with a bifunctional microporous carbon interlayer inserted between the sulfur cathode and the separator.[120]

Carbon material has excellent electrical conductivity, so that it was the earliest materials used as an interlayer to improve the capacity of Li-S batteries. In 2012, the Manthiram group[126] inserted a free-standing multiwall-carbon-nanotube (MWCNT) interlayer between the sulfur cathode and the separator, which could help to improve the cycling stability of Li-S batteries (Figure. 2.16a). The free-standing carbon interlayer served two important functions: (1) suppressing the diffusion of lithium polysulfides to the lithium anode by acting as a polysulfide reservoir and (2) working as an upper current collector to decrease the internal resistance and improve active material utilization. This simple method can dramatically improve the electrochemical performance of the Li-S battery (Figure. 2.16b). Later, their group[127] prepared a hierarchical carbonized paper with outstanding mechanical strength and high liquid absorption capability as a interlayer for intercepting the migrating polysulfide species and then reutilizing the trapped active material in Li-S batteries. The electrochemical results indicated that with 1 layer of carbonized paper, the initial discharge capacity increased from 945 mA h g^{-1} to 1094 mA h g^{-1} at 0.2 C; with 6 layers, the initial discharge capacity reached 1235 mA h g^{-1}, and the utilization rate of active materials increased from 65% to 74%. In addition, the interception mechanism for polysulfides of the hierarchical carbonized paper was

demonstrated by the gradient decrease in the sulfur concentration in the carbon interlayer.

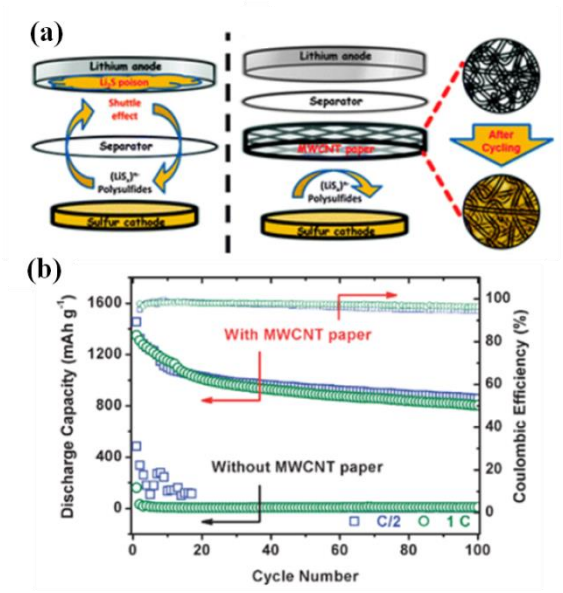

Figure 2.16. (a) Schematic illustration of cell configuration of rechargeable Li-S batteries with the traditional configuration and with the MWCNT interlayer configuration, (b) High-rate cycling performance of the Li-S cells with and without the MWCNT interlayer.[126]

Apart from the interlayer, using various materials directly coated on the commercial separator is a more direct way to suppress the shuttle effect. Compared with the interlayer, the materials were in direct contact with the separator, which could reduce the contact resistance of the whole cell. What is more, this method is simple with no need for preparing free-standing materials. Lin *et al.* [128] coated reduced graphene oxide (rGO) on the separator *via* polyvinylidene fluoride (PVDF) binder. The Li-S battery with the rGO modified separator delivered a discharge capacity of 1067 mA h g^{-1} (0.2 C), and the discharge capacity was maintained at 878 mA h g^{-1} after 100 cycles. This is because the uniform porous structure of the rGO coating layer with rich functional

groups and good electrical conductivity not only relieves the shuttling of polysulfides, but also increases the conductivity of the whole cell.

To further improve the absorptive effect of the separator, materials which could chemically absorb polysulfides, such as polymers and metal oxides/sulfides were also introduced to modify the separator. Ma et al. [129] prepared a polypyrrole nanotube film (PNTF) 35 μm in thickness as a functional interlayer for Li-S batteries, as shown in Figure 2.17a. Because of the adsorption effect between PPy and lithium polysulfides and the conductivity of PPy films, the polymer interlayer can not only significantly decrease the polarization of sulfur cathode, but also can effectively suppress the shuttle effect and the redistribution of the active material during the charge/discharge process. A nickel foam interlayer was also reported by Zhang et al (Figure 2.17b).[130] The nickel interlayer not only acts as a conductive network to enhance the utilization of sulfur, but also acts as a matrix to retain and accommodate the volumetric stress during cycling.

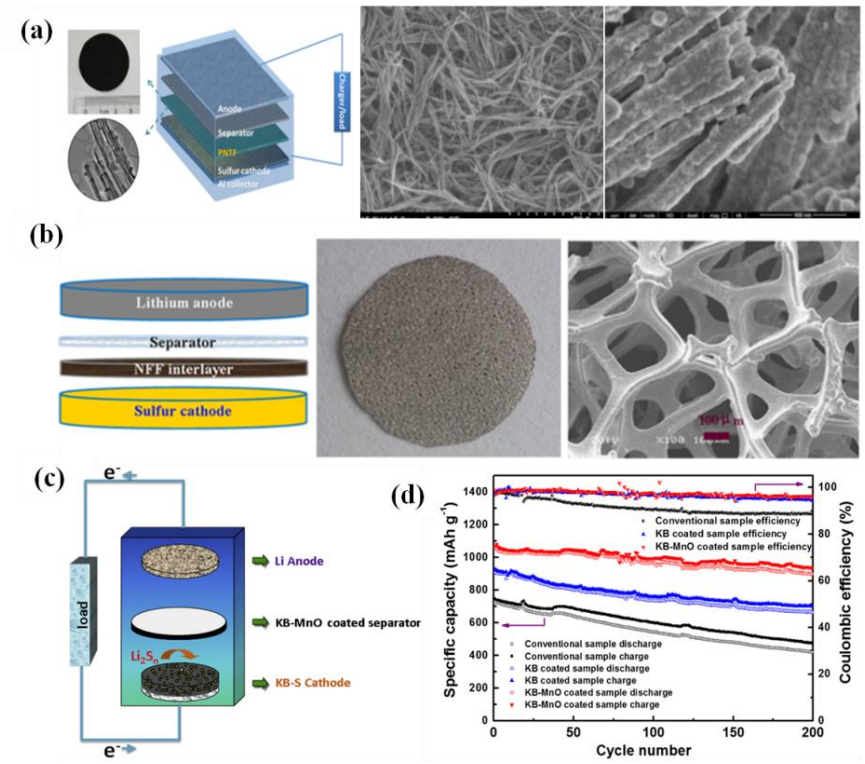

Figure 2.17. (a) PPy nanotube interlayer[129], (b) nickel foam foil interlayer[130], (c) KB-MnO coated separator[131] and (d) cycling performance in Li-S batteries.

Later, Qian et al. [131] prepared a Ketjen black (KB)-MnO composites coated separator for Li-S batteries (Figure 2.17c). Experiments showed that the discharge capacities of the cell using a common separator, a KB coated separator and the KB-MnO coated separator were 723 mA h g^{-1}, 907 mA h g^{-1}, and 1059 mA h g^{-1}, respectively, at 1 C. After 200 cycles, the capacity retention rates were 58%, 73% and 85%, respectively (Figure 2.17d). The specific surface areas of KB and KB-MnO are similar, but the Li-S batteries with the KB-MnO coated separator had better electrochemical performance than that with KB, because the MnO can absorb more polysulfide because the oxygen atom in MnO can be chemically bound with polysulfides.

Modifying the separator or inserting an interlayer between the cathode and the separator is regarded as a simple and promising way to overcome the shuttle effect and improve

the cycling stability of Li-S batteries, although these strategies is still in their early stages and only a few kinds of materials were applied. The dynamics of the modified separator/interlayer is also not fully understood as yet. Therefore, exploring rational materials and applying operando techniques are highly required to realise advanced Li-S batteries.

2.3.3 Electrolyte system

In Li-S battery systems, the electrolyte is a very important component. The main function of the electrolyte is to transfer lithium ions between the positive and negative electrodes. For Li-S batteries, However, since various forms of polysulfides formed during the discharge-charge process could react with most organic electrolytes, the selection of organic solvents for the Li-S system is narrow. Recently, attention and research on Li-S battery electrolytes have gradually increased,[39, 40, 132, 133] mainly including liquid-phase electrolytes, solid-state electrolytes and ionic liquid electrolytes.

Liquid-phase electrolytes: In terms of liquid-phase electrolytes, the carbonates solvents commonly used in conventional lithium ion batteries are not suitable for Li-S batteries because of their high irreversible reactivity with polysulfides species, causing severe loss of active material and capacity decay.[134] In 2012, however, Xin et al.[49] reported the confinement of small sulfur molecules of S_{2-4} in a conductive microporous carbon matrix, which could work well with the carbonate-based electrolytes. This may be because the small sulfur molecules will not be reduced to long-chain polysulfides during cycling, which can be confirmed by the discharge profiles, which only show lower plateaus under 2 V. Other research papers also showed that the small size sulfur confined in micropores could perfectly work with carbonates solvent due to the disappearance of the upper plateau related to the formation of dissolved polysulfides.[135,

[136] Nevertheless, the reaction mechanism of polysulfides with carbonate solvents still needs to be investigated and confirmed.

At present, the liquid-phase electrolytes that are mostly applied in Li-S batteries are mainly ether-based solvents due to their low viscosity, including 1,3-dioxolane (DOL) and 1,2-dimethoxy ethane (DME).[137] DOL has a low dipole moment and can help to form a solid electrolyte interphase on the anode surface, but has relatively low polysulfide solubility. In contrast, DME has high dielectric permittivity and could dissolve a large amount of Li-based salts for high ionic conductivity. Single component solvent systems have typically shown poor electrochemical performance, however, and typically, combining two solvents together can yield high specific capacity and stable cycling performance.[138, 139]

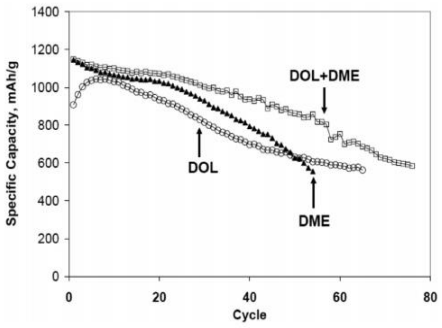

Figure 2.18. The cycling performance of Li-S batteries with different electrolyte solvents.[138]

Solid-state electrolytes: If a solid-state electrolyte is used in Li-S batteries, the cycling performance can be improved to some extent. Up to now, poly(vinylidene fluoride-co-hexafluoropropylene)[140] and $PEO_{20}LiCF_3SO_3$ + 10 % ZrO_2 electrolyte[141], where PEO is polyethylene glycol, have been tested in the Li-S battery systems as gel electrolytes. Various glass ceramics have been used as the solid-state electrolytes, such as Li_2S-P_2S_5 and Li_2S-GeS_2-P_2S_5 glass compounds.[142, 143] This is because the solid

electrolyte could reduce the dissolution and diffusion of intermediates products, suppress the shuttle effect, improve the utilization of active materials, and protect the lithium anode from corrosion, thus enhancing the capacity and life-span of Li-S batteries. Meanwhile, the solid-state electrolyte can also function as a separator. Because, solid-state electrolytes have poor ionic conductivity at room temperature, Li-S batteries using solid electrolytes require higher operating temperatures, which is not possible due to the low melting point of sulfur. So, the discharge capacity and rate performance of Li-S batteries with solid electrolytes at room temperature need to be further optimized. In addition, the solid electrolyte usually has a high over-potential, resulting in low energy efficiency. Therefore, the usage of solid-state electrolytes in Li-S batteries has a long way to go.

Ionic liquid electrolytes: Another kind of electrolyte used in Li-S batteries is the ionic liquids electrolyte. Due to the high viscosity, poor wettability, and high cost of ionic liquid electrolyte, however, it is not widely accepted at present, although mixing an ionic liquid with an ether solvent has been shown to improve the thermal stability and ionic conductivity of the electrolyte.[144, 145]

In terms of the lithium salts, $LiCF_3SO_3$, $LiN(CF_3SO_2)_2$ and $LiClO_4$ are commonly used as lithium salts that are added into organic solvents to produce the electrolytes for Li-S batteries, which all have good stability and ionic conductivity. Kim et al.[146] compared the effects of different salts in DOL-DME solvent on the cycling performance of Li-S batteries, and the results are shown in Figure 2.19a. As expected, lithium bis(trifluoromethanesulfonyl)imide (LiTFSI) shows the best cycling performance, and specifically the best initial discharge capacity and capacity retention compared to the

other salts, due to its high ionic conductivity in DOL-DME solvent and its having the highest donor number. Apart from the lithium salts, $LiNO_3$ has been usually included in the into electrolyte as an additive for Li-S batteries,[147] Studies have shown that lithium nitrate can produce a passivation film on the lithium anode,[148] effectively protecting the Li electrode and improving the coulombic efficiency (Figure 2.19b). This is because $LiNO_3$ can help to form a stable solid electrolyte interphase (SEI), which could prevent the reaction of the polysulfides with lithium and alleviate the shuttle effect.[149]

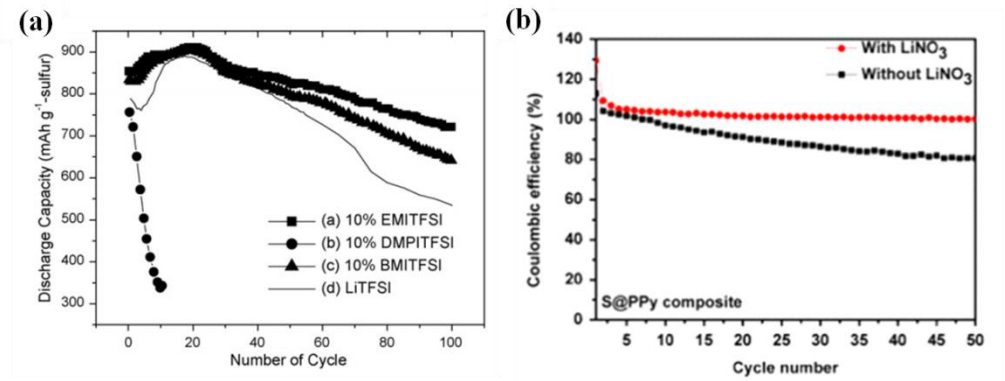

Figure 2.19. (a) Cycling performance of Li-S batteries with different lithium salts in DOL/DME solvent[146]; (b) Coulombic efficiency of sulfur cathode with and without $LiNO_3$ additive in the electrolyte [149].

2.3.4 Lithium anode

Lithium metal has a very high energy density (3860 mA h g^{-1}) a very low electrochemical potential (-3.040 V vs. standard hydrogen electrode (SHE,)), and was the first anode material used in the secondary battery systems. There are several challenges that have limited the commercialization of lithium metal anode, however, including dendrite formation, an unstable SEI, and severe volume changes, which can

lead to safety issues, low coulombic efficiency, and short cycling life. In the case of Li-S batteries, there is another problem related to the lithium anode. The dissolved polysulfides can pass through the separator and react with lithium to be reduced to shorter-chain polysulfides. If the polysulfides are reduced to Li_2S_2/Li_2S, it can be deposited on the surface of the lithium anode to form a nonconductive layer that will stop any further reaction of sulfur with lithium. Therefore, various strategies should be adopted to overcome these drawbacks.[150-152] This section mainly reviews some suggestive research efforts made towards protecting the lithium anode to improve the electrochemical performance of Li-S batteries.

One of the most used methods to protect the Li anode in the Li-S battery is to stabilize the solid electrolyte interphase (SEI), for example, by adding $LiNO_3$ into the ether-based electrolyte.[153] Although the $LiNO_3$ can help to form a SEI on the lithium anode, the lithium dendrite will continuously grows during long-term cycling and the SEI is not sufficient to protect the lithium anode. Ding et al.[154] demonstrated a self-healing electrostatic shield mechanism (SHES) to alter dendrite formation by adding cation (such as cesium or rubidium), which lead to a lower reduction potential than that of lithium ions. During the initial deposition process, the lithium ions (Li^+) and additive ions (M^+) will both be adsorbed on the lithium anode suface (Figure 2.20a). Li^+ will agglomerate together to form some protuberant tips due to the fluctuations on the lithium foil (Figure 2.20b). Due to the lower reduction potential, the M^+ will be accumulated in the vicinity of the tips to form a electrostatic field (Figure 2.20c-d), which could prevent the Li^+ from being continuously deposited on the tips, but rather causes it to be preferentially deposited around the tips (Figure 2.20e) until a smooth deposition layer is formed on the surface of lithium anode (Figure 2.20f). The Scanning

electron microscope (SEM) images of lithium anode are presented in Figure 2.20g and h. A dendritic and mossy film was deposited on the lithium surface in the normal electrolyte, while a smooth Li film was obtained after adding the M^+ into the electrolyte. These phenomena indicate that the added M^+ will not be consumed during cycling and will be effective for many cycles. In addition, this strategy can be used in other metal-based batteries. The coulombic efficiency is relatively low, However, due to the unstable SEI layer formed on the surface of the lithium anode.

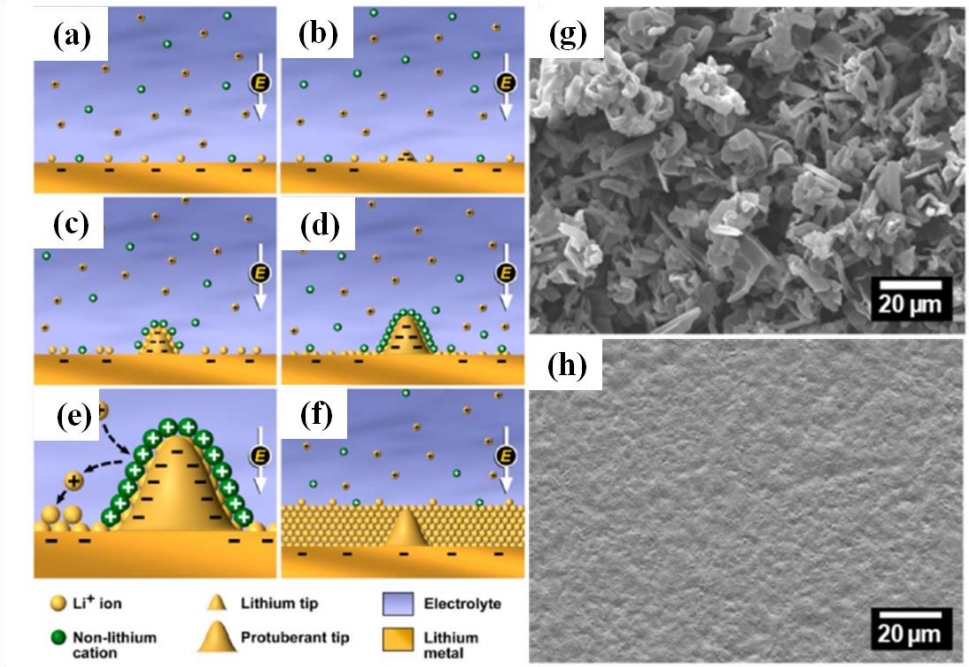

Figure 2.20. (a-f) Schematic illustration of Li deposition process based on the SHES mechanism, SEM images of the morphologies of Li films deposited in electrolyte composed of 1 M $LiPF_6$/PC with $CsPF_6$ concentrations of (g) 0 M and (h) 0.01 M at a current density of 0.1 mA cm^{-2}.[154]

Apart from modifying the electrolyte system, preparing lithium composites is another promising method to protect the lithium anode. Zhang et al.[155] used Li-B alloy to suppress the formation of lithium dendrites and improved the cycling and safety

performance of their Li-S batteries. The unique structure of the Li-B alloy allows it to be embedded in lithium to form a stable Li_7B_6 sponge structure. Li_7B_6 can crystallize lithium and promote the formation of SEI film. This sponge structure can protect most alloy materials from material deformation caused by volume expansion during cycling. Cui et al. reported reduced graphene oxide (rGO) with nanoscale interlayer gaps as a stable host for lithium anode.[156] Due to its excellent mechanical properties, the rGO could significantly mitigate the volume change of lithium during cycling. Moreover, the rGO with its large surface area could provide a electrochemically and mechanically stable artificial interface to stabilize the SEI after formation. Owing to these merits, the Li-rGO anode exhibited stable voltage profles with little hysteresis, and flat voltage plateaus were observed throughout the cycling. At the same time, this group also prepared a polyimide matrix for the lithium anode,[157] which could effectively suppress the volume changes and provide stable cycling performance under high current density (5 mA cm^{-2}). Therefore, preparing the lithium host materials enabled uniform lithium stripping /plating within the matrix, minimizing the volume changes and avoiding dendrite formation.

Some scientists have proposed using other new anode materials instead of lithium anodes to solve the above problems. Wan et al.[158] used electrochemically prelithiated Si/C microspheres as the anode material and C/S as the cathode material with a room-temperature ionic liquid (RTIL) electrolyte, n-methyl-n-allylpyrrolidinium bis(trifluoromethanesulfonyl)imide (RTIL P1A3TFSI). The electrochemical performance of the resultant Li-S battery is shown in Figure 2.21. It delivered an initial discharge capacity of 1457 m Ah·g^{-1}, and a reversible capacity of 926.4 m Ah g^{-1} with the capacity still maintained at 670 m Ah g^{-1} after 50 cycles. The Si/C anode and ionic liquid electrolyte were well matched, and the output voltage of each cell was 1.5 V,

showing the potential to replace the widely used alkaline batteries. Although the cycling performance is still poor, this prelithiated Si/C anode can effectively solve the safety problem related to the Li-S battery anode.

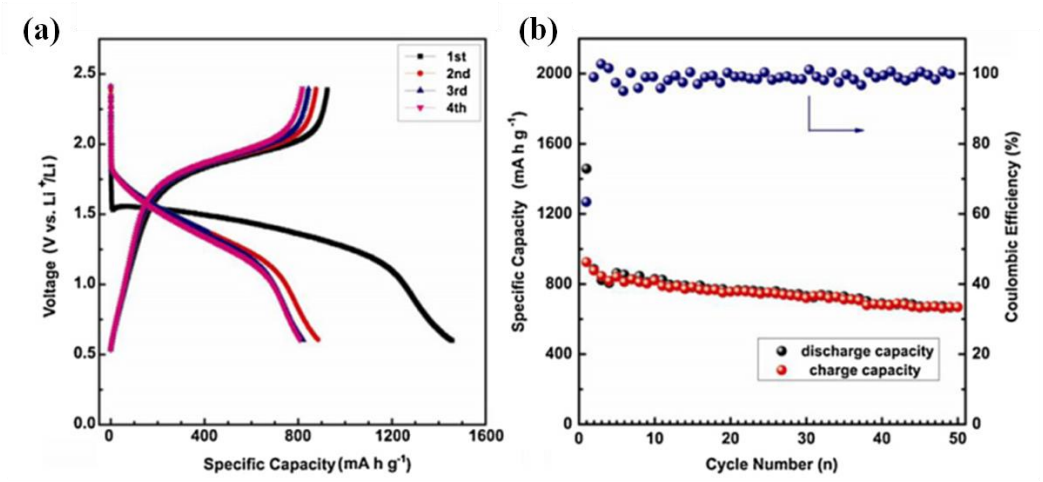

Figure 2.21. (a) Discharge-charge profiles and (b) cycling performance of Li-S battery composed of prelithiated Si/C anode and S/C cathode.[158]

2.3.5 Li_2S cathode materials

Recently, the use of lithium sulfide cathodes instead of sulfur has been attaching great attention due to their many advantages.[30, 159-163] For example, it is fully lithiated and can be paired with non-lithium metal anodes (silicon, tin, or carbon), avoiding the formation of lithium dendrites and safety concerns related to metallic lithium; it has a high theoretical specific capacity (1166 mAh g^{-1}); unlike sulfur with volume expansion of about 80% during lithiation, Li_2S shrinks as it is initially delithiated, generating empty space for subsequent volumetric expansion during lithiation; and Li_2S has a much higher melting point (938 ˚C) compared to that of sulfur (115 ˚C), which make it easier to synthesize Li_2S-conductive matrix composites. There are also some drawbacks faced by the Li_2S cathode materials, however, such as, the low electronic and ionic conductivity of Li_2S, similar to that of sulfur, the high initial barrier at the first charge

process, and its high sensitivity to moisture and the dissolution of intermediate products, all of which have inhibited the rapid development of Li_2S cathode. This section mainly summarizes the recent breakthroughs made on the Li_2S cathode for Li-S batteries.

Due to the insulating nature of Li_2S in terms of both electrons and ions, Li_2S was firstly considered as an electrochemically inactive material. Nevertheless, in 2010, Cui and co-workers[164] filled Li_2S into the mesopores of CMK-3 carbon particles to make a cathode material for Li-S batteries, which delivered a discharge capacity of 573 mA h g^{-1}. In addition, a full cell based on Li_2S/CMK-3 cathode and $LiCoO_2$ anode was assembled to avoid the safety concerns relating to the metal lithium anode, and it worked successfully, although the cell experienced serious capacity fading. From then on, various kinds of carbonaceous materials were widely studied as the host materials for Li_2S to improve the cycling stability of Li_2S cathode, such as graphene oxide[165], carbon nanotube[166], and mesoporous carbon[167]. With these host materials, by preparing nanostructured Li_2S using the chemical method, it was usually possible to obtain a uniform dispersion of Li_2S in the conductive matrix and improve the electrochemical performance of Li_2S cathode. For example, Wu and co-workers[168] designed and synthesized a Li_2S/few-walled carbon nanotubes@reduced graphene oxide nanobundle forest (Li_2S/FWNTs@rGO NBF) by directly annealing the Li_2SO_4/FWNTs@GO NBF, as shown in Figure 2.22a. The FWNT skeleton and rGO coating acted together as a pathway for fast electron transport and prevented the loss of active materials, with the 3D structure providing effective ion diffusion channel (Figure 2.22b-d). As a result, the designed Li_2S/FWNIs@rGO NBF cathode was able to achieve a high initial capacity of 980 mA h g^{-1} at 0.2 C with impressive capacity retention of 89% after 300 cycles and an unprecedented reversible capacity of 433 mA h g^{-1}, even at the high rate of 10 C (Figure 2.22e).

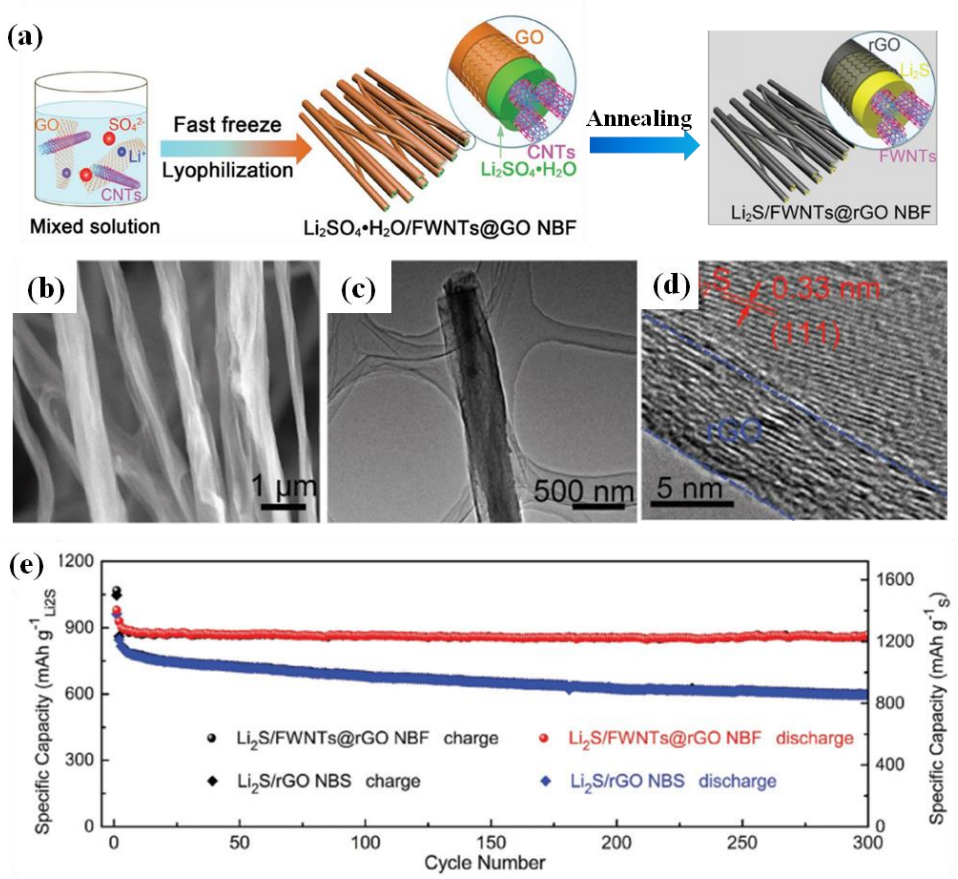

Figure 2.22. (a) Schematic illustration of the synthesis, and (b) SEM, (c) TEM, and (d) HRTEM images of Li_2S/FWNTs@rGO NBF; (e) Cycling performance of the Li_2S/FWNTs@rGO NBF cells in comparison with Li_2S/rGO NBS cells at 0.2C.[168]

In 2012, Yi Cui's group[169] discovered that there was a large potential barrier (~1 V) in the initial charge process (Figure 2.23), which can be ascribed to the new phase nucleation (polysulfides in this system). The amplitude of the barrier is related to the electronic conductivity of Li_2S and the charge transfer process at the surface of Li_2S particles. Li_2S is an ionic crystal, and the strong bonding between Li^+ and S^{2-} ions makes it very difficult to extract Li^+ from Li_2S and move it into the electrolyte because the bonding environment for Li^+ changes drastically from Li_2S to the electrolyte. Once the polysulfide exists in the electrolyte, due to the similar Li^+ environment between Li_2S and lithium polysulfides, it become easier to extract Li^+ from Li_2S and move it into the

electrolyte via lithium polysulfides, which indicates that the barrier is related to the polysulfide nucleation. Fortunately, the potential barrier can be overcome by applying a high cut-off votage (usually >3.5 V). In addition, after the initial activation, the potential barrier will not appear again in the subsequent charging process.

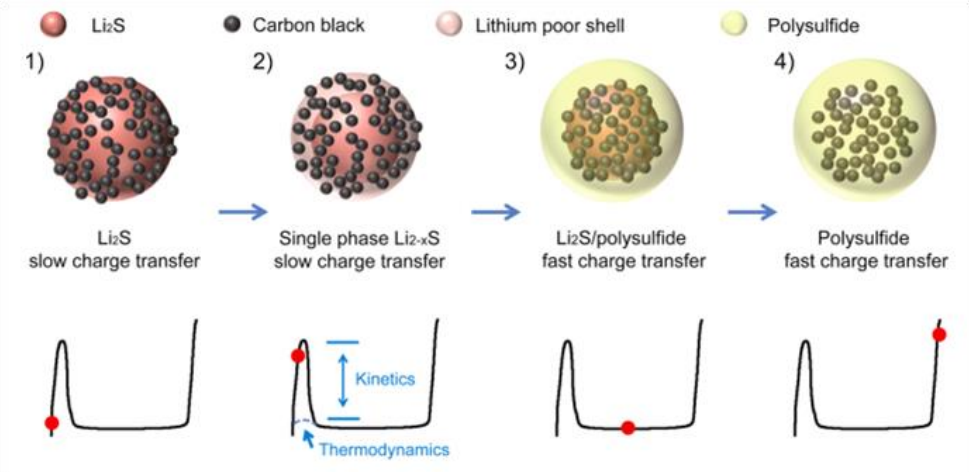

Figure 2.23. Summary of the model for the initial charging of Li_2S. Before reaching the top of the potential barrier, $Li_{2-x}S$ exists as a single phase with a lithium-poor shell on the surface. In step 2, the shell is highly lithium deficient while the core remains in near stoichiometry. In step 3, soluble polysulfides are formed after overcoming the initial barrier, shown as the yellow part around the solid Li_2S particle. Consequently, the kinetics is significantly improved. At the end of charging, only the polysulfide phase exists with fast kinetics. [169]

After this discovery, researchers were dedicated to exploring bifunctional catalyst materials to decrease the potential barrier and chemically adsorb polysulfides as well.[170-173] Recently, Yu and co-workers[174] synthesized a binder-free Li_2S/nitrogen, phosphorous doped carbon (Li_2S/N,P-C) electrode by simultaneously reducing Li_2SO_4 to Li_2S in the carbonization process. The porous 3D architecture of N and P codoped carbon provides continuous pathways for electron and Li ion transport. Moreover,

phosphorus doping can also suppress the shuttle effect through the consequent strong interaction between polysulfides and the carbon framework, resulting in stable cycling performance. Meanwhile, P doping in the carbon framework plays an important role in catalysing the redox reactions of polysulfide species, improving the reaction kinetics, and reducing electrochemical polarization. As a result, the Li_2S/N,P-C electrode delivered a stable capacity of 700 mA h g^{-1} over 100 cycles at 0.1C.

Metal sulfides are widely used in S cathodes to suppress the shuttle effect and improve the cycling stability of Li-S batteries, which has been already summarized in section 2.3.1. Recently, Cui's group[163] investigated a series of metal sulfides as catalysts to identify the key parameters determining the energy barrier for Li_2S oxidation and polysulfide adsorption (Figure 2.24a). Their calculated and experimental results indicated that the Li_2S decomposition energy barrier is associated with the binding between isolated Li ions and the sulfur in sulfides (Figure 2.24b-d). The inherent metallic conductivity, strong interaction with LiPSs, facilitated Li ion transport, controlled Li_2S precipitation, accelerated surface mediated redox reaction, and catalysing the reduction/oxidation capability of M_xS_y are critical for reducing the energy barrier and contributing to the remarkably improved battery performance. The VS_2-, TiS_2-, and CoS_2-based cathodes exhibited higher capacity, lower overpotential, and better cycling stability compared with pure carbon materials and other metal sulfide-added electrodes. This paper sheds light on preparing rational materials that can reduce the potential barrier of Li_2S and adsorb polysulfides via strong chemical bonding.

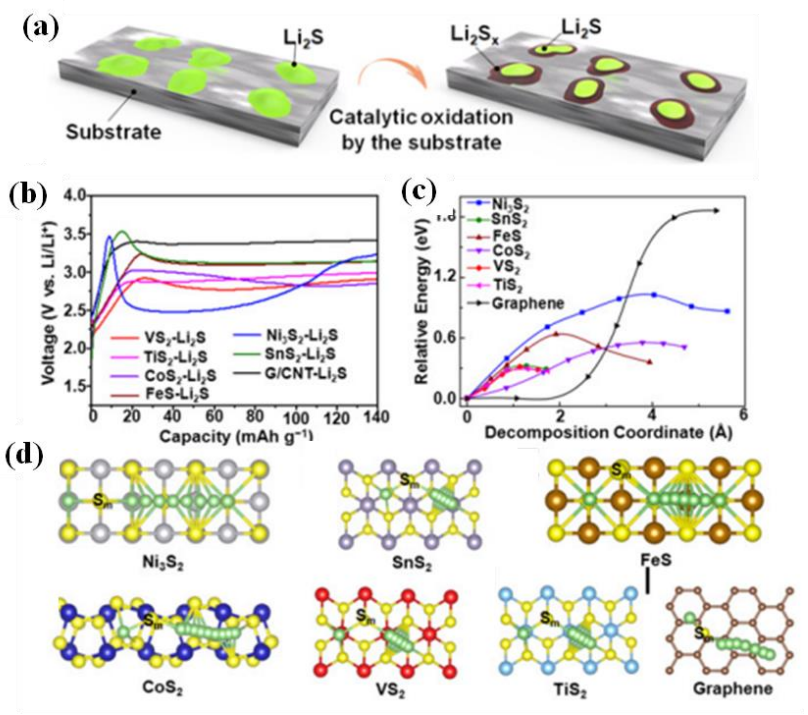

Figure 2.24. (a) Schematic illustration of the metal sulfides catalysing Li_2S decomposition and favouring the oxidization of Li_2S to Li_2S_x; (b) first cycle charge voltage profiles of Li_2S based on different metal sulfides electrodes and graphene, (c) energy profiles for the decomposition of Li_2S clusters on different metal sulfide and graphene, (d) top view schematic representations of the corresponding decomposition pathways for different metal sulfides and graphene.[163]

Although, Li_2S cathode materials have attracted much attention due to their numerous advantages, the synthesis methods used in these reports are relatively complicated, which is not suitable for practical application. In addition, even though a Li_2S cathode can be paired with a lithium-free anode (such as Si, Sn, or C) to avoid the safety concerns related to metal lithium, there are only few reports on assembled full cells.[164, 175-178] Therefore, substantial exploration is required to achieve better electrochemical performance of Li_2S cathode and promote the real commercialization of Li-S batteries.

CHAPTER 3 EXPERIMENTAL

In my doctoral work, different synthesis methods were applied to synthesize sulfur-based cathode materials, such as the chemical polymerization/deposition method to prepare S@PPy composites, the solvothermal method to prepare S/graphene composites and Li_2S/N-doped carbon nanofibers, and the ball milling method to prepare Li_2S-PPy hybrid. After obtaining the samples, some physical characterizations were made to confirm the structural and physical properties of the as-prepared samples. Finally, these samples were used to make electrodes and conduct the electrochemical measurements. For some samples, the morphology of lithium, separator or cathodes were also investigated after electrochemical cycling tests. The whole experimental process is shown in Figure 3.1.

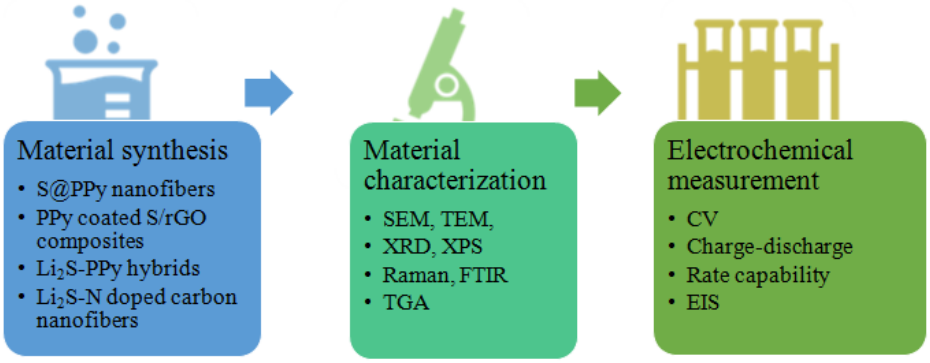

Figure 3.1. Outline of the experimental procedures and characterization techniques used in this thesis.

3.1 Chemicals and materials

The main chemicals and materials used in my experiments are listed in Table 3.1 along with the formulas, suppliers, and purity. The materials were all used without any purification except for the pyrrole.

Table 3.1. Chemicals and materials used in this thesis

Materials/Chemicals	**Formula**	**Purity (%)**	**Supplier**
1,3-dioxolane	$C_3H_6O_2$	99	Sigma Aldrich, Australia
1-methyl-2-pyrrolidinone (NMP)	C_5H_9NO	99.5	Sigma Aldrich, Australia
Acetone	CH_3COCH_3	99	Sigma Aldrich, Australia
Ferric salt iron (III) p-toluenesulfonate	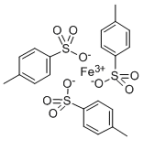	98	Sigma Aldrich, Australia
Aluminium foil	Al	N/A	China
Carbon black	C	N/A	Timcal, Belgium
CR2032 type coin cells	N/A	N/A	China
Dimethoxy ethane	$C_4H_{10}O_2$	99	Sigma Aldrich, Australia
Ethanol	C_2H_5OH	Reagent	Q-store, Australia
Hypophosphorous acid	H_3PO_2	50	Sigma-Aldrich, Australia
Ammonium persulfate	$(NH_4)_2S_2O_8$	98+	Sigma-Aldrich, Australia
Hydrochloric acid	HCl	36.5	Sigma Aldrich, Australia

Lithiumbis(trifluoromethanesulfonyl)imide (LiTFSI)	$CF_3SO_2NLiSO_2CF_3$	N/A	Sigma Aldrich, Australia
Lithium metal	Li	99.9	Sigma Aldrich, Australia
Lithium nitrate	$LiNO_3$	99	Sigma Aldrich, Australia
Hexadecyl trimethyl ammonium bromide (CTAB)	$C_{19}H_{42}BrN$	99+	Sigma Aldrich, Australia
Lithium sulfides	Li_2S	99.9	Sigma Aldrich, Australia
n-Butyllithium	C_4H_9Li	99	Sigma Aldrich, Australia
Polypropylene separator	$(C_3H_6)_n$	Celgard 2500	Hoechst Celanese
Polyvinylidene difluoride (PVDF)	$(CH_2CF_2)_n$	N/A	Corporation, USA
Pure ethanol	C_2H_5OH	99.9	Sigma Aldrich, Australia
Monomer pyrrole		98	Sigma Aldrich, Australia
Singled-Walled CNT	C	99	Sigma Aldrich, USA
Sodium thiosulphate	$Na_2S_2O_3$	99	Nanocore, USA
Sodium p-toluenesulfonate	$CH_3C_6H_4SO_3Na$	95	Sigma Aldrich, Australia

Sulfur	S	99.5	Sigma Aldrich, Australia
Triton X-100	$C_{34}H_{62}O_{11}$	99	Sigma Aldrich, Australia

3.2 Materials preparation

3.2.1 Chemical precipitation

Chemical precipitation is one of the basic methods for preparing ultrafine powders. The various precursors dissolved in solvent are chemically reacted to form insoluble precipitates. The precipitate is then separated by centrifugation, washing, drying, or subsequent heat treatment to obtain the desired products. The chemical precipitation method has the characteristics of high purity, simple operation, good stoichiometry, low requirements on reaction equipment, and low cost, which makes it suitable for industrial production. In the chemical precipitation method, the concentration and type of precursors will affect the size and morphology of the products. By adjusting the concentration and kind of precursors, deferent sizes and morphologies products can be obtained.

In this thesis, the S@PPy nanofibers and the Li_2S coated N-doped carbon nanofibers were all synthesized using this method. The chemical reactions are shown below:

$$Na_2S_2O_3 + 2HCl \rightarrow 2NaCl + S\downarrow + H_2O + SO_2\uparrow \quad (3.1)$$

$$\text{n-Butyllithium} + S \rightarrow Li_2S\downarrow + \text{hydrocarbons} \quad (3.2)$$

3.2.2 Polymerization reaction

Polymerization is a process for converting low molecular weight monomers into high molecular weight polymers. The polymers have important properties such as plasticity, high conductivity, and fibre or film morphology, which are not possessed by low molecular weight monomers, so that they can be widely used as flexible substrates. Various polymerization mechanisms exist due to the different functional groups and their inhibition of steric effects. Normally, there are two kinds of polymers: homopolymers and copolymers. The homopolymers consist of only one type of monomer unit, while the copolymers consists of more than one type of monomers unit, as shown in Equations (3.3) and (3.4).[179]

$$\text{Homopolymers: } A + A + A \ldots \rightarrow AAA \ldots \quad (0.3)$$

$$\text{Copolymers: } A + B + A \ldots \rightarrow ABAB \quad (0.4)$$

A catalyst is needed in the polymerization method to trigger this reaction. In Chapters 4 and 7, the PPy nanofibers were prepared by the chemical polymerization method. In this method, ammonium persulfate (APS) was used as an oxidant and a surfactant cetyltrimethylammonium bromide (CTAB) was also used. In Chapter 5, an organic trivalent iron salt was chosen to oxidize pyrrole monomer to obtain a thin film layer on the surface of S/rGO composite.

3.2.3 Ball milling method

Mechanical ball milling is a method in which mechanical energy is to induce changes in the organization, structure, and properties of materials or to induce a chemical reaction to produce a designed product. The mechanical ball-milling method is simple in operation and is an energy-efficient preparation technology. It can refine the particles of

a material and improve the size distribution of powder particles, thereby changing the electrochemical activity of the material. According to the energy of the grinding ball, the mechanical ball milling method is divided into the energy ball-milling method and the planetary ball-milling method. In Chapter 6, planetary ball-milling is used to prepare Li_2S-PPy composites. The main purpose of this method was to uniformly disperse Li_2S in the PPy nanofiber matrix, thus improving the conductivity of the cathode materials and suppress the dissolution of LiPSs.

3.3 Structural and physical characterization

3.3.1 X-ray diffraction

X-ray diffraction (XRD) is a commonly used technique for characterizing the phase composition and crystal structure of materials based on their diffraction patterns. The working principles of XRD are illustrated by Figure 3.2. X-rays are a type of electromagnetic radiation generated by the transitions of atomic inner electrons under the impact of high-speed moving electrons, and mainly include continuous X-rays and characteristic X-rays. When the X-rays hit the surface of a crystals, the crystal acts as a gratings for X-rays, and the X-rays are scattered by each set of lattice planes at a unique angle, which is called elastic scattering. Since every crystal features a set of unique *d*-spacings, the pattern has a functional relationship with the crystal structure, which is described by Bragg's law (Equation 3.5):

$$n\lambda = 2d\,sin\,\theta \qquad (3.5)$$

Where n is an integer, λ is the wavelength of the incident X-ray beam, d is the lattice spacing of the given crystal, and θ is the incidence angle. The crystal structure of the

sample is analyzed based on the diffraction angle and relative intensities of the diffraction peaks.

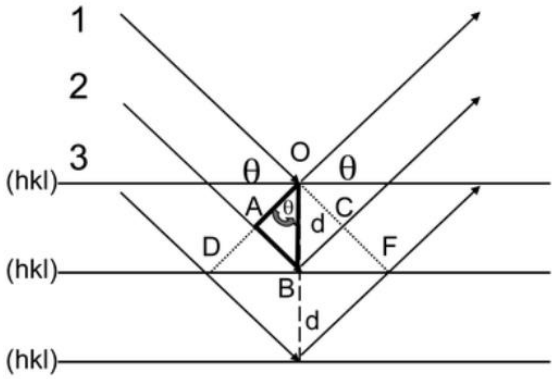

Figure 3.2. Bragg's law can be derived from the geometrical relation between the interplanar spacing *d* and the diffraction angle *θ*.[180]

In this doctoral work, all the XRD measurements were performed using a GBC MMA X-ray generator and diffractometer with Cu Kα radiation (λ = 1.5406 Å). The working voltage and current were 40 kV and 25 mA, respectively.

3.3.2 Raman spectroscopy

Raman spectroscopy is a powerful tool to investigate the structure of a material. The incident light used in Raman spectroscopy is monochromatic light, which is produced by a laser. When the incident light hits the sample, some of the light is scattered. In the scattered light, the frequencies of some of the light are different from the frequency of the incident light because the incident photon exchanges energy with a vibration group in the sample. This phenomenon is called the Raman effect. The scattered line located in a lower frequency region than that of the incident light is called the Stokes line, while the scattered line located in a higher frequency region than that of the incident light is called the anti-Stokes line. The Stokes line is the main recorded line in the Raman

spectrum. Therefore, the Raman spectrum reveals the special chemical compositions and structures of samples, which is a complementary technique to XRD. In this doctoral work, the Raman spectroscopy was performed using a JOBIN YVON HR 800 Horiba Raman spectrometer with the laser wavelength at 632.8 nm. A neutral density filter was applied to adjust the laser intensity in the measurements.

3.3.3 Fourier transform infrared spectroscopy

Fourier Transform Infrared Spectroscopy (FTIR) is a commonly used method to analyze the vibration groups in samples. When the infrared light illuminates the sample, the sample will absorb the infrared light which has the same frequency as that of a vibration group in the sample, which causes the transmission intensity of the infrared light to decrease. The changes will be recorded by an infrared spectrum. Every vibration group has a special vibration frequency, which means that analyzing the absorption band in the infrared spectrum will give information on the vibration groups in the sample. The vibrations in the sample include stretching vibration and bending vibrations. Stretching vibration refers to the vibration of the bonding atoms in the direction of the key axis, which changes its length. Bending vibration refers to the vibration of the bonded atoms away from the bond axis, which causes the bond angle to change. In this doctoral work, FTIR spectra were collected on a Shimadzu IRPresting-21 model Fourier transform infrared spectrometer. For measurements, the sample materials were mixed with potassium bromide (KBr) powder, which acts as the background, and pressed in a die with a barrel.

3.3.4 X-ray photoelectron spectroscopy

X-ray photoelectron spectroscopy (XPS) is a surface-sensitive quantitative spectroscopic method to analyse the surface chemistry of a material. When X-rays are

used to irradiate the surface of a sample, the electrons in the atoms of the sample will be excited and can escape from the atom as photoelectrons. The process can be expressed by the following formula:

$$h_n = E_k + E_b \,, \qquad (3.6)$$

where h_n is the energy of the X-ray photons; E_k is the energy of the photoelectron; E_b is the binding energy of the electron. If we can know the h_n and E_k, the binding energy can be calculated. Every atomic orbital has its own special binding energy and therefore, by measuring the energies of the photoelectrons produced by the sample, the composition of the elements in the sample can be known. In this doctoral work, XPS analysis was conducted on a VG Scientific ESCALAB 2201XL system using Al Kα X-ray radiation and fixed analyzer transmission mode. A commercial XPS 2.3.15 software package was used to analyse the XPS data. All the spectra were calibrated by C 1s = 284.6 eV.

3.3.5 Thermogravimetric analysis

Thermogravimetric analysis (TGA) is a method to study the composition and structure of materials by analyzing the mass changes during a heating process. In this doctoral work, TGA was used to measure the content of sulfur in the whole cathodes. When the temperature reaches its melting point, sulfur will evaporate from the surface of host materials, causing a decrease in the mass of the sufur composites. According to the thermogravimetric curve, the mass reduction at the corresponding temperature can be ascribed to the loss of sulfur content. TGA was carried out by using a SETARAM Thermogravimetric Analyzer (France).

3.3.6 UV-Visible spectroscopy

Both the ultraviolet (UV) absorption spectrum and the visible absorption spectrum of a substance belong to its molecular spectrum, which is entirely due to the transitions of valence electrons. The location and intensity of the UV-visible spectrum generated by the absorption of ultraviolet and visible light by molecules or ions of a substance can be used to analyze the composition, content, and structure of the substance. In this doctoral work, UV-visible spectroscopy was used to analyze the adsorption on host materials of the dissolved lithium polysulfides.

3.3.7 Scanning electron microscopy (SEM)

Scanning electron microscopy is a method for discovering the surface morphology and composition distribution of a sample by scanning the sample using a high-energy beam of electrons. The electron beam and the sample interact to generate various signals such as secondary electrons, back-scattered electrons (BSE), characteristic X-rays, light (cathodoluminescence), and transmitted electrons. These signals are detected by the detector and converted into electrical signals, which are amplified to obtain an image. The obtained images provide information on the morphology, composition, and distribution of structures on the sample surface. The resolution of the images can be up to 1 nm when the detectors for secondary electrons are installed in the SEM system.

Some other detectors, such as for energy-dispersive X-ray spectroscopy (EDS) are usually installed in the SEM system, which can provide further specific charaterization of samples. EDS could give information on the presence of different elements and their distribution in the sample. In this doctoral work, a field-emission scanning electron microscope (FE-SEM, JEOL JSM-7500FA, 15 kV) was used to characterise the morphologies of materials. Before SEM observation, the powdered material was

directly applied on carbon conductive tape, which was mounted on an aluminium holder.

3.3.8 Transmission electron microscopy

Transmission electron microscopy (TEM) is another technique to analyze the morphology, lattice spacing, crystal orientation, and electronic structure of sample materials. Unlike SEM, TEM provides the morphology of a sample through transmission because the electron beam will penetrate the sample and the transmitted electrons are magnified and collected to produce an image. The difference in density and thickness of the various parts of the sample produce contrast in the electronic image, which corresponds to the internal structure of the sample. The samples investigated by transmission electron microscopy need to be very thin, so that the electron beam can penetrate the sample. The preparation of the powder particles is relatively easy: the powder particles in a solution are dispersed by ultrasonic treatment, and then the solution is dropped onto the carbon-film-covered copper grid of the electron microscope. After the solvent is volatilized, a powder particle sample is obtained. Like SEM, detectors for energy-dispersive X-ray spectroscopy (EDS) are usually installed in the TEM system to analyze the element distribution.

In this doctoral work, the TEM observations were carried out on a JEOL 2011 TEM (200 keV) and a JEOL ARM-200F TEM (200 keV).

3.4 Electrode preparation and coin-cell assembly

To prepared the electrodes, the active materials, Super P carbon and poly(vinylidene fluoride) (PVDF) were mixed together in a mass ratio of 8:1:1 in

N-methyl-2-pyrrolidinone (NMP) solvent to form a slurry. The resultant slurries were coated on aluminum foil and dried in a vacuum oven at 60 °C overnight.

The cells were assembled in an argon-filled glovebox (Mbraun, Unilab, Germany) with H_2O and O_2 levels below 1 ppm. CR2032 coin type cells and a commercial polypropylene separator were used. Lithium foil was used as counter electrode. The electrolyte was 1 M lithium bis(trifluoromethanesulfonyl)imide (LiTFSI) in 1,3-dioxolane (DOL)/1,2-dimethoxyethane (DME) (1:1 by volume) containing 0.1 M $LiNO_3$ as additive.

To evaluate the electrochemical performance of the Li-S cells, an automatic battery test system (Land®, China) was used at room temperature. Electrochemical impedance spectroscopy (EIS) and cyclic voltammetry (CV) measurements were performed on a Biologic VMP 3 electrochemical workstation. Standard components of a CR2032 coin-cell Li-S battery are shown in Figure 3.3 in their stacking sequence.

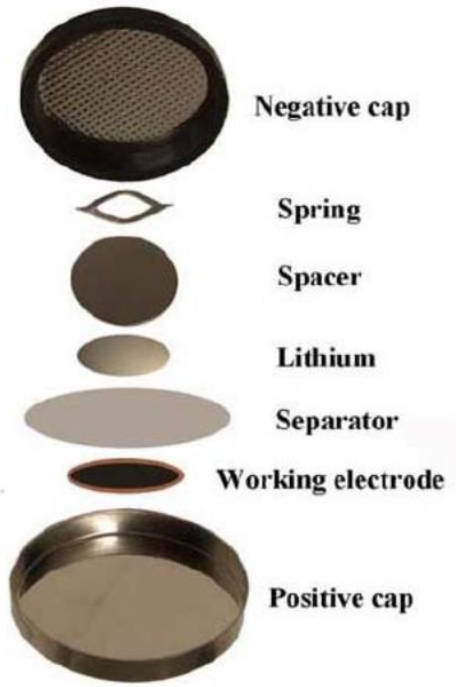

Figure 3.3. Stacking sequence of components of a CR2032 coin cell.[181]

3.5 Chemical characterization

3.5.1 Cyclic voltammetry

Cyclic voltammetry (CV) is a widely used technique for investigating the redox reactions of electrode materials. The CV is a function of current value vs. potential. In a CV measurement, the electrode potential is scanned from a starting voltage to a selected voltage at a constant scan rate, and the response current is recorded. According to the CV curve, we can study the reversibility and reaction mechanism of the electrode material in the electrochemical reactions, analyze the electrochemical activity of electrode materials prepared under different conditions, and test the redox potential of the material. In this work, the CV measurements were carried out on a Biologic VMP-3 electrochemical work station.

3.5.2 Galvanostatic charge-discharge

In constant current charge and discharge testing, the battery is charged and discharged at different current densities according to an artificially set program. The electrochemical performance, such as the cycling performance, rate performance, and coulombic efficiency, is characterized by the charge-discharge capacity of the electrode material. The charge-discharge current of a lithium-sulfur battery is usually expressed by a factor C, where 1 C refers to the amount of current required for the battery to discharge its rated capacity within 1 h. In this paper, 1 C = 1675 mA g^{-1} for sulfur cathode, and 1 C = 1166 mA g^{-1} for Li_2S cathode. An automatic battery test system (Land®, China) was used to test the cycling performance and rate capability of cells at room temperature.

3.5.3 Electrochemical impedance spectroscopy

Electrochemical Impedance Spectroscopy (EIS) was applied to test the internal resistance of the coin cells, which includes the electrolyte resistance, the charge transfer resistance, and the interfacial resistance. In the impedance spectrum, the high-frequency semicircle is related to the charge transfer resistance and the double layer capacitance; the low-frequency linear tail reflects the solid-state diffusion of lithium ions into the electrode materials. In this thesis, EIS data were collected on a Biologic VMP-3 electrochemical workstation in UOW.

CHAPTER 4 FREE-STANDING SULFUR-POLYPYRROLE CATHODE IN CONJUNCTION WITH POLYPYRROLE-COATED SEPARATOR FOR FLEXIBLE LI-S BATTERIES

4.1 Introduction

Flexible electronic devices, such as roll-up displays, and implantable and wearable devices, have drawn much attention to promising soft energy storage systems. In order to power these kinds of devices, flexible batteries with both mechanically robust flexibility and high energy density are required.[182, 183] Currently, lithium ion batteries (LIBs) have dominated the portable device industry for decades due to their high energy density, high working voltage, and long lifetime.[184, 185] Due to the restricted volume and weight in modern flexible electronics, however, even state-of-art LIBs based on intercalation chemistry are limited by insufficient capacity.[186-188] Therefore, exploring new cathode materials with high specific capacity is urgently needed for flexible batteries.

Sulfur, which can react with Li^+ through a two-electron transfer electrochemistry and exhibits high specific capacity (1675 mA h g^{-1}) and high energy density (2600 Wh kg^{-1}), is regarded as a promising cathode material for flexible batteries. Great efforts have been made to date on exploring flexible sulfur cathodes to realize the application of sulfur in flexible devices. Among them, Cheng's group[43] infiltrated sulfur into flexible graphene foam, prepared using Ni foam as template, to produce a cathode for Li-S batteries, which showed long-term stability. Peng et al. developed a flexible hybrid cathode containing CMK-3 ordered mesoporous carbon, sulfur, and carbon nanotubes (CMK-3@S/CNT) with an aligned and laminated structure to improve the conductivity of the electrode and suppress the shuttle effect.[189] Niu's group[190] designed two kinds of soft-packaged and

cable-type flexible Li-S batteries based on a free-standing paper-like reduced graphene oxide (rGO)-S film with high flexibility, which showed stable electrochemical performance in the bent state. Although great developments have been made in flexible sulfur cathodes, the flexible matrixes that are used are always nonpolar carbonaceous materials, such as rGO or CNT, which have low binding energy with polar Li_xS ($0 < x \leq 2$).[74] Compared with carbonaceous materials, polypyrrole (PPy), as a conducting polymer, has many advantages as a cathode matrix for Li-S batteries. First, PPy has strong interactions with intermediate polysulfides due to its unique chain structure and the lone pair electrons of the nitrogen atoms in PPy.[76, 84] Moreover, the redox potential of PPy (2.5 V vs. Li/Li^+) is located in the range of potential windows that are suitable for the Li-S battery.[191] Therefore PPy not only acts as an electrically conducting agent, but also contributes capacity to the Li-S batteries.[22, 149] Keeping these considerations in mind, we designed a free-standing sulfur-polypyrrole cathode (PPy/S@PPy) by loading sulfur coated polypyrrole (S@PPy) composite on a flexible PPy film. The as-prepared PPy film possesses a rough surface, which can enhance the adhesion of active material and further trap the dissolved polysulfides. Furthermore, the flexible PPy film shows excellent mechanical elasticity,[192] which can accommodate the volume expansion and prevent the peeling-off and cracking of active materials, which usually occurs in traditional electrodes. Due to the synergistic effect provided by the PPy film, the designed free-standing sulfur-polypyrrole cathode was found to be more suitable for flexible Li-S batteries than the traditional electrode with Al foil as substrate.

Recently, it was demonstrated that the cell configuration also plays a vital role in achieving higher capacity and more stable cyclability.[193, 194] Fang et al. provided an overview of promising approaches for realizing Li-S batteries that are suitable for commercialization, in which the electrode architecture, cell engineering, and design

parameters are comprehensively discussed for improving the electrochemical performance of the Li-S battery.[195] Among these promising methods, A. Manthiram and co-workers[120] inserted a layer of free-standing microporous carbon paper between the cathode and the separator to address the shuttle effect, and they found that the interlayer can effectively decrease the internal resistance and adsorb soluble polysulfides. Inspired by this work, we present a bifunctional separator that is fabricated by directly coating polypyrrole nanofibers on a commercial separator. Compared with the carbonaceous interlayers normally used in Li-S batteries, the PPy layer coated on the separator acts as a fishing net to capture dissolved polysulfides to mitigate the shuttle effect,[84] which can enhance the cycling stability of Li-S batteries. In addition, the PPy layer coated on the separator is much lighter (0.3 mg cm^{-2}) than many free-standing interlayers fabricated by other groups,[126, 130, 196] which will improve the gravimetric capacity of the whole cell. As a result, the PPy-coated separator will provide Li-S batteries with high capacity and enhanced cycling stability.

In this study, based on the flexibility of the designed free-standing sulfur cathode and the PPy coated separator, a soft-packaged flexible Li-S battery based on them was assembled. Due to the inherent advantages of PPy mentioned above, the newly designed flexible Li-S battery is expected to exhibit stable cycling life and have great practical applications.

4.2 Experimental section

Synthesis of PPy film: The PPy film was synthesised by an electrodeposition method. The electrodeposition was carried out in a solution containing 0.2 M pyrrole and 0.05 M sodium *p*-toluene sulphonate (p-TSNa). A stainless steel plate was used as the working electrode, a reticulated vitreous carbon tube as the counter electrode, and Ag/AgCl as the reference electrode. The process was carried out using an automatic battery tester system

(Land®, China) with a constant current density of 1 mA cm^{-2}. After electrodeposition, the PPy free-standing film was easily peeled off from the stainless steel plate and washed with distilled water and ethanol, which was followed by room-temperature drying.

Synthesis of PPy nanofiber: PPy nanofiber was synthesized via an oxidative chemical polymerization method. The pyrrole was distilled before use. In a typical process, 0.72 g hexadecyl trimethyl ammonium bromide (CTAB) was dissolved in 200 mL of 1 M HCl aqueous solution. Then, 0.25 g sodium *p*-toluene sulfonate and 0.33 g distilled pyrrole were added into the above solution successively, and the solution was precooled in an ice bath (0-5 °C) maintained for 0.5 h under constant magnetic stirring. Meanwhile, 1.13 g ammonium persulfate was dissolved in 20 ml distilled water, which was then dropped into the pyrrole-containing solution. The whole solution was reacted for 12 h in an ice bath (0-5 °C) under magnetic stirring. After that, the black product was collected by vacuum filtration and washed with 1 M HCl and distilled water several times, followed by drying at 60 °C for 12 h in an oven. Finally, the obtained black powder was denoted as PPy nanofiber.

Synthesis of S@PPy composite: The composite was prepared as follow: 32 mg PPy nanofiber was added into a 50 mL aqueous solution containing 470 μL Triton® X-100 surfactant, followed by sonication for 3 h to form a stable suspension. A uniform coating of sulfur on the surfaces of the PPy nanofibers was realized by a simple chemical deposition method. Briefly, 0.5 g $Na_2S_2O_3$ was first dissolved in 150 ml distilled water, and then the $Na_2S_2O_3$ solution was added into the as-prepared PPy suspension. The mixed solution was stirred at room temperature for 3 h. After that, 15 ml HCl (0.5 M) was slowly added at a rate of 0.1 mL min^{-1}. After the reaction, the as-synthesized S@PPy composite was collected by vacuum filtration and washed with distilled water several times to remove residue salts and impurities. Finally, the obtained sample was dried at 50 °C

overnight. The sulfur particles were synthesized using the same method as preparing S@PPy composites, without using Triton® X-100 surfactant and PPy nanofibers.

Fabrication of CNT free-standing film: The fabrication of the single-walled (SW) CNT free-standing film was exactly the same as in our previous work.[197] 15 mg of SWCNT with 500 ml de-ionized water were poured into a beaker, and 500 mg of Triton-X100 surfactant was added. Then, the solution was probe sonicated for 1 h with a 2 s pause time, followed by vacuum filtration and washing with de-ionized water and ethanol. The polytetrafluoroethylene (PTFE) filter paper with the SWCNT layer was dried under vacuum overnight at 60 °C, and finally, the SWCNT film was easily peeled off from the filter paper.

Material Characterizations: For physical and morphological characterization of the composite, X-ray diffraction patterns (XRD, GBC MMA 017) were collected over a 2θ range of 10° - 80° with a scan rate of 2° min^{-1}. Raman spectra were collected on a JOBIN YVON HR800 Confocal Raman System with 632.8 nm diode laser excitation on a 300 lines mm^{-1} grating at room temperature. The Fourier transform infrared (FTIR) spectrographs were collected using a Nicolet Avatar 360 FTIR Fourier transform infrared spectrometer. X-ray photoelectron spectroscopy (XPS) was conducted on a Vacuum Generator (VG) Scientific ESCALAB 2201XL instrument using Al Kα X-ray radiation and fixed analyser transmission mode. Thermogravimetric analysis (TGA) was performed in air using a SETARAM instrument to estimate the amount of sulfur in the sample. The morphologies of the samples and corresponding element mapping images were examined by field emission scanning electron microscopy (JEOL: FESEM-7500).

Electrochemical Measurements: The coin cells and soft-packaged batteries were all assembled in an Ar-filled glove box. Lithium metal foil was used as the anode. The PPy

film was cut into disks with a diameter of 12 mm to be used as current collectors. The S@PPy composite slurry was made by mixing 80 wt% S@PPy with 10 wt% carbon black and 10 wt% poly(vinylidene fluoride) (PVDF) binder in N-methyl-2-pyrrolidinone (NMP) solvent. The slurry was spread on the PPy film with a doctor blade. The PPy coated separator was prepared using the same method. The S@PPy electrode and PPy-separator were dried in a vacuum oven at 60 °C overnight. The mass loading of the sulfur cathode was about 1.4 mg cm^{-2}. The electrolyte was 1 M lithium bis(trifluoromethanesulfonyl)imide (LiTFSI) in 1,3-dioxolane (DOL)/1,2-dimethoxyethane (DME) (1:1 by volume) containing 0.1 M $LiNO_3$ as additive. The amount of electrolyte used in coin cell is 15 uL g^{-1} based on the sulfur amount in electrodes. The soft-packaged Li-S batteries were assembled as follows: the PPy-separator and electrolyte were sandwiched between the PPy/S@PPy electrode and the Li foil, the assembly was then sealed in an Al/polymer soft package, and the same electrolyte as used in the coin cells was injected. The size of the Al/polymer used in the soft-packaged Li-S batteries is 5 cm × 5 cm. The size of both the sulfur cathode and the lithium foil used in the soft-packaged Li-S batteries is 2 cm × 2 cm. To verify the practical application of the obtained flexible Li-S battery in flexible devices, it was bent by hand to an angle of about 140˚ 10 times, and then was used to power the device in the bent state. For electrochemical performance evaluation of the Li-S cell, an automatic battery test system (Land®, China) was used at room temperature. Electrochemical impedance spectroscopy (EIS) and cyclic voltammetry (CV) measurements were performed on a Biologic VMP 3 electrochemical workstation over a frequency range of 10 mHz to 100 kHz, and the scan rate was 0.1 mV s^{-1} within a 1.7 V to 2.8 V voltage window. The coin cell charge-discharge testing was carried out with a LAND battery test system at 0.2 C (1 C = 1675 mA g^{-1}) within the voltage range of 1.7-2.8 V. The soft-packaged Li-S battery

was tested at 0.1 C. For calculate the polarization, we choose a same specific capacity (for example 500 mA h g^{-1}) for every electrode at the same current density. The voltage was written down when the capacity was reached 500 mA h g^{-1} in the charge and discharge process, respectively. Then use the charge voltage minus the discharge voltage obtaining the polarization values.

4.3 Results and Discussion

4.3.1 Structure and morphology

The crystalline structures of the synthesized sulfur, PPy nanofiber, and S@PPy composite were investigated by X-ray diffraction (XRD). As shown in Figure 4.1a, all the diffraction peaks of the S@PPy composite match very well with the diffraction lines of sulfur (JCPDS No: 08-0427), indicating the formation of well-defined crystalline sulfur during the chemical synthesis procedure. PPy only has a broad and weak diffraction peak between 20-30˚, however, suggesting an amorphous structure. Raman spectroscopy measurements were also used to confirm the formation of the as-prepared S@PPy composite. Figure 4.1b shows the Raman spectra of bare S, PPy nanofiber, and S@PPy composite in the range of 100 to 2000 cm^{-1}. The Raman spectrum of S displays three main peaks below 500 cm^{-1}, which can be assigned to the S-S bond. These basic features of crystal structure can be understood in terms of the assignments of Scott, McCullough, and Kruse for the Raman-active $2A_1 + 3E_2 + 2E_3$ species appropriate to a molecular unit S_8 of D4d symmetry. The peaks centered at 151 cm^{-1} are assigned to the E_2 symmetry species; those at 218 and 474 cm^{-1} are assigned to the A_1 species; and those small peaks located at 248 and 437 cm^{-1} are assigned to the E_3 species. In the case of PPy, the Raman scattering peak located at 1599 cm^{-1} is ascribed to the C=C stretching vibration. The scattering peaks at 1320 cm^{-1} and 1396 cm^{-1} are assigned to the

ring-stretching mode of PPy. The peak at 1260 cm^{-1} is assigned to the N-H in-plane bending vibration. The peaks at 1043 and 930 cm^{-1} are assigned to the C-H out-of-plane bending vibration.[198] The Raman spectrum of S@PPy composite shows not only the three characteristic peaks of sulfur below 500 cm^{-1}, but also the typical peaks of PPy between 800 and 1700 cm^{-1}, which confirms that the S@PPy composite contains both elemental sulfur and PPy. X-ray photoelectron spectroscopy (XPS) measurements were performed on the as-prepared PPy nanofiber and S@PPy composite to obtain more detailed information on the surface chemical composition and the chemical states of the elements. The XPS spectrum of PPy indicates the presence of C 1s, N 1s, and O 1s signals at 285, 399.7, and 532 eV, respectively, as shown in Figure 4.1c.[199] In comparison, the spectrum of S@PPy composite shows two additional S 2p and S 2s signals, confirming the successful loading of sulfur on PPy nanofibers. The high-resolution spectrum of the S 2p region (Figure 4.1d) is deconvoluted into three peaks. The binding energy at 163.6 eV corresponds to S $2p_{3/2}$, which is slightly lower than for elemental sulfur (164 eV), revealing the possible presence of C-S species,[200, 201] while the binding energy at 164.9 eV corresponds to S $2p_{1/2}$. The peak at 168.4 eV can be ascribed to the sulfate species formed by the oxidation of sulfur in air and the residual ammonium persulfate.[85] The binding energy of the N 1s peak is centred at 399.7 eV, which is attributed to pyridinic N from PPy nanofiber (Figure 4.1e).[202] FTIR experiments (Figure 4.1f) were also conducted to confirm the presence of PPy. Compared with the FTIR spectra of PPy and S, the spectrum of S@PPy composite exhibited the clear presence of the vibrational peaks corresponding to PPy, indicating the presence of PPy in the composite.

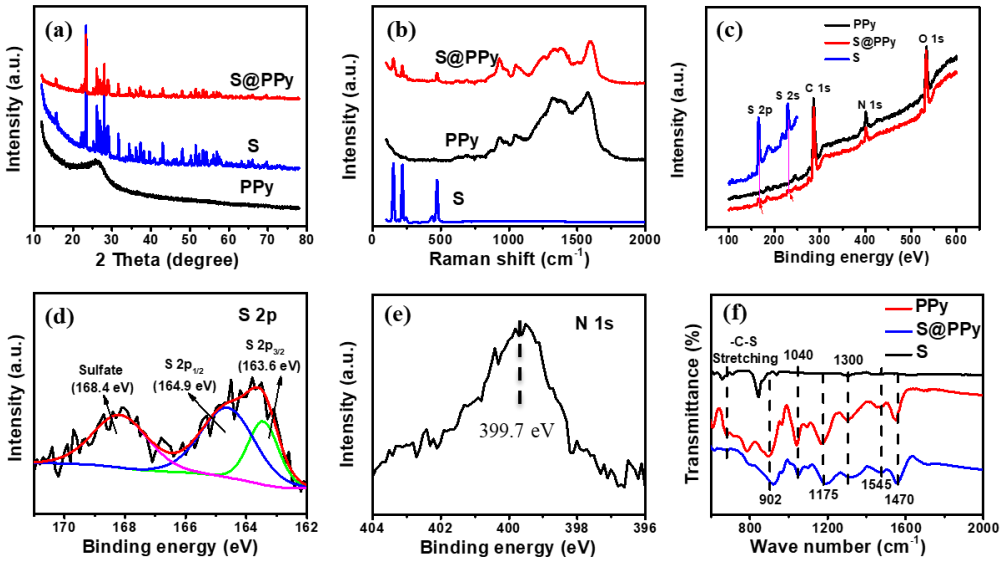

Figure 4.1. **(**a) XRD patterns of synthesized sulfur, PPy nanofiber, and S@PPy composite; (b) Raman spectra of bare S, prepared PPy nanofiber and S@PPy composite; (c) XPS spectra of obtained PPy nanofibers and S@PPy composite; (d) High resolution S 2p XPS spectrum of S@PPy composite; (e) High resolution of N 1s XPS spectrum of PPy nanofibers; (f) FTIR spectra of bare S, PPy nanofiber and S@PPy composites.

Thermogravimetric analysis (TGA) was carried out in air to determine the content of sulfur in the S@PPy composite. As shown in Figure 4.2, the TGA curves of PPy consist of two weight loss stage, the first one is from 40 ℃ to 130 ℃, which can be ascribe to the evaporation of residual moisture; the second one is the oxidation of PPy in air (250 ˚C - 580 ˚C). As for the S@PPy composites, the TGA curve consist of three weight loss stages: the first one is same with that of PPy nanofibers, which is about 4.2%; the second weight loss stage from 130˚C to 250 ˚C was assigned to the sublimation of sulfur, which is 52.6%; and the third stage was also same with that of PPy nanofiber. Due to the TGA curves of PPy and S@PPy composites in the first stage was exactly coincide, indicating no sulfur evaporation in this stage. And the sulfur amount can be decided by the second stage of weight loss. Thus, the content of sulfur in the S@PPy

composites was found to be 52.6%. From the TGA profile, it is clearly seen that the release temperature of sulfur in S@PPy is slightly lower than that of simple sublimed sulfur. This phenomenon can be ascribed to the uniform dispersion of nanosized sulfur in S@PPy compared to the bulk-type material in sublimed sulfur.[203] In addition, the incorporation of PPy fibers will also slightly accelerate the evaporation of sulfur due to the enhanced heat transfer rate.[204]

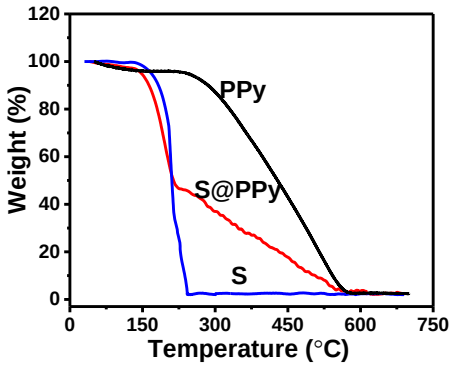

Figure 4.2. TGA curves of synthesized sulfur, PPy nanofiber, and S@PPy composite in air.

The morphology of the as-prepared PPy nanofiber and S@PPy composite were investigated by scanning electron microscopy (SEM). As shown in Figure 4.3a, the surfaces of the pure PPy nanofibers with a diameter about 50-70 nm are relatively rough, which can increase the surface area and makes the deposition of sulfur on them feasible. After the sulfur coating, the S@PPy composite keeps the nanofiber morphology of PPy with a larger diameter, and the surface becomes relatively smooth, indicating the successful loading of sulfur layer on the PPy nanofiber (Figure 4.3b). The corresponding elemental maps of carbon, nitrogen, and sulfur in Figure 4.3d-e further confirm the homogeneous distribution of elements in the S@PPy composite.

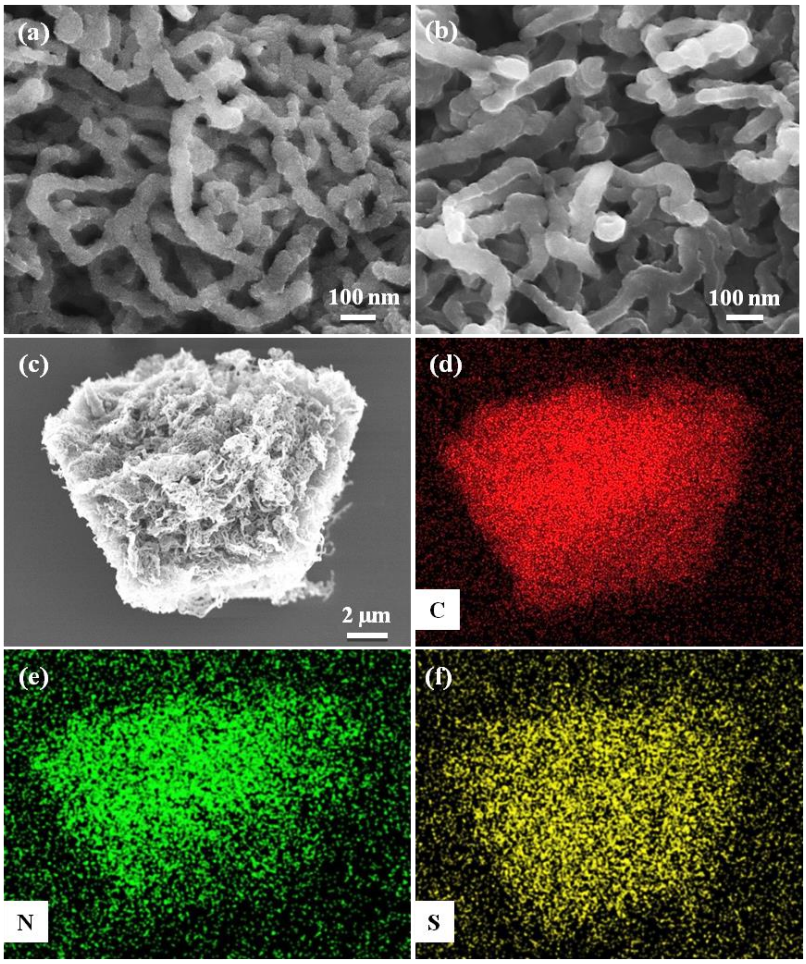

Figure 4.3. SEM images of (a) PPy nanofiber and (b) S@PPy composite; (c) Low-resolution of SEM image and corresponding elemental mapping showing the uniform distribution of (d) C, (e) N, and (f) S elements in S@PPy composite.

A typical photograph of the as-prepared PPy film is shown in Figure 4.4a, which shows excellent flexibility. The free-standing PPy flim can be folded into one fourth of its original size, and could returned to its original appearance without any cracks, while Al foil cannot recover its original shape. Due to the elastic properties of PPy film, it could release mechanical stresses and prevent the peeling-off and cracking of the active material during cycling, which is necessary for a flexible Li-S battery. As shown in Figure 4.4b, the PPy film with a thickness of about 10 µm shows a rough surface consisting of many nodules, which provides a larger contact area and stronger adhesion

with the active material compared with the smooth Al foil. The adhesion of the active materials to the PPy film and Al foil are shown by cross-sectional SEM images of the electrodes (Figure 4.4c-d). The compact and homogenous S@PPy active material tightly adheres to the PPy film (Figure 4.4c), while there is a gap between the S@PPy nanofiber material and the Al foil current collector because of the weak adhesion between the smooth Al foil and the active materials (Figure 4.4d), which will dramatically increase the internal impedance and lead to sluggish redox reactions. In addition, the PPy/S@PPy electrode could keep its integrity, and there is no cracking or exfoliation of the active materials after bending, which can ascribed to the mechanical elasticity of the PPy film (Figure 4.4e), while the Al/S@PPy electrode forms cracks and the electrical connectivity is broken after bending (Figure 4.4f). On the other hand, the weight of the PPy film is only one third that of the Al foil (Table 4.1), which will increase the gravimetric capacity and energy density of the whole cell. As such, the free-standing PPy/S@PPy electrode is more suitable as a flexible Li-S cathode than the Al/S@PPy electrode.

Table 4.1. Weight comparison of different substrates and interlayers

	Al foil	**PPy film**	**CNT interlayer**	**PPy fiber coated on separator**
Weight (mg/cm^2)	2.39	0.77	1.03	0.3

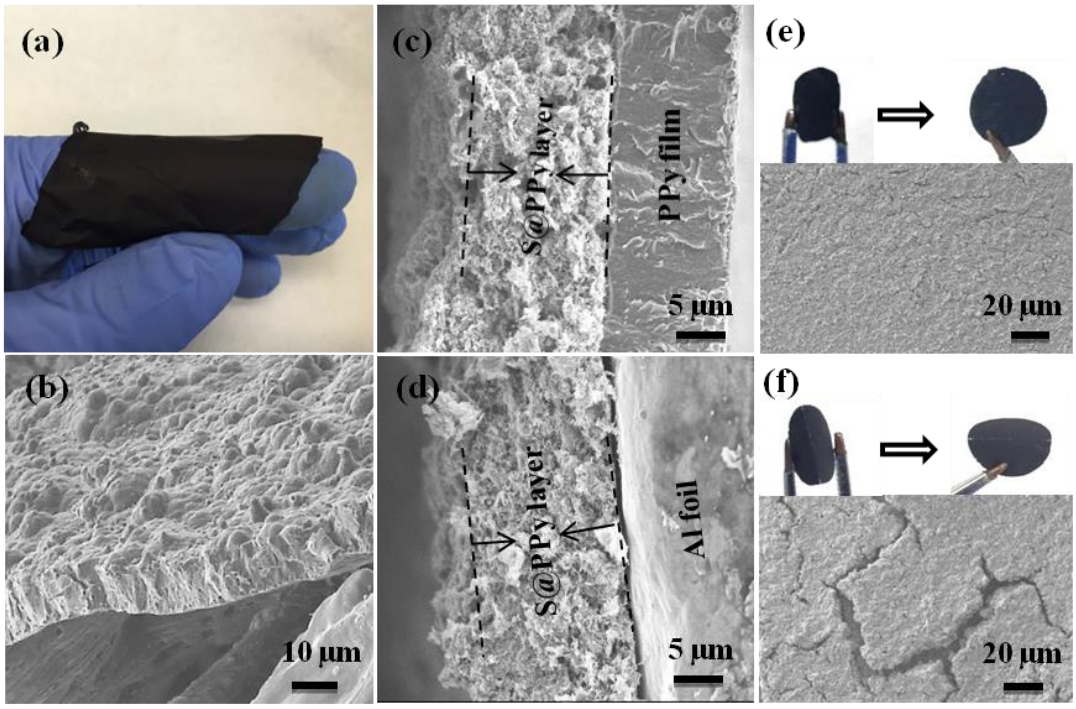

Figure 4.4. (a) Digital photograph and (b) SEM image of prepared PPy film; SEM cross-sectional images of (c) PPy/S@PPy and (d) Al/S@PPy electrodes; (e) Ditital photos of PPy/S@PPy electrode under and after bending, and SEM image of PPy/S@PPy electrode after bending; (f) Ditital photos of Al/S@PPy electrode under and after bending, and SEM image of Al/S@PPy electrode after bending.

4.3.2 Effect of PPy film on electrochemical performance

To verify the effects of the PPy substrate on the electrochemical performance, a series of electrochemical measurements were carried out to compare it with conventional Al foil substrate. The same amount of S@PPy nanofiber was coated on Al foil and PPy film to make cathodes for Li-S batteries (denoted as Al/S@PPy and PPy/S@PPy, respectively). Cyclic voltammetry (CV) measurements were conducted on the Al/S@PPy and PPy/S@PPy electrodes over the voltage range from 1.7 V - 2.8 V at a scanning rate of 0.1 mV s^{-1} (Figure 4.5a and b). Both electrodes show two typical cathodic peaks and one broad anodic peak. The first cathodic peak located at about 2.3 V represents the reduction

of sulfur to soluble long-chain polysulfides (Li_2S_n, $2 < n \leq 8$), and the second cathodic peak at ~2.0 V is due to the further reduction of soluble polysufides to lithium sulfides (Li_2S_2/Li_2S).[34] At around 2.5 V, the anodic peak reveals the conversion from lithium sulfides to lithium polysulfides, and finally to sulfur.[13, 32] The CV peaks for the Al/S@PPy electrode (Figure 4.5b) show a lower reduction potential and higher oxidation potential than those for PPy/S@PPy electrode, indicating higher voltage hysteresis and sluggish kinetics.[205]

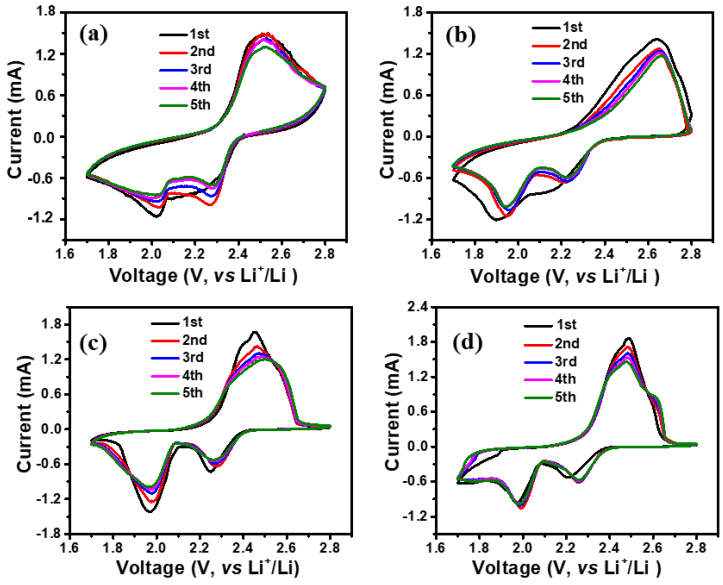

Figure 4.5. CV curves of Li-S batteries with (a) Al/S@PPy, (b) PPy/S@PPy, (c) PPy/S@PPy+CNT interlayer and (d) PPy/S@PPy+PPy-separator structure over the voltage range from 1.7 V - 2.8 V at a scanning rate of 0.1 mV s^{-1}.

Electrochemical impedance spectroscopy (EIS) measurements were used to characterize the internal resistance and charge-transfer process. The Nyquist plots of the PPy/S@PPy and Al/S@PPy electrodes before cycling are shown in Figure 4.6a, which are both composed of a depressed semicircle from the high frequency region to the mid-frequency region and an inclined line in the low frequency region, which are ascribed to the

charge-transfer resistance (R_{ct}) and the mass-transfer process,[206] respectively. The Nyquist plots were analyzed and fitted by an equivalent circuit model (inset in Figure 4.6a). In the equivalent circuit model, R_s, R_{ct}, Z_w, and C_{dl} represents the impedance of the electrolyte, the charge transfer resistance, the Warburg impedance, and the capacitance of the electrical double layer, respectively.[207] According to the fitting results (Table 4.2), the charge-transfer resistance of the free-standing PPy/S@PPy electrode (425.6Ω) is slightly lower than that of the Al/S@PPy electrode (556.8 Ω). The conductivity of the pure PPy film is 19.23 S cm^{-1}, however, which is much lower than that of Al foil (3.7×10^5 S cm^{-1}). The lower charge-transfer resistance would be ascribed to the rough surface of the PPy film and tight adhesion to the S@PPy composite.

Table 4.2 R_{ct} values measured for different electrode structures before cycling

Electrode structure	**PPy/S@PPy+ PPy-separator**	**PPy/S@PPy+ CNT interlayer**	**PPy/S@PPy**	**Al/S@PPy**
R_{ct} (Ω)	58.75	90.5	425.6	556.8

The first charge and discharge voltage profiles of the Li-S batteries with PPy/S@PPy and Al/S@PPy cathodes within the potential window of 1.7-2.8 V *vs.* Li^+/Li were collected, as shown in Figure 4.6b. The discharge curves show two plateaus, representing two reduction processes, while the charge curves have one plateau, which matches well with the CV curves. It should be noted that the PPy/S@PPy cathode shows lower polarization (239 mV) than the Al/S@PPy cathode (294 mV), which is ascribed to the kinetically efficient redox reaction process with a small barrier for the PPy/S@PPy cathode.[208]

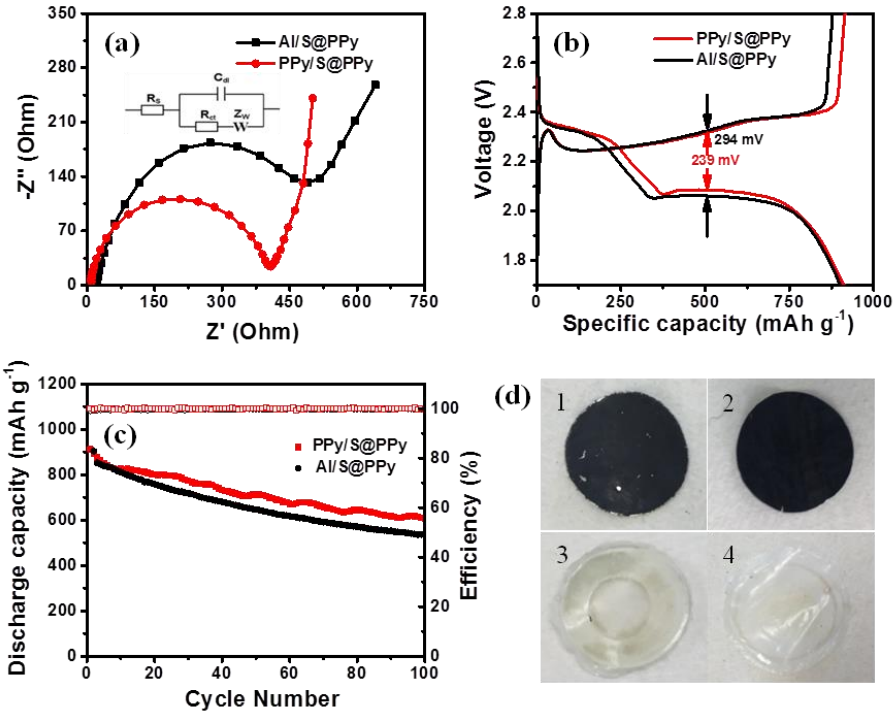

Figure 4.6. (a) Nyquist plots of the PPy/S@PPy and Al/S@PPy electrodes before cycling (inset: equivalent circuit); (b) Galvanostatic charge-discharge profiles of PPy/S@PPy and Al/S@PPy electrodes; (c) Cycling performance of Li-S batteries with PPy/S@PPy and Al/S@PPy cathodes at 0.2 C for 100 cycles; (d) Photograph of cycled (1) Al/S@PPy electrode and (2) PPy/S@PPy electrode; Photograph of separator disassembled from Li-S batteries with (3) Al/S@PPy electrode and (4) PPy/S@PPy electrode.

To further clarify the merits of free-standing PPy film as current collector, the cycling performance of Li-S batteries with PPy film current collector was investigated for comparison with cells using conventional Al foil at a current density of 0.2 C, as shown in Figure 4.6c. The same amount of S@PPy nanofiber active materials were coated on PPy film and Al foil, respectively, to make electrodes for Li-S batteries (denoted as PPy/S@PPy and Al/S@PPy). The PPy/S@PPy electrodes both showed higher specific capacity than that of Al/S@PPy due to the porous structures of PPy film, which can

store more electrolyte and enhance the contact between the active materials and the current collector, improving the utilization of active materials. The PPy/S@PPy electrode retained a capacity of 653 mA h g^{-1} after 100 cycles with a capacity retention rate of 66.3%. The superior electrochemical performance of the PPy/S@PPy electrode is attributable to the synergistic effect provided by the rough and elastic PPy flim, including the strong adhesion between it and the active materials, trapping dissolved polysulfides and accommodating volume expansion. To further confirm the role of the PPy film in improving electrochemical performance, the cell was disassembled after 100 cycles. Figure 4.6d presents digital photographs of the cycled electrodes and corresponding separators. A small amount of active materials was exfoliated from the Al/S@PPy electrode (Figure 4.6d-1) after cycling. In contrast, the S@PPy nanofibers on PPy flim showed no obvious exfoliation or changes (Figure 4.6d-2), indicating good elasticity of the PPy film, which can accommodate the volume expansion and prevent peeling-off of the active materials during cycling. The separator from the Li-S battery with Al/S@PPy electrode showed a yellowish color (Figure 4.6d-3), indicating the diffusion of polysulfides through the separator, leading to the shuttle effect and low active material utilization. The separator from the Li-S battery with PPy/S@PPy electrode, however, remained relatively clean with no yellowish color (Figure 4.6d-4), which means that the PPy film could act as a further barrier to polysulfide migration. All the results demonstrate that the PPy film could not only maintain the integrity of the electrode during cycling, but also limited the dissolution of polysulfide, which improved the active material utilization and guaranteed a stable cycling performance.

4.3.3 Effect of PPy-coated separator on electrochemical performance

Although the PPy/S@PPy cathode exhibits better cycling performance than CNT/S@PPy and Al/S@PPy electrodes, capacity decay with increasing cycle number still remains a

problem, obstructing its practical application. In order to increase the specific capacity and cycling stability, a PPy nanofiber coated separator (PPy-separator) was used in our following experiments. The separator was prepared by a simple doctor blade method, which is simple and cost-effective compared with preparing free-standing interlayers. Most importantly, the PPy layer on the separator can effectively block the diffusion of polysulfides across the separator to the Li anode, due to its unique chain structure and inter- and/or intra-chain bonding with polysulfides, which will greatly improve the cycling stability.

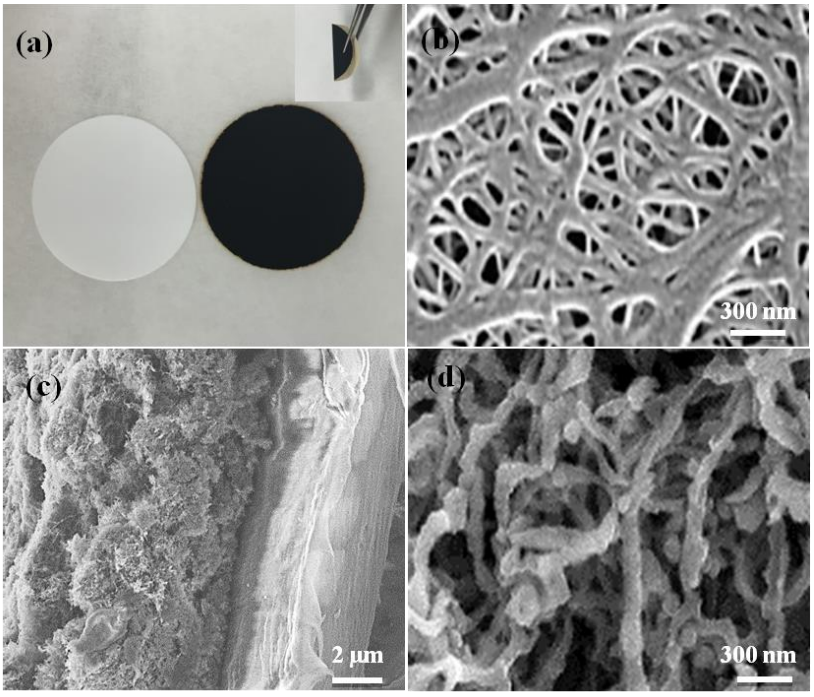

Figure 4.7. (a) Digital photos comparison of commercial separator and PPy nanofiber coated commercial separator, the inset shows the flexibility of PPy nanofiber coated separator; (b) Top-view SEM image of commercial separator; (c) Cross-section SEM image of the PPy nanofiber coated separator; (d) Top-view SEM image of the PPy coated separator.

Photographs of the commercial separator and the as-prepared PPy-separator are shown in Figure 4.7a. A homogeneous PPy layer was coated on the commercial separator, and the PPy-separator exhibits good flexibility (as shown in the inset photograph of Figure 4.7a). Figure 4.7b presents an SEM image of the commercial separator, which displays a highly porous structure with pore size of several hundred nanometres, which the intermediate polysulfides can easily pass through. In contrast, the cross-sectional image of the PPy-separator in Figure 4.7c shows that the PPy layer with a thickness about 5 μm is closely coated on the commercial separator, which not only can improve the conductivity of the cell, but also works as an effective reservoir for dissolved polysulfides to mitigate the shuttle effect. The PPy-separator shows a loose nanofiber structure (Figure 4.7d), which forms a woven-like textile that can act as a fishing net for capturing polysulfides. At the same time, the loose structure ensures that the liquid electrolyte penetrates easily into the whole cell to guarantee rapid redox reactions. The electrochemical properties of a cell with the PPy-separator were investigated, and a cell with a free-standing CNT interlayer was also tested for comparison.

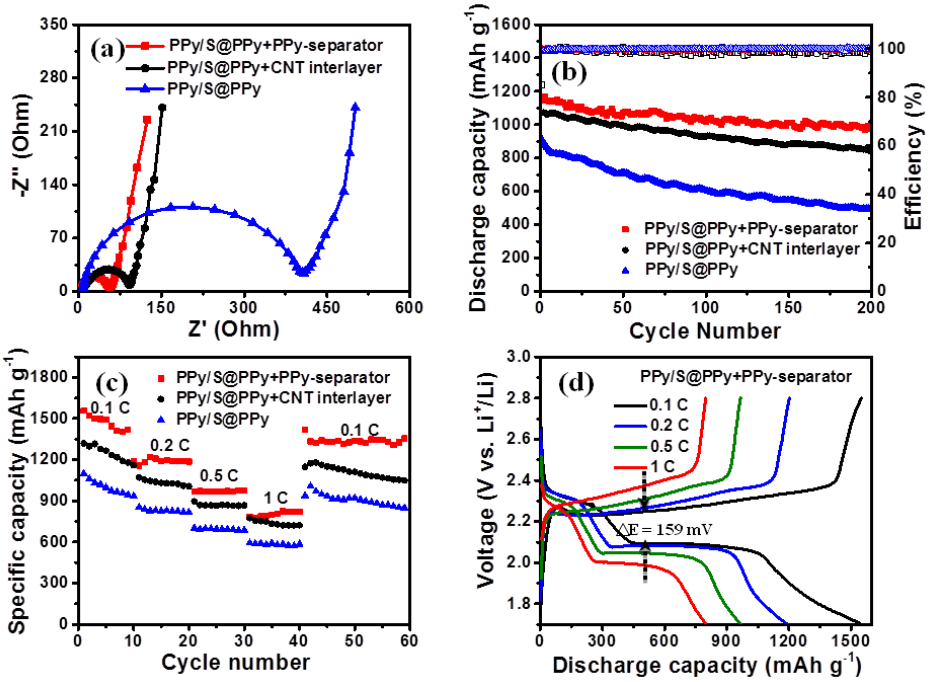

Figure 4.8. (a) Nyquist plots of Li-S batteires with PPy/S@PPy, PPy/S@PPy+PPy-separator, and PPy/S@PPy+ CNT interlayer structure before cycling; (b) Cycling performance (0.2 C) and (c) rate performance of Li-S batteires with PPy/S@PPy, PPy/S@PPy+PPy-separator, and PPy/S@PPy+ CNT interlayer structure; (d) Dischage-charge profiles of Li-S batteires with PPy/S@PPy+PPy-separator structure at different current density.

To analyze the impact of the PPy-separator on the performance of Li-S batteries, impedance analysis was performed on Li-S batteries with commercial separator, PPy-separator, and a CNT interlayer before cycling (Figure 4.8a). Compared with the battery with the commercial separator, the charge transfer resistances of the Li-S batteries with the PPy-separator or CNT interlayer both dramatically decrease (Table 4.2). The conductive interlayer between the cathode and the separator acts as an upper current collector, which can maintain contact with the active material on the nanoscale and allows electrons to flow freely through the cathode, reducing the effective resistance of

the highly insulating sulfur cathode and accelerating the kinetics of the electrochemical reactions. Moreover, the PPy-separator shows a smaller charge transfer resistance than the CNT interlayer, which can be attributed to the tight contact between the PPy layer and the separator. Figure 4.8b and c shows the cycling and rate performance of the Li-S batteries with PPy/S@PPy, PPy/S@PPy+PPy-separator, and the PPy/S@PPy+CNT interlayer structure. Compared with the Li-S batteries with commercial separator, the cycling and rate performances of the Li-S batteries with the PPy-separator and CNT interlayer are better, indicating that the conductive layers between the cathode and the separator can effectively capture polysulfides and improve sulfur utilization. As shown in Figure 4.8b, the initial discharge capacity of the Li-S battery with the PPy/S@PPy+PPy-separator structure is 1236 mA h g^{-1} at 0.2 C, and the battery still retains discharge capacity of 1073 mA h g^{-1} after 200 cycles, with a capacity retention rate of about 86.8%. On the other hand, the initial discharge capacity of the Li-S battery with the PPy/S@PPy+CNT interlayer structure is 1158 mA h g^{-1}, and the capacity after 200 cycles is 907 mA h g^{-1}, which is much lower than that of the PPy/S@PPy+PPy-separator structure. In addition, the Li-S battery with PPy-separator delivers higher discharge capacity than that with the CNT interlayer at all current densities (Figure 4.8c), which indicates that the PPy features stronger adsorption of polysulfides than the CNT interlayer due to its unique chain structure and inter- and/or intra-chain bonding with polysulfides. The CV curves of a battery with PPy/S@PPy+PPy-separator structure show two cathodic peaks and one broad anodic peak (Figure 4.5d), and the peak intensities and positions are almost the same from the second to the fifth cycle, which indicates the good cycling stability of this system. The CV curves of a battery with the PPy/S@PPy+CNT interlayer structure show a slightly lower reduction potential and a slightly higher oxidation potential (Figure 4.5c), and the integral areas are decreased with the increasing

cycle number, which suggests capacity fading during cycling. The galvanostatic discharge profiles of a battery with the PPy/S@PPy+PPy-separator structure at different current densities (from 0.1 C to 1 C) consist of two plateaus (Figure 4.8d), even at a very high current rate. The plateaus are flat and stable with a relatively low polarization of 159 mV at 0.1 C, which suggests a kinetically efficient reaction process with a small barrier. In contrast, the discharge potential decreases, and the charge potential increases for the Li-S batteries with PPy/S@PPy+CNT interlayer, PPy/S@PPy, and Al/S@PPy structures, resulting in higher voltage hysteresis (171, 198, and 274 mV at 0.1 C, respectively) (Figure 4.9). In addition, the weight of the PPy layer coated on the separator is much lighter (0.3 mg cm^{-2}) than that of the CNT interlayer (1.03 mg cm^{-2}) (Table 4.1), which will further improve the gravimetric capacity of the whole cell.

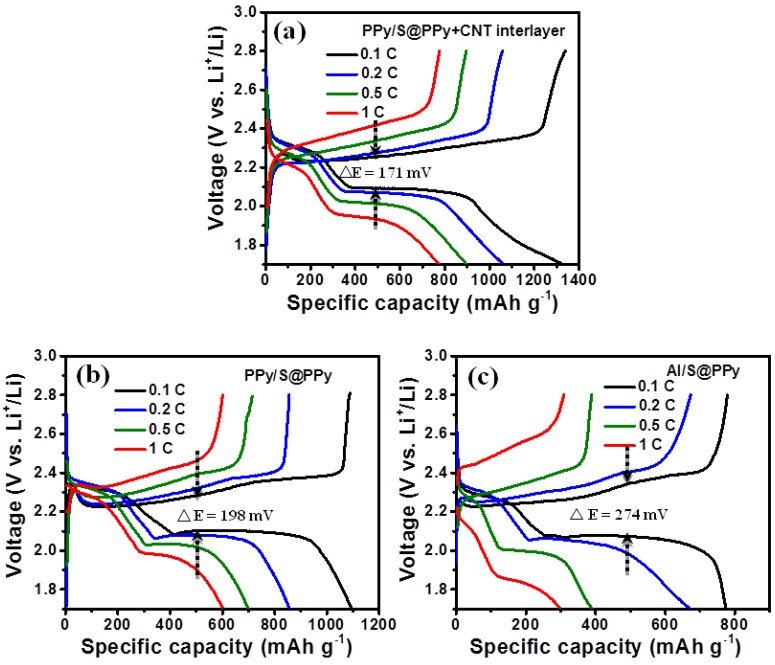

Figure 4.9. Dischage-charge profiles of Li-S batteires with (a) PPy/S@PPy+CNT interlayer, (b) PPy/S@PPy and (c) Al/S@PPy structure at different current density.

To understand how the PPy-coated separator suppresses the polysulfide diffusion, the coin cells were disassembled in a glove box after 50 cycles. A cross-sectional SEM image of the cycled PPy-coated separator and the corresponding element mapping are shown in Figure 4.10a. The PPy layer maintains its original structure and is still firmly adhered to the separator. The mapping image of sulfur indicates that the dissolved polysulfides are mainly trapped within the PPy layer before they pass through the separator because only very weak sulfur signals are detected on the commercial separator. As further evidence, SEM images of the Li anode surface after 50 cycles are shown in Figure 4.10c and d. Compared with the fresh metallic Li (Figure 4.10b), the Li anode from the cell with the PPy/S@PPy cathode and the commercial separator exhibits a severely damaged surface caused by the reaction of lithium with long chain lithium polysulfides (Li_2S_n $2 < n \leq 8$). In contrast, the Li anode from the cell with the PPy/S@PPy electrode and the PPy-separator shows a relatively smooth surface, which indicates that the polysulfides are mainly trapped on the cathode side rather than travelling to the anode side. This phenomenon illustrates the superior ability of the PPy-separator to suppress the shuttle effect and prevent the corrosion of the Li anode during cycling. Table 4.3 compares the electrochemical performance of this Li-S battery with the PPy/S@PPy+PPy-separator structure with some Li-S batteries reported previously using polypyrrole as an adsorption medium for polysulfides.[85, 209-212] The mass loading of active material is comparable in these papers. The specific capacities of the designed Li-S battery at different C-rates are quite remarkable and higher than those observed in previously reported composite electrodes. This is due to the unique PPy film substrate and the PPy coated separator as a polysulfide reservoir.

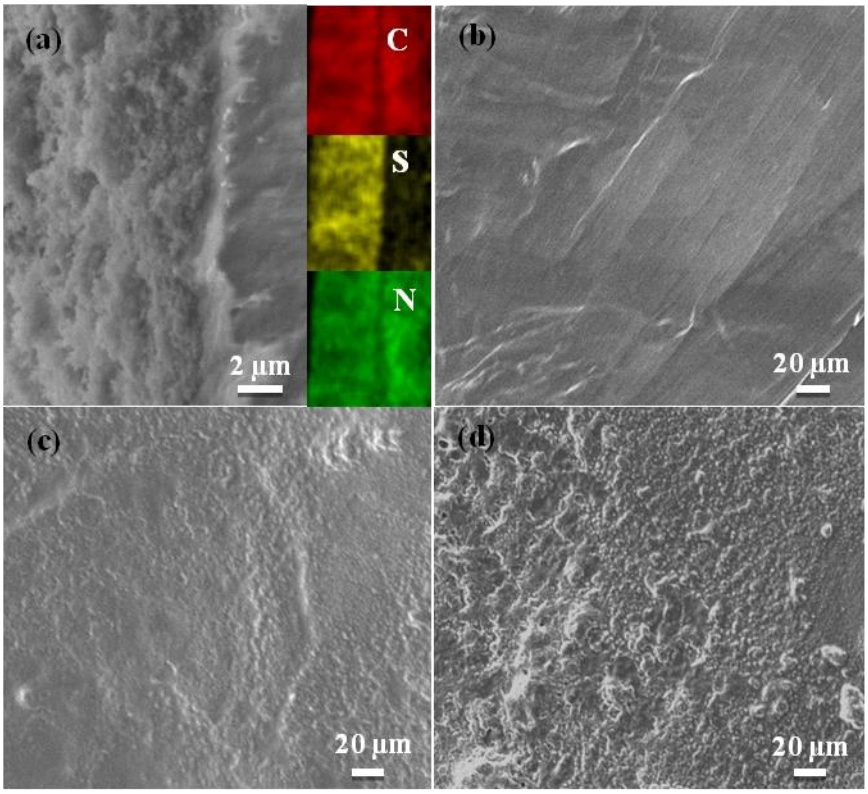

Figure 4.10. (a) SEM image and element mappings for PPy coated separator after 50 cycles; SEM images of (b) pristine lithium and lithium anode from the battery with PPy/S@PPy electrode (c) with and (d) without the PPy-coated separator after 50 cycles.

Figure 4.11a and b clearly illustrates the advantages of the designed structure compared with the traditional electrode structure. First, the flexible and conductive PPy film has a rough surface, which can enhance adhesion of the active materials and trap polysulfides, resulting in low contact resistance and stable cycling performance. Second, PPy is an active material, which can contribute capacity during cycling, as shown in Figure 4.11c and d. Moreover, the PPy film could maintain its integrity even after 100 cycles (Figure 4.11e and f) due to its elastic property, which gives it electrochemical stability during cycling. Finally, the PPy layer coated on commercial separator not only acts as a reservoir for capturing polysulfides for reutilization, inhibiting the shuttle effect, but also acts as an

upper current collector to facilitate electron transfer. As a result, the designed Li-S battery shows excellent cycling and rate performance.

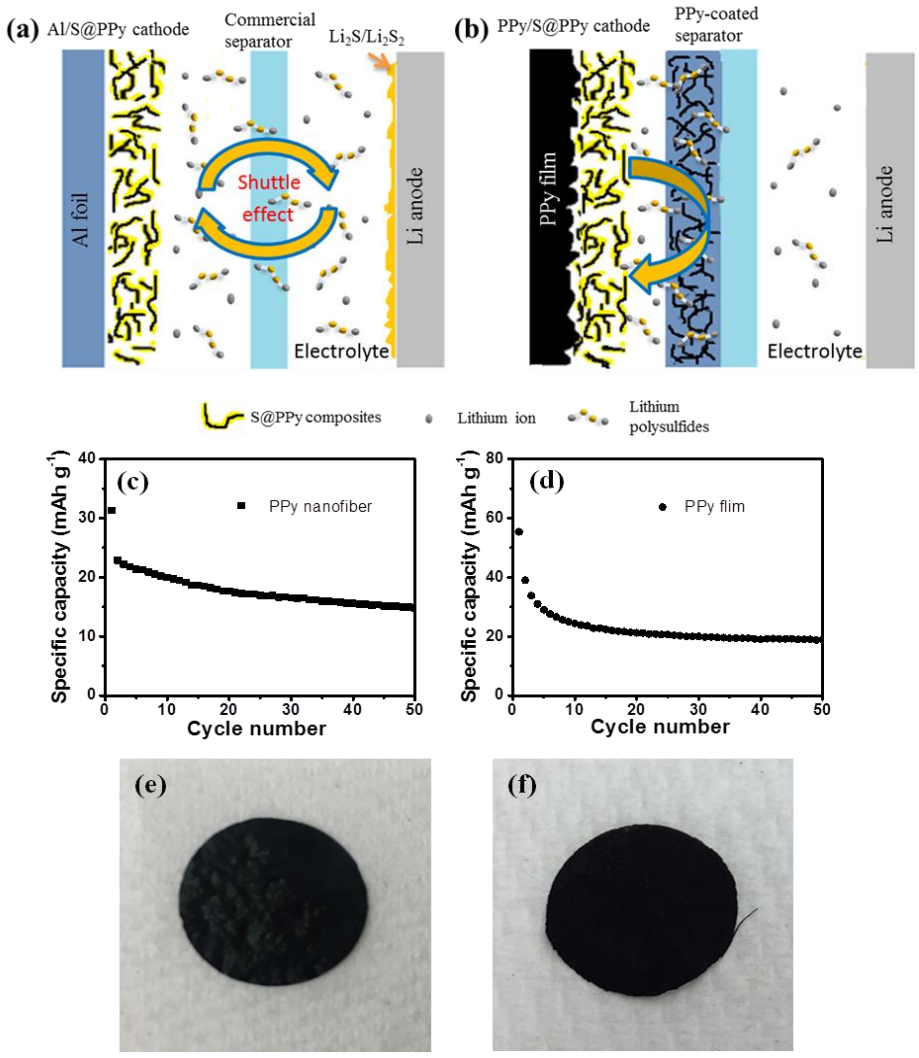

Figure 4.11. Schematic illustration of a Li-S battery with (a) the traditional electrode structure and (b) the uniquely designed electrode structure; Cycling performance of (c) PPy nanofiber electrode and (d) free-standing PPy film; The digital photos of free-standing PPy film (e) before and (f) after 100 cycles.

4.3.4 Electrochemical performance of soft-packaged Li-S batteries

In order to verify the potential application of the cell with the PPy/S@PPy cathode and PPy-separator in flexible Li-S batteries, soft-packaged Li-S batteries consisting of the

free-standing PPy/S@PPy film cathode, the PPy-coated separator, and lithium foil anode were assembled in a glove box. Figure 4.12a shows the initial charge–discharge curves of a soft-packaged battery before and after bending. The charge–discharge curves before and after bending are similar, indicating that the bending operation makes no difference to the redox reactions of sulfur. The cycling performance of the soft-packaged Li-S battery is shown in Figure 4.12b. It delivers an initial discharge capacity of 1064 mA h g^{-1} at 0.1 C. After 20 cycles, the discharge capacity is still maintained at 848 mA h g^{-1} with capacity retention of 79.7%. The decrease of capacity can be ascribed to the relative loose contact between cathode and anode in the soft-packaged cell. The technology used in assembling flexible battery needed to be improved in future study. After that, the flexible battery was bent 10 times, and charged and discharged under the same conditions. It still could retain almost the same capacity compared with that before bending, which indicates that the electrochemical behaviour of the flexible Li-S battery was only slightly influenced by repeated bending. EIS measurements were conducted before and after repeated bending (Figure 4.12c). The results indicated that, after the bending, the conductivity of the cell was slightly lower than that of the unbent cell, which can be ascribed to the loose contact between the Li anode and the PPy/S@PPy cathode during the repeated bending process. SEM images of the free-standing PPy/S@PPy cathode before and after the bending are shown in Figure 4.12d. No cracks were detected in the electrode around the bent area after the bending test. This suggests that the electrode is resistant to repeated bending. To demonstrate the practical application of the designed flexible Li-S battery, the soft-packaged battery was used to light up a “UOW” device containing 24 white light-emitting diodes (LEDs) (Figure 4.12e and f). The LEDs could still be well lit when the soft-packaged Li–S battery was bent to an angle of about 140˚. In short, the designed flexible Li-S battery shows excellent mechanical and

electrochemical properties during a rough bending treatment, which is attributed to the novel free-standing PPy/S@PPy cathode and the PPy-coated separator. First, the rough and elastic PPy film will enhance the adhesion of the active material and relieve the mechanical stress during bending. Second, the PPy-coated separator could efficiently trap dissolved polysulfides to improve the utilization of the active material, leading to superior electrochemical performance. All these results show its great potential for powering flexible electronics. Despite great electrochemical performance was obtained for this flexible Li/S batteries using Li metal as anode materials, there are still some safety potential problems related with Li metal. Using metal-free flexible anode materials instead of Li metal, such as Si, Sn and C.[164] Therefore, it is necessary to explore metal-free anode to fulfill the requirements of practical application in the future study.

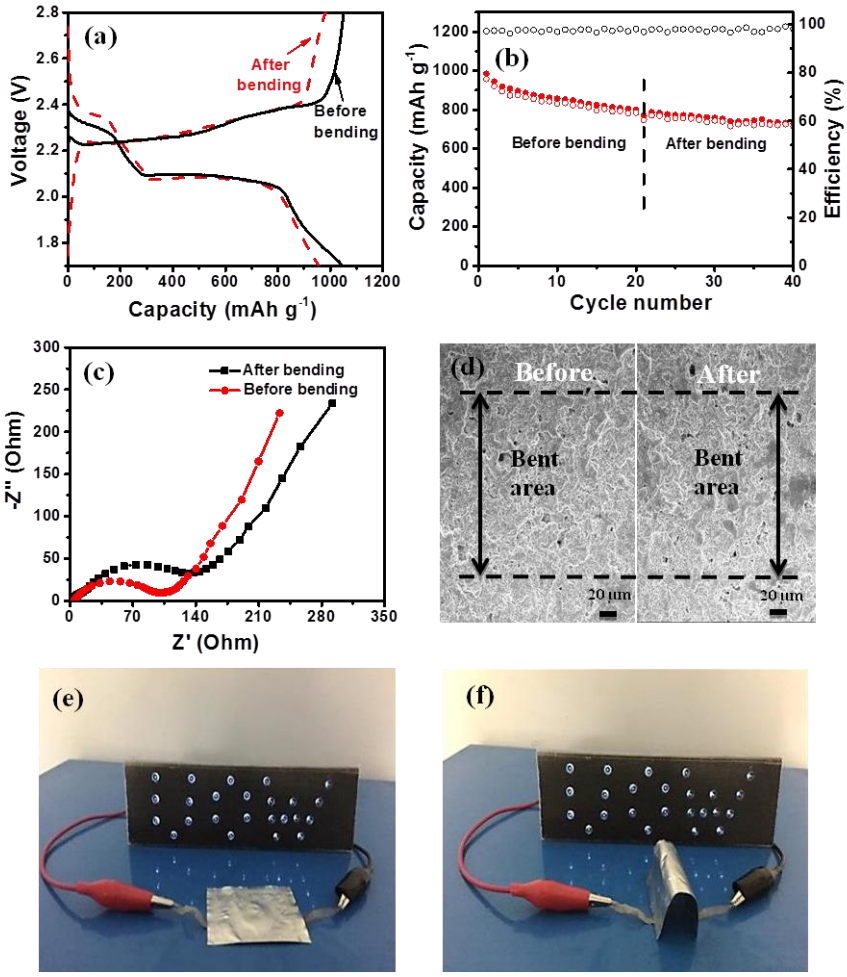

Figure 4.12. (a) Charge/discharge curves of the soft-packaged battery before and after bending; (b) Cycling performance of the soft-packaged battery at 0.1 C; (c) Nyquist plots of the soft-packaged battery before and after bending; (d) FESEM images of electrode before and after repeated-bending tests; The optical images show a white LED logo powered by a Li-S battery with a PPy/S@PPy+PPy-separator structure (e) before and (f) after bending.

Table 4.3. Comparisons of electrochemical performances between this work and the reported polypyrrole-based cathode for Li-S batteries.

Materials description	**S content (wt%)**	**S loading**	**1st discharge capacity**	**Cycle number**	**Capacity after the reported**	**Refs.**

		(mg cm^{-2})	(mAh g^{-1})		cycles (mAh g^{-1})	
PPy/S@PPy +PPy-separator	56.8%	1.5	1144 (0.2 C)	200	994 (0.2 C)	**This work**
S/KB+PPy layer	45%	0.5	823 (0.1 C)	n/a	n/a	[209]
PPy coated S@GCS	64%	0.4-0.6	925 (0.5 C)	100	750 (0.5 C)	[85]
PPy coated AB/S	45%	1.3-1.8	847 (0.5 C)	200	630 (0.5 C)	[210]
PPy coated S spheres	65%	n/a	961 (0.2 C)	50	530 (0.2 C)	[211]
Core-shell PPy@S	80%	2.6	1142 (0.1 C)	100	725 (0.1 C)	[212]
PPy@S@PPy	65.6%	n/a	800 (0.1 C)	50	550 (0.1 C)	[149]
sulfur-PPy composite	70%	4.5	1043 (0.06 C)	30	500 (0.06 C)	[213]
S/C+PPy interlayer	67%	2.5-3	1102 (0.5 C)	300	712 (0.5 C)	[214]

4.4 Conclusions

In summary, a free-standing sulfur-PPy cathode and a PPy nanofiber coated separator were designed for flexible Li-S batteries. The as-prepared PPy film not only has a rough surface, which can enhance adhesion of the active materials and trap dissolved polysulfides, but also possesses elastic properties, which can accommodate the volume expansion and maintain the integrity of electrode during cycling. On the other hand, the PPy-separator not only acts as a reservoir for soluble lithium polysulfides, but also acts as an upper current collector to accelerate the kinetics of the electrochemical reactions. Moreover, PPy is electrochemically active and could contribute capacity to Li-S batteries. Benefiting from the above advantages, the flexible Li-S battery can deliver an initial

discharge capacity of 1064 mA h g^{-1} and retains a capacity of 848 mA h g^{-1} after 20 cycles at 0.1 C. After repeated bending for 10 times, the capacity remains almost the same. In addition, the soft-packaged Li-S battery could power a device containing 24 white LEDs, both before and after bending, indicating its great potential application in flexible electronics. We believe that this flexible electrode structure may provide guidance for fabricating high energy, flexible electrochemical energy-storage devices.

CHAPTER 5 UNIFORM POLYPYRROLE-COATED SULFUR/GRAPHENE AEROGEL VIA VAPOR PHASE DEPOSITION TECHNIQUE FOR LI-S BATTERIES

5.1 Introduction

The rapid development of electric vehicles and grid-scale energy storage systems have promoted increasing demand for rechargeable batteries with high specific capacity and long lifetimes.[2, 215] Considerable attention has been paid to the lithium-sulfur battery due to its high theoretical energy density (2600 Wh kg^{-1}), low cost, and environmental friendliness,[10, 12, 216] although the practical application of Li-S battery is hampered by several issues.[15, 195, 217, 218] First of all, the low electronic conductivity of both sulfur and its discharge products (Li_2S/Li_2S_2) causes insufficient utilization of the active material and inferior rate capability. Another issue is that the large volume expansion (80%) of sulfur during discharge leads to mechanical instability of the electrode. Moreover, the intermediate products are soluble in electrolyte, so that they shuttle between the cathode and the anode, resulting in low coulombic efficiency, fast capacity fading, and short lifetimes.

To address these issues, great efforts have been made towards designing novel nanostructured carbonaceous/polymer host materials,[35, 219-227] adding a functional interlayer between the separator and the cathode,[93, 120, 228-230] or exploring advanced electrolytes.[231-234] The most common strategy is to combine the sulfur with one of a number of nanostructured carbonaceous matrices, including microporous/mesoporous carbon,[86, 235, 236] carbon nanotubes,[227, 237-239] carbon fibers,[33, 74] and graphene.[190, 208, 240, 241] Among these carbonaceous matrices, graphene has attracted considerable attention due to

its mechanical properties and high electrical conductivity. For example, Duan's group reported a freestanding three-dimensional (3D) graphene framework that could tolerate loading with a high amount of sulfur particles.[242] The 3D highly porous interconnected graphene network could facilitate electron transport, accommodate volume expansion, and also acts as an effective encapsulation layer to retard the polysulfide shuttling effect. The polysulfides were still dissolved into electrolyte, however, in the course of long cycling due to the weak interaction between the nonpolar graphene and the polar polysulfides. Therefore, additional adsorbents for lithium polysulphides, such as metal oxides/sulphides, or conductive polymer coatings, are essential to improve the cycling performance of carbon/sulfur composite cathodes.[77, 163, 243] Cui's group investigated the influence of three different polymers towards improving the electrochemical performance of sulfur cathode by coating a thin layer of polymer on hollow sulfur nanospheres.[84] It was found that the polymer could efficiently enhance the specific capacity and cycling life of the sulfur cathode due to the strong interaction between heteroatoms in the polymer and lithium ions in Li_xS ($0< x \leq 2$). The cycling performance was improved by coating with polymer, but the rate capability was still not satisfactory due to the limited conductivity of the polymer.

Herein, we have designed and synthesized a sulfur/graphene aerogel composite coated with a uniform polypyrrole (PPy) layer (PPy@S/GA-VD) via vapor phase deposition. The vapor phase method has been widely used to coat polymers on different substrates, and it shows many advantages over other methods for depositing polymers. First, in the vapor phase deposition method, the monomer is applied as a vapor instead of a solution, which can easily penetrate the pores of the sulfur/graphene composite, resulting in a uniform PPy coating layer. Moreover, much research has confirmed that the polymer layer formed by the vapor phase deposition method has high electronic conductivity.[244]

To the best of our knowledge, this is the first time that the vapor phase deposition technique has been applied to prepared sulfur cathode materials. The obtained PPy@S/GA-VD composite was expected to offer high specific capacity and good cycling stability. This is because the 3D graphene hydrogel will shrink in the deposition process, which can enhance the contact between the sulfur and the conducting agent, and afford short ionic and electronic transport distances. More importantly, the graphene sheets could act as a physical barrier to trap dissolved polysulfides and enhance the cycling stability. In addition, the uniform PPy layer coated on the S/GA composite serves as a cushion layer to buffer the volume expansion of sulfur and maintain the integrity of the electrode during cycling. Moreover, the PPy layer could act as container to efficiently block polysulfide penetration and suppress polysulfide dissolution by strong chemical adsorption, facilitating long and stable cycling performance. As a result, the designed PPy coated S/GA composite using the vapor phase deposition method delivered a capacity of 1167 mA h g^{-1} at 0.2 C. At 0.5 C, it still delivered a capacity of 698 mA h g^{-1} after 500 cycles with an ultra-slow decay rate of 0.03% per cycle. The uniform PPy layer coated S/GA composite with excellent cycling performance and high rate capability could act as a promising cathode for advanced Li-S batteries.

5.2 Experimental section

Synthesis of Sulfur/Graphene Hydrogel: Graphene oxide (GO) was synthesized by Hummers' method. For the preparation of the sulfur/graphene hydrogel, commercial sulfur and GO in a weight ratio of 8:2 were added into a vial with 20 ml distilled water. After sonication for 0.5 h, a uniform sulfur/GO suspension was obtained. Then, a certain amount of hypophosphorous acid was added, followed by sonication for 10 min. Afterwards, the suspension was placed in an oven at 60 °C overnight to obtain the

sulfur/graphene hydrogel. The sulfur/graphene hydrogel was carefully taken out and purified with distilled water for one week with frequent changes of water. To synthesize sulfur/graphene aerogel (S/GA), the sulfur/ reduced GO (S/rGO hydrogel) was directly freeze-dried overnight.

Vapor phase deposition method to prepare PPy coated S/graphene aerogel: The organic ferric salt iron (III) p-toluenesulfonate (FeToS) was dissolved in distilled water at a concentration of 20 wt% as oxidant. The obtained S/graphene hydrogel was put into the FeToS solution for about 24 h. Then, the hydrogel was taken out and placed in an oven at 100 ℃ for 20 min to form an oxidant layer on the surface of the S/graphene hydrogel. Then, the FeToS coated S/graphene sample was put into a vapor phase deposition chamber with pyrrole monomer on the bottom at 60 ℃ for 20 min. Afterwards, the sample was taken out and put on a hot plate at 50 ℃ for 30 mins, followed by washing with water and ethanol several times until a colourless solution was obtained. Then, the sample was freeze-dried and the PPy coated S/graphene aerogel (PPy@S/GA-VD) was obtained. By adjusting the deposition time, the amount of PPy coated on the S/GA composite was easily controlled.

Liquid phase deposition method to prepare PPy coated S/graphene aerogel: 20 wt% FeToS solution was added dropwise into 20 mL of a solution containing 37 μL pyrrole monomer, 75 μL concentrated hydrochloric acid (37%), and 160 mg of the obtained S/GA composite at 0-5°C. After constant stirring for 6 h, the precipitate was harvested by centrifugation, washed with distilled water several times, and dried at 50 ℃ under vacuum. The obtained black power was denoted as PPy@S/GA-CD composite.

Material characterizations: For physical and morphological characterization of the composites, X-ray diffraction patterns (XRD, GBC MMA 017) were collected over a 2θ

range of 10° - 80° with a scan rate of 2° min^{-1}. X-ray photoelectron spectroscopy (XPS) was conducted on a Vacuum Generator (VG) Scientific ESCALAB 2201XL instrument using Al Kα X-ray radiation and fixed analyzer transmission mode. Thermogravimetric analysis (TGA) was performed in air using a SETARAM instrument to estimate the amount of sulfur in the sample. The morphologies of the samples were investigated by field emission scanning electron microscopy (JEOL JSM-7500FA) and transmission electron microscopy (JEOL 2011, 200 keV). The TEM was linked to an energy dispersive spectral analysis (EDS) system, which used a probe corrected JEOL ARM200F instrument.

Electrochemical Measurements: For the electrochemical measurements of the S/GA, PPy@S/GA-CD, and PPy@S/GA-VD composites as cathode for Li-S batteries, CR2032 coin type cells were assembled. The electrodes were prepared by mixing the S/GA, PPy@S/GA-CD, and PPy@S/GA-VD with poly(vinylidene fluoride) (PVDF) and Super P in a weight ratio of 8:1:1, respectively. The resultant slurries were coated on aluminum foil and dried in a vacuum oven at 60 °C overnight. The mass loading of the sulfur cathode was about 1 mg cm^{-2}. The electrolyte was 1 M lithium bis(trifluoromethanesulfonyl)imide (LiTFSI) in 1,3-dioxolane (DOL)/1,2-dimethoxyethane (DME) (1:1 by volume) containing 0.1 M $LiNO_3$ as additive. The amount of electrolyte used in coin cell is 15 uL g^{-1} based on the sulfur amount in electrodes. To evaluate the electrochemical performance of the Li-S cells, an automatic battery test system (Land®, China) was used at room temperature. Electrochemical impedance spectroscopy (EIS) and cyclic voltammetry (CV) measurements were performed on a Biologic VMP 3 electrochemical workstation over the frequency range of 10 mHz to 100 kHz, and the scan rate was 0.1 mV s^{-1} within a 1.7 V to 2.8 V voltage window. The cycling performance and rate capability tests were carried out with a LAND

battery test system at different current densities (1 C = 1675 mA g^{-1}) within the voltage range of 1.7 - 2.8 V.

5.3 Results and discussion

5.31. Structure and morphology

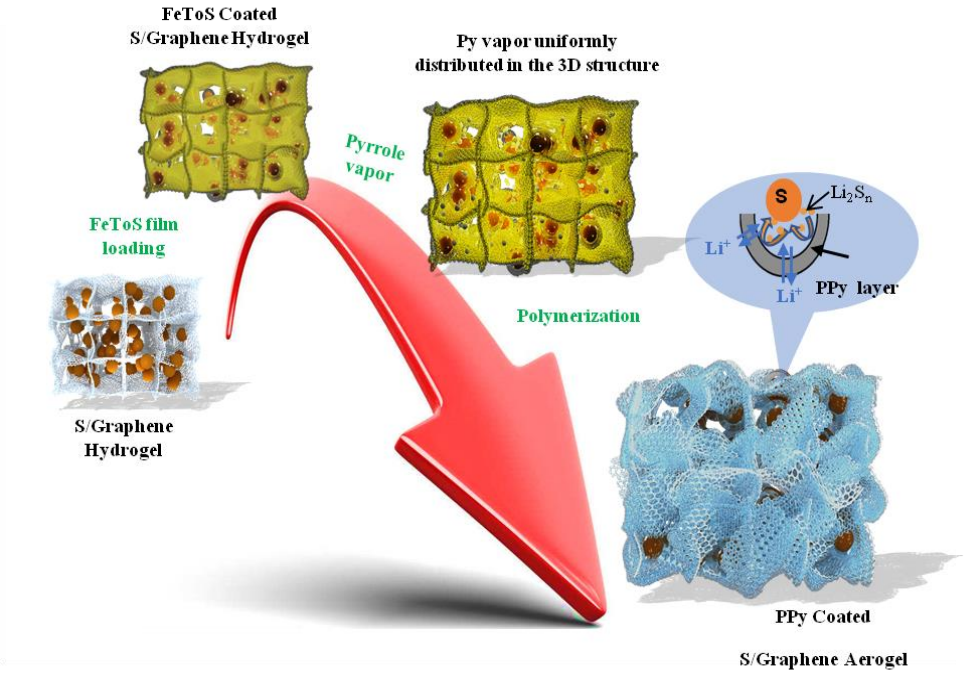

Figure 5.1. Schematic illustration of the main synthesis process for PPy@S/GA-VD composite.

The synthetic process for the PPy@S/GA-VD composite is illustrated in Figure 5.1. Firstly, graphene oxide (GO) and commercial sulfur were mixed under high energy probe sonication to obtain a uniform suspension. Then, a 3D porous sulfur/graphene hydrogel was obtained via a process of self-assembly at 60 °C overnight, as shown in Figure 5.2. The obtained hydrogel was immersed in iron(III) p-toluenesulfonate (FeToS) solution for several hours, and then the solvent was evaporated at 100 °C and resulting in the formation of a uniform FeToS oxidant layer on the surface of the hydrogel. Then, the

FeToS coated sulfur/graphene hydrogel was transferred into a chamber saturated with pyrrole (Py) monomer vapor to grow a uniform and thin PPy layer. By adjusting the deposition time (15, 20, and 25 mins), the samples with different PPy layer thicknesses were obtained. During the vapor phase deposition process, the obtained hydrogel would shrink owing to the capillary force between the solvent and the graphene sheets, so that a crumpled morphology could be produced, which could enhance the interface contact between sulfur and the conductive agent, improve the conductivity, and provide fast electron transport as well.[245] For comparison, we also applied a chemical deposition method to coat a PPy layer on the S/GA composite, with the resulting sample denoted as PPy@S/GA-CD composite.

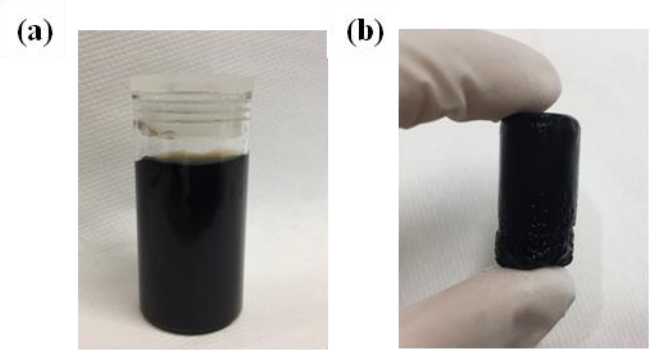

Figure 5.2. The photos of (a) sulfur and GO suspension and (b) the obtained S/graphene hydrogel.

The structural characterization of the as-prepared PPy, GA, S/GA, PPy@S/GA-CD, and PPy@S/GA-VD was conducted by X-ray diffraction (XRD), as shown in Figure 5.3a. For all the samples, the pronounced peaks could all be assigned to orthorhombic sulfur (JCPDS card No: 08-0427) with high crystallinity. The peaks of graphene and PPy are barely detectable in these obtained composites due to their low content and poorly crystallized or amorphous phase. The intensity of the sulfur peaks in the S/GA, PPy@S/GA-CD, and PPy@S/GA-VD composites is much lower than for the pure sulfur,

indicating the successful coating of graphene and PPy on the surfaces of sulfur particles. Thermogravimetric analysis (TGA) was performed under pure argon atmosphere to determine the content of sulfur, PPy, and graphene in the S/GA, PPy@S/GA-CD, and PPy@S/GA-VD composites. As shown in Figure 5.3b, the content of sulfur in S/GA was 80%. After the PPy coating, the sulfur content in the PPy@S/GA-VD and PPy@S/GA-CD composites was reduced to 65% and 63%, respectively, which are similar values, making it appropriate to compare the electrochemical performances of these two samples.

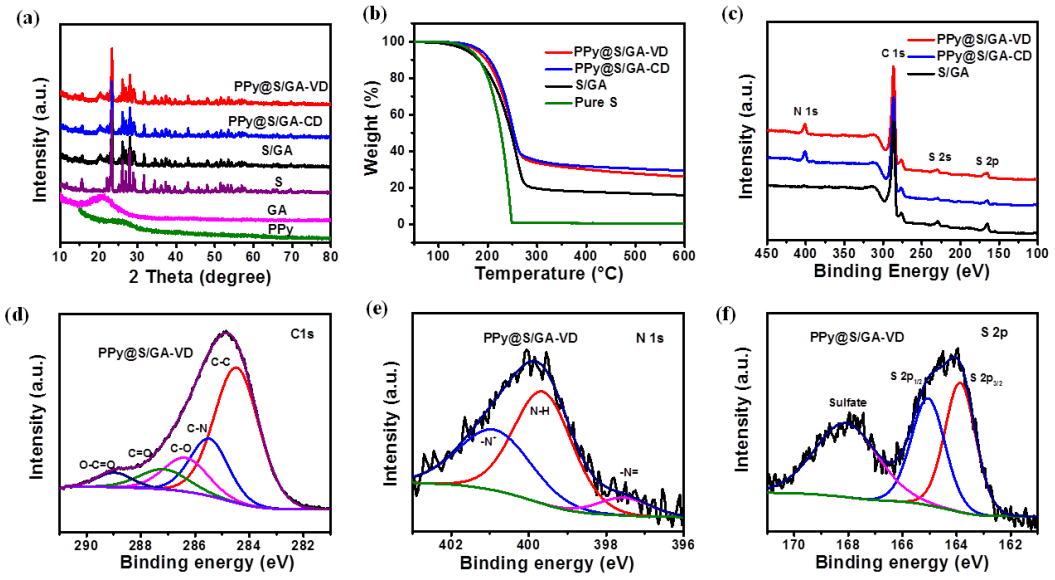

Figure 5.3. (a) XRD patterns of the obtained samples. (b) TGA curves of pure S, and S/GA, PPy@S/GA-CD, and PPy@S/GA-VD composites. (c) XPS survey spectra of S/GA, PPy@S/GA-CD and PPy@S/GA-VD composites. The fitted high-resolution (d) C 1s, (e) N 1s, and (f) S 2p XPS spectra of PPy@S/GA-VD composite.

The surface chemical interaction was investigated by X-ray photoelectron spectroscopy (XPS). Figure 5.3c displays the XPS survey spectra of the S/GA, PPy@S/GA-CD, and PPy@S/GA-VD composites. The peak at 400 eV corresponds to N 1s, the one at 286 eV to C 1s, and the two located at 229.5 eV and 165 eV belong to S 1s and S 2p, respectively.

Compared with the S/GA composite, there is a new N 1s peak that appears in the XPS spectra of the PPy@S/GA-CD and PPy@S/GA-VD composites, which comes from PPy layer, indicating the successful deposition of PPy on the surface of the S/GA composite. High-resolution spectra of C 1s, N 1s, and S 2p for the PPy@S/GA-VD composite are clearly presented in Figure 5.3d-f. The C 1s spectrum is fitted into 5 peaks: C-C at 284.7 eV, C-N at 285.6 eV, C-O at 286.5 eV, C=O at 287.4 eV, and C-C=O at 289.0 eV (Figure 5.3d).[246, 247] Compared with the S/GA composite (Figure 5.4), the C-N bond only appears after the PPy coating. The N 1s spectrum is deconvoluted into 3 peaks centred at 399.7 eV, 397.6 eV, and 401.0 eV, corresponding to pyrrole nitrogen (N-H), the imine-like (-N=) structure, and positively charged nitrogen ($-N^+$), respectively, indicating the presence of PPy (Figure 5.3e).[248] Moreover, the high-resolution spectrum of the S 2p region (Figure 5.3f) is fitted into three peaks. The binding energy at 163.8 eV corresponds to S $2p_{3/2}$, which is slightly lower than for elemental sulfur (164 eV), revealing the possible presence of C-S species, while the binding energy at 164.9 eV corresponds to S $2p_{1/2}$. The peak at 168.1 eV can be ascribed to the sulfate species arising from the oxidation of sulfur by air or an oxidizing agent.[246]

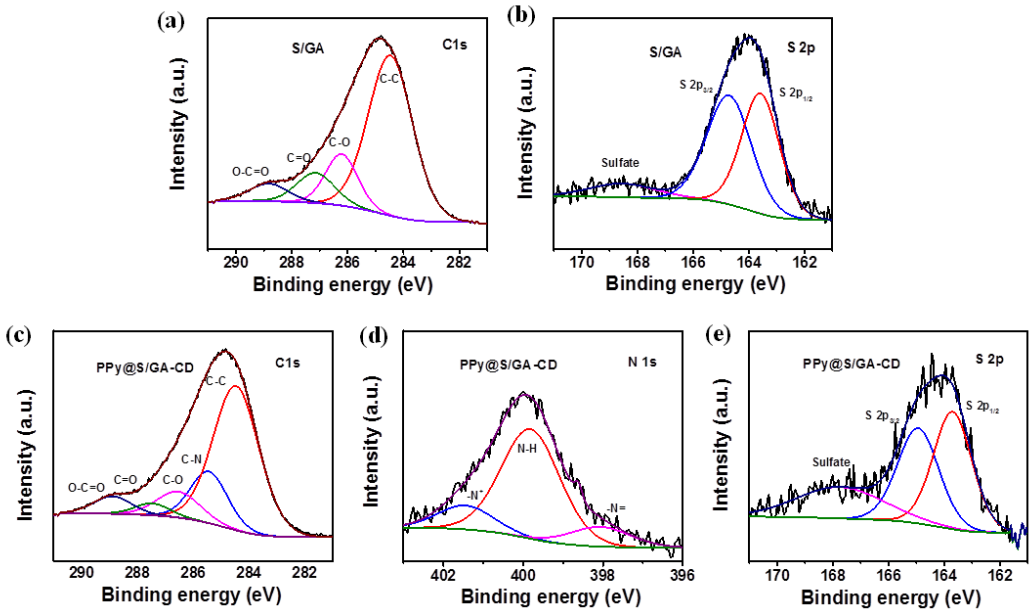

Figure 5.4. The fitted high-resolution a) C 1s and b) S 2p XPS spectra of S/GA composite; (c) C 1s, (d) N 1s and (e) S 2p XPS spectra of PPy@S/GA-CD composite.

The morphology of the S/GA, PPy@S/GA-CD, and PPy@S/GA-VD composites was investigated via field-emission scanning electron microscopy (FESEM) (Figure 5.5a-c). Figure 5a shows that sulfur particles were embedded in the graphene nanosheet matrix in the S/GA composite, which could improve the conductivity and utilization of sulfur, yielding high specific capacity during cycling. After the PPy deposition, however, the composites synthesized with different deposition methods show different morphologies. The PPy@S/GA-CD composite still maintain the same morphology as that of S/GA, except that the graphene nanosheets have become thicker due to the PPy coverage (Figure 5.5b). The PPy@S/GA-VD composite displays smaller pores, however, and more wrinkled graphene nanosheets than t the S/GA and PPy@S/GA-CD composites (Figure 5.5c), which is possibly due to the shrinkage of the gel during the vapor phase deposition process for coverage with PPy. The crumpled matrix could further enhance the contact

between the active materials and the conductive agent, improving the utilization of sulfur during cycling.

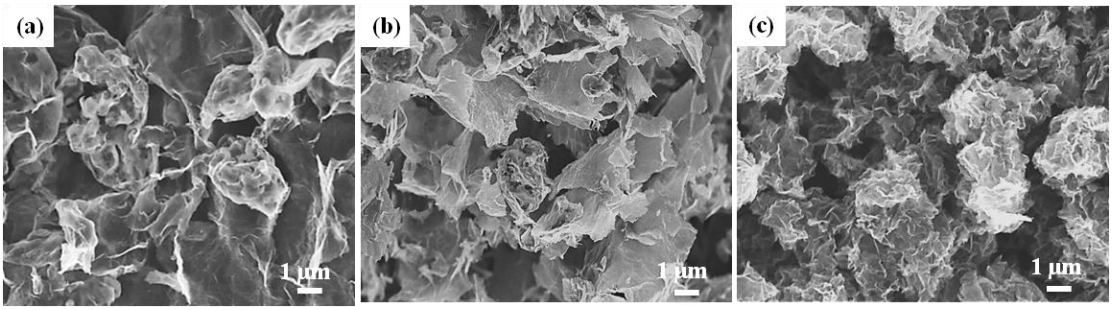

Figure 5.5. Scanning electron microscope (SEM) images of a) S/GA, b) PPy@S/GA-CD, and c) PPy@S/GA-VD composites.

PPy@S/GA-VD composites with different amounts of PPy layer were also prepared by adjusting the vapor phase deposition time, and scanning electron microscope (SEM) images are shown in Figure 5.6a-c. It can be clearly observed that with increasing deposition time, the graphene nanosheets became thicker due to the increased amount of PPy layer that was coated on them. TGA curves were collected for these three samples to confirm the amount of S, PPy, and graphene, which are shown in Figure 5.6d and summarized in Table 5.1. The cycling performances of the three samples are presented in Figure 5.6e and f. Sample-2 and Sample-3 (20 and 25 min PPy deposition time, respectively) show better cycling stability than Sample-1 (15 min deposition time) due to the superior ability of a thicker layer of PPy to anchor polysulfides and mitigate the shuttle effect. The specific capacity of Sample-3 is slightly lower than that of Sample-2, however, and an activation process appears in sample-3, which can be ascribed to the thick PPy layer coated on the S/GA composite, leading to low reaction kinetics. When the calculated capacity is based on whole cathode materials, the superiority of Sample-2 over Sample-3 is more obvious **(**Figure 5.6f**).** Therefore, considering the balance between high

sulfur loading and stable electrochemical performance, Sample-2 with 20 min deposition time was selected for further study.

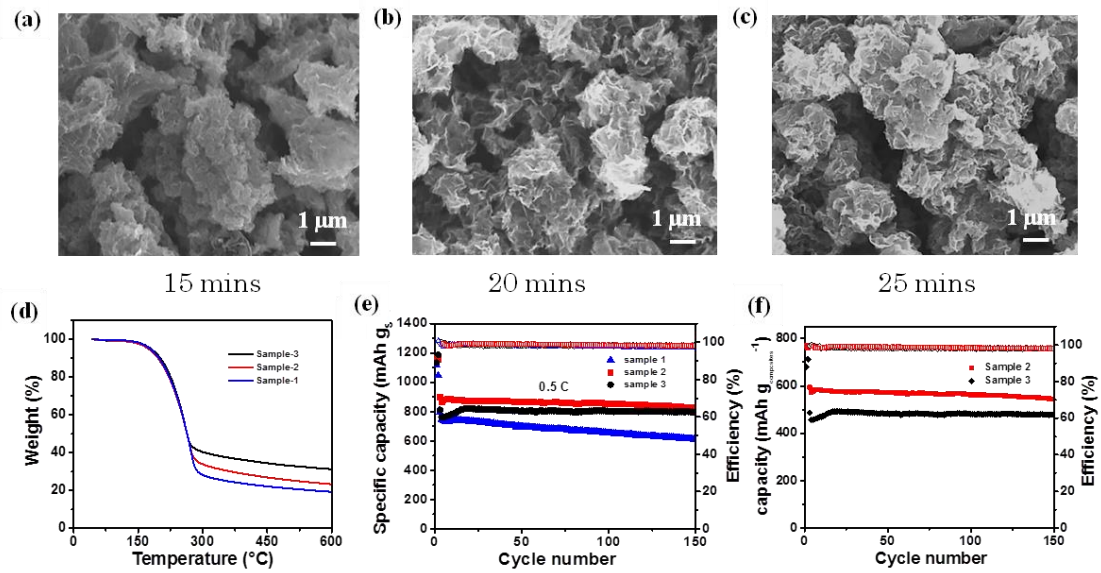

Figure 5.6. The SEM images of PPy coated S/GA composites with different deposition time: (a) 15 mins: sample-1, (b) 20 mins: sample-2 and (c) 25 mins: sample-3. (d) The TGA curves of different samples; the cycling performance of different samples (e) capacity based on sulfur and (f) capacity based on the whole cathode materials.

Table 5.1 The content of S, graphene and PPy in the different samples.

Material	**Deposition time**	**Sulfur (%)**	**rGO (%)**	**PPy (%)**
Sample-3	25 mins	60	12	28
Sample-2	20 mins	65	16.25	18.75
Sample-1	15 mins	72	18	10

The morphology of PPy@S/GA-VD composite was further investigated via transmission electron microscopy (TEM). The typical image exhibits S particles that are fully encapsulated in the crumpled PPy@GA matrix (Figure 5.7a). The high-resolution TEM

(HRTEM) image clearly shows the lattice fringes of sulfur particles, which are covered by graphene sheets and the PPy layer, and a PPy layer with a thickness of several nanometres was uniformly coated on the outside of the graphene sheets (Figure 5.7b). The HRTEM image of PPy@S/GA-CD composite (Figure 5.7c), however, shows that the PPy layer was randomly coated on the graphene layer, indicating that the vapor phase method could grantee a more uniform PPy layer than the chemical deposition method. From the HRTEM image of PPy@S/GA-VD composite (Figure 5.7d), the amorphous PPy layer is very uniform and covers all the wrinkled graphene sheets, while the PPy layer only covers the outside of the graphene sheets in the PPy@S/GA-CD composite (Figure 5.7e). This further confirms that the pyrrole monomer vapor could easily penetrate the pores of the FeToS coated sulfur/graphene hydrogel and form a uniform PPy layer on the graphene nanosheets.

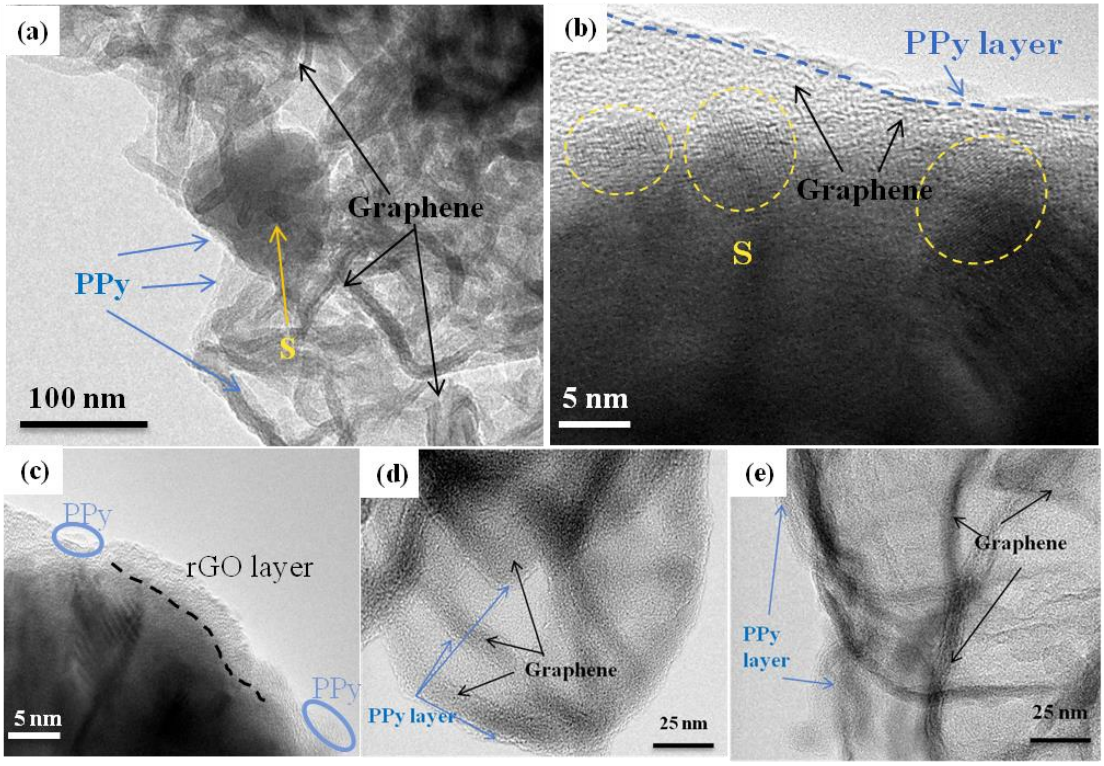

Figure 5.7. (a) Transmission electron microscope (TEM) and (b, d) high resolution TEM (HRTEM) images of PPy@S/GA-VD composites, (c, e) HRTEM images of PPy@S/GA-CD composites.

The corresponding scanning TEM (STEM) and energy dispersive spectroscopy (EDS) element mapping images of PPy@S/GA-VD and PPy@S/GA-CD composites are also presented in Figure 5.8. The homogeneous distributions of carbon, sulfur, and nitrogen can be obtained in PPy@S/GA-VD composites (Figure 5.8a-d), while the EDS element mapping images of PPy@S/GA-CD (Figure 5.8e-h) indicated that the non-uniform nitrogen distribution was observed in this structure due to the random distribution of the PPy layer on the S/GA composite.

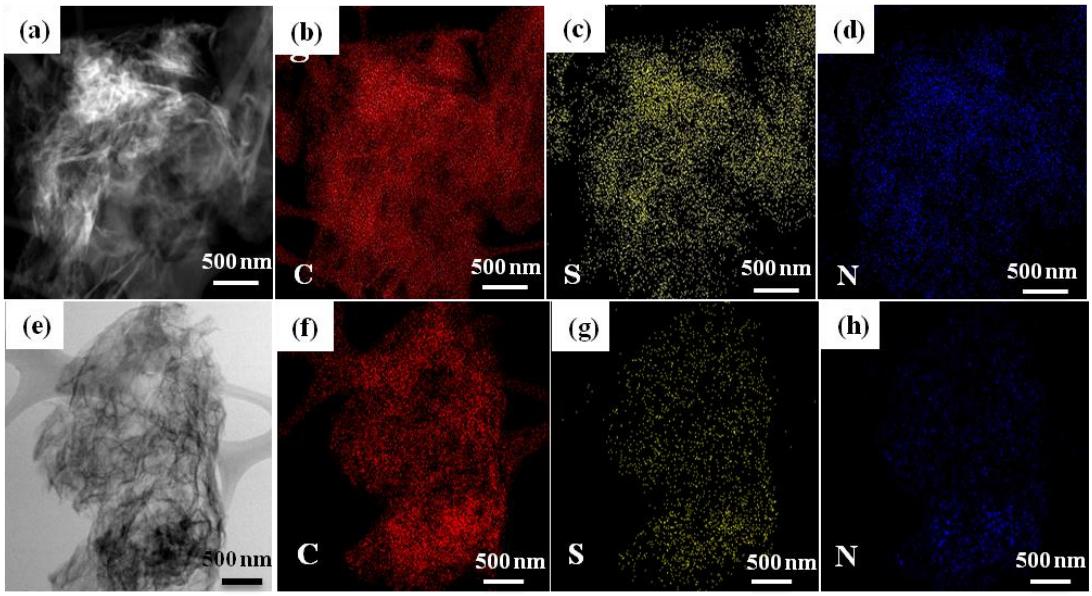

Figure 5.8. Scanning TEM (STEM) image and corresponding elemental mapping of PPy@S/GA-VD composites (a-d) and PPy@S/GA-CD composites (e-h).

5.3.2 Electrochemical characterizations

Figure 5.9 presents the electrochemical performances of the S/GA, PPy@S/GA-CD, and PPy@S/GA-VD composites. Figure 5.9a shows the cyclic voltammetry (CV) curves for the initial five scans of PPy@S/GA-VD composite at a scan rate of 0.1 mV s^{-1} between 1.7 and 2.8 V. The CV curves show two typical cathodic peaks and two anodic peaks. The first cathodic peak located at about 2.3 V represents the reduction of sulfur to soluble long-chain polysulfides (Li_2S_n, $2 < n \leq 8$), and the second cathodic peak at ~2.0 V is due to the further reduction of soluble polysufides to lithium sulfides (Li_2S_2/Li_2S). At around 2.4 V, the anodic peaks reveal the conversion from lithium sulfides to lithium polysulfides, and finally to sulfur.[13] The CV curves for subsequent cycles show good reproducibility with an overlapping of all the peaks, suggesting the good reversibility of the multistep reactions. The CV curves of S/GA and PPy@S/GA-CD composite were also collected, as shown in Figure 5.11, and they both feature lower current density and

wider cathodic and anodic peaks than the PPy@S/GA-VD composite, indicating sluggish kinetics during cycling.[33] Representative charge/discharge voltage profiles of PPy@S/GA-VD at 0.2 C with a cut-off voltage window of 1.7 -2.8 V are shown in Figure 5.9b. Consistent with the CV curves, the discharge profiles contain two typical plateaus: the high plateau at ~ 2.3 V is related to the formation of long-chain polysulfides, and the low plateau at ~ 2.1 V corresponds to the formation of low-order polysulfides during discharge. The discharge plateaus are long and flat, and the profiles show nearly the same shape, even after 100 cycles, indicating stable energy output.

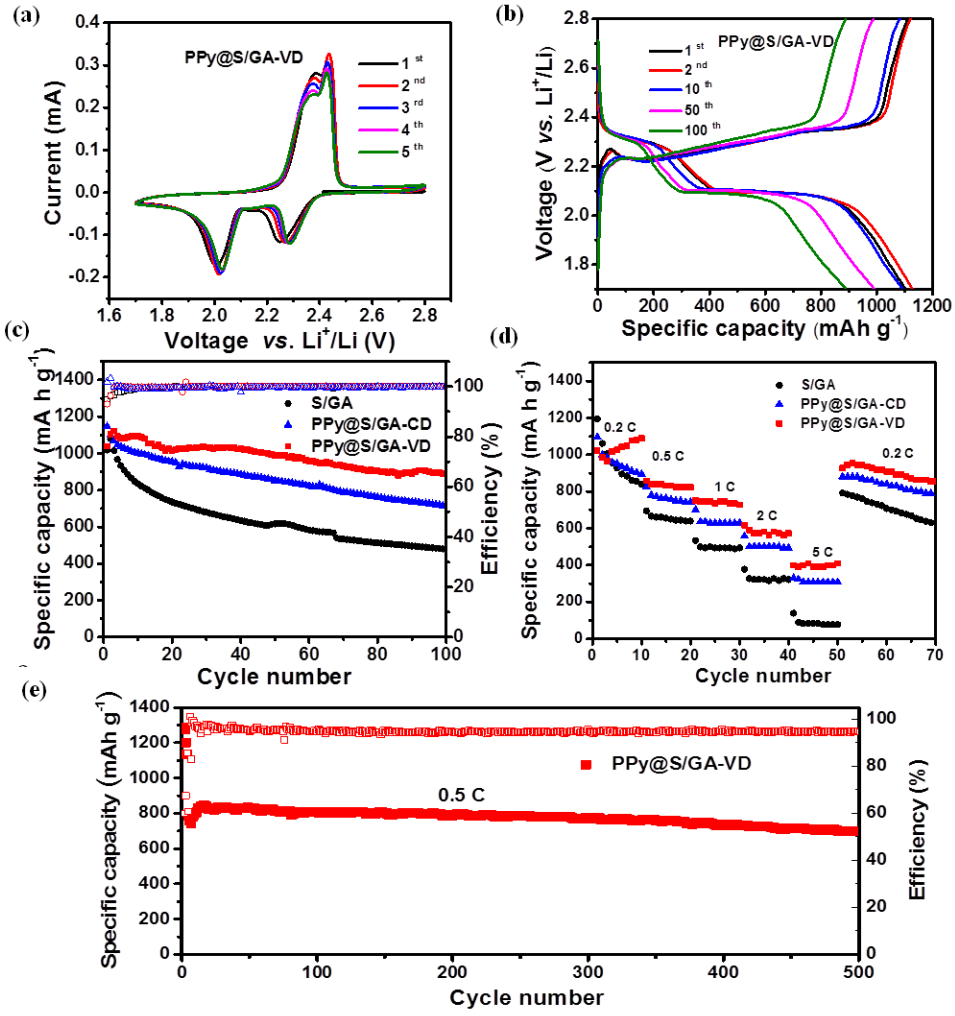

Figure 5.9. (a) Cyclic voltammetry curves for the first five cycles of PPy@S/GA-VD composite. (b) Charge-discharge voltage profiles for selected cycles of PPy@S/GA-VD

composite at a current density of 0.2 C. (c) Cycling performances of PPy@S/GA-VD, PPy@S/GA-CD, and S/GA composites at 0.2 C. (d) Rate performances of PPy@S/GA-VD, PPy@S/GA-CD, and S/GA composites at different current densities. (e) Long-term cycling performance of PPy@S/GA-VD composite at 0.5 C (1 C = 1675 mA g^{-1}).

The cycling performances of Li-S batteries containing S/GA, PPy@S/GA-CD, and PPy@S/GA-VD as electrodes at a current rate of 0.2 C are presented in Figure 5.9c. The S/GA electrode shows dramatic capacity fading, since it has a discharge capacity of 1019 mA h g^{-1} in the first cycle that decreases to 479 mA h g^{-1} after only 100 cycles. Compared to S/GA, the PPy@S/GA-CD electrode shows relatively stable cycling performance with an initial specific capacity of 1146.6 mA h g^{-1}, which gradually decreases to 716.2 mA h g^{-1} after 100 cycles. The PPy@S/GA-VD electrode, however, shows a more stable electrochemical performance than that of PPy@S/GA-CD electrode, delivering a second cycle specific capacity of 1103 mA h g^{-1}. A high capacity of 890 mA h g^{-1} is still maintained after 100 cycles with a slow decay rate of 0.19% per cycle. From the above results, we can conclude that, the cycling stability is significantly improved after coating with the PPy layer, suggesting that the PPy could efficiently adsorb lithium polysulfides, mitigate the shuttle effect, and enhance the utilization of active materials. In addition, the superior electrochemical stability of the PPy@S/GA-VD electrode should be ascribed to the uniform PPy layer and the shrinkage in the structure obtained from the vapor phase deposition method. Figure 5.9d shows the rate capabilities of the S/GA, PPy@S/GA-CD, and PPy@S/GA-VD electrodes. Obviously, the PPy@S/GA-VD electrode exhibits the best rate capability: it delivers discharge capacities of 1009.1, 918.1, 745.4, 590.9, and 409.1 mA h g^{-1} at the current densities of 0.2, 0.5, 1, 2, and 5 C, respectively. When the current density is reversed back to 0.2 C, a specific capacity of 945.5 mA h g^{-1} still can be

obtained. At the relatively higher current density of 0.5 C, the PPy@S/GA-VD electrode still delivers a capacity of 698 mA h g^{-1} after 500 cycles with an ultra-slow decay rate of 0.03% per cycle (Figure 5.9e). The cycling performances of recently reported polypyrrole-based sulfur cathode materials are summarized in Table 5.2. Compared with the recently reported polypyrrole-based cathodes, the PPy@S/GA-VD electrode demonstrates the best cycling stability.

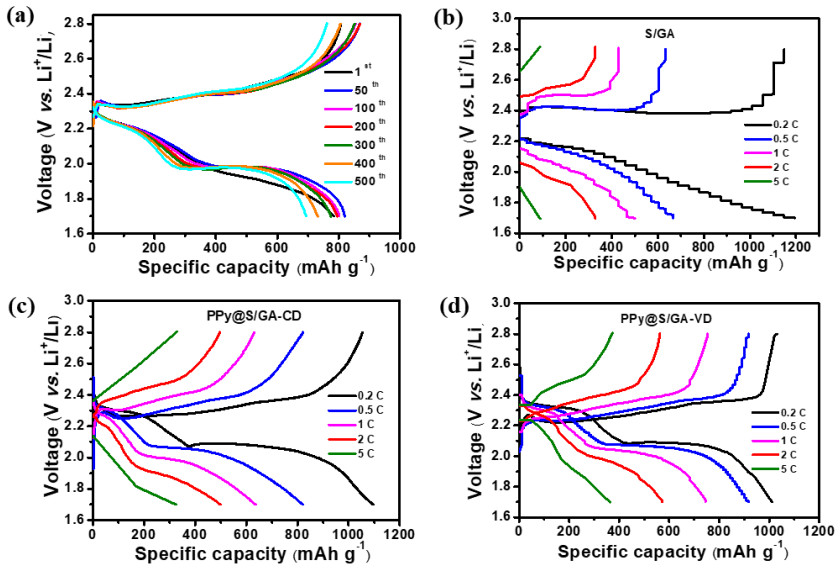

Figure 5.10. (a) Charge-discharge voltage profiles for selected cycles of PPy@S/GA-VD composite during the long-term cycles at a current density of 0.5 C. Charge-discharge voltage profiles for (b) S/GA, (c) PPy@S/GA-CD, and (d) PPy@S/GA-VD composites at different current density.

The selected charge-discharge curves of PPy@S/GA-VD composites during the 500 cycles was shown in Figure 5.10a. The discharge plateaus are long and flat, and the profiles show nearly the same shape, even after 500 cycles, indicating stable energy output. The selected charge-discharge curves of PPy@S/GA-VD, PPy@S/GA-CD, and S/GA composites at different current density were also shown in Figure 5.10b-d. These three samples all show long and flat discharge plateaus at low current density. When the

current density increased to 5 C, the discharge plateaus of PPy@S/GA-CD, and S/GA composites is disappearing, while the PPy@S/GA-VD composites still show a relative flat plateaus, indicating its stable output at high current density.

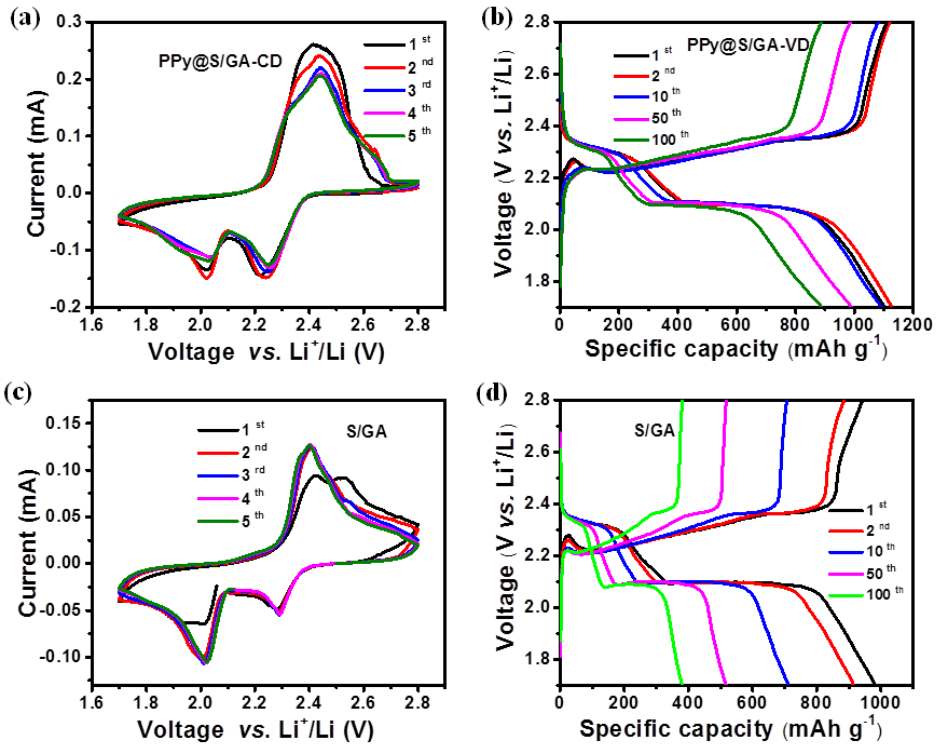

Figure 5.11. (a) Cyclic voltammetry curves for the first five cycles of PPy@S/GA-CD composite. (b) Charge-discharge voltage profiles for selected cycles of PPy@S/GA-CD composite at a current density of 0.2 C. (c) Cyclic voltammetry curves for the first five cycles of S/GA composite. (d) Charge-discharge voltage profiles for selected cycles of S/GA composite at a current density of 0.2 C.

To validate the synergistic effects of graphene and the PPy layer towards mitigating the dissolution of polysulfides during the charge/discharge process, the cells were disassembled in fully charged state after 100 cycles, and the cycled PPy@S/GA-VD, PPy@S/GA-CD, and S/GA electrodes were soaked in dioxolane/dimethoxyethane (DOL/DME) (v:v = 1:1) solution for 12 hours, and the absorption spectra of the obtained

solutions were collected using ultraviolet-visible (UV-vis) spectroscopy. The colour changes of the DOL/DME solutions exposed to the different electrodes were recorded using digital photographs, as shown in Figure 5.12a. The cycled PPy@S/GA-VD electrode solution shows the lightest yellow colour compared with the other electrode solutions due to having the lowest content of polysulfides in solution. Figure 5.12b shows the UV-vis spectra of the obtained solutions. The intensity of the adsorption peak of PPy@S/GA-VD electrode is lower than for the other two samples, which indicates that the uniform PPy layer could efficiently anchor and reduce the dissolution of the produced polysulfides, as well as improving the utilization of the active materials.

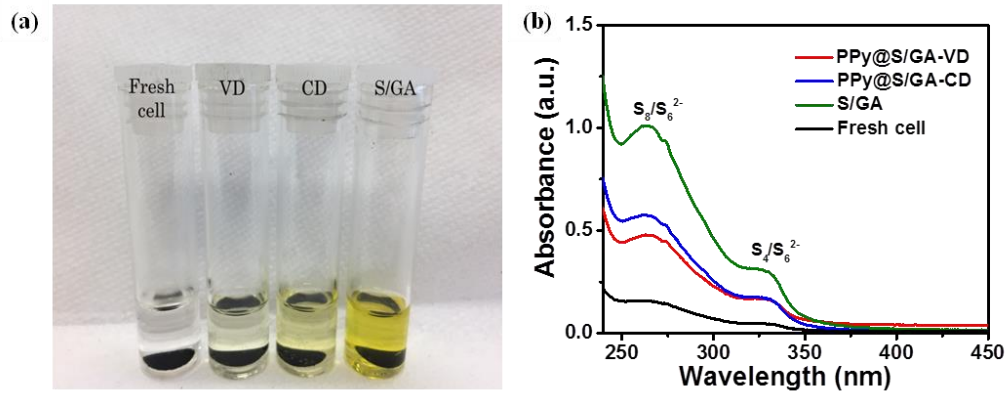

Figure 5.12. (a) Typical colours and (b) UV/vis absorption spectra of DOL/DME solutions with S/GA, PPy@S/GA-CD, and PPy@S/GA-VD electrodes after 100 cycles.

To investigate the effects of prepared composites towards suppressing the dissolution of polysulfides, the lithium anodes, separators, and cathodes were examined after cycling. SEM images of the Li anode surface after 100 cycles are shown in Figure 5.13a, e, and i. Compared with the fresh metallic Li, the Li anode from the cell with the PPy@S/GA-VD cathode exhibits a relatively smooth surface (Figure 5.13a), which indicates that the polysulfides are mainly trapped on the cathode side rather than travelling to the anode side. There is a thin film of Li_2S_2/Li_2S that is deposited on the lithium anode from the cell

with the PPy@S/GA-CD cathode (Figure 5.13e), indicating that some dissolved polysulfides penetrated through the separator and reacted with lithium. In contrast, the lithium anode from the cell with S/GA cathode is fully covered by a thick Li_2S_2/Li_2S film (Figure 5.13i), showing a severely damaged surface caused by the reaction of lithium with polysulfides. This phenomenon illustrates the superior ability of the PPy@S/GA-VD composite to suppress the shuttle effect and prevent the corrosion of the Li anode during cycling due to the uniformly coated PPy layer on the outside of the S/GA composites as a result of the vapor phase deposition method. Since the separator is closely compressed on the surface of the cathode electrode in the tightly sealed coin cell, the area of orange lithium polysulfides on the separator could also reflect their dissolution from the cathode. The trace of dissolved lithium polysulfides on the separator from the PPy@S/GA-VD cell shows inconspicuous colouring and the smallest area, implying that the most effective restriction of lithium polysulfides takes place in the PPy@S/GA-VD cathode (Figure 5.13b). In contrast, the orange areas on the separators of the PPy@S/GA-CD and S/GA cells are much larger, and the colours are more distinct than that of the PPy@S/GA-VD cell (Figure 5.13b, f, and j), indicating that significant amounts of lithium polysulfides are dissolved from the PPy@S/GA-CD and S/GA cathodes during the cycling. These observations are consistent with the electrochemical performance results and visually demonstrate that PPy@GA-VD serves as a great conductive matrix for Li-S batteries. SEM images of the electrodes before and after cycling were also shown in Figure 5.13. The PPy@S/GA-VD cathode well maintains its porous 3D structure (Figure 5.13c), indicating good mechanical stability during the electrode preparation process. After cycling, PPy@S/GA-VD shows no obvious changes compared with the fresh electrode, and no clear sulfur aggregation is observed. In the case of the PPy@S/GA-CD and S/GA electrodes, compared with the fresh electrodes (Figure

5.13g and k), aggregated sulfur particles are clearly evident on the surfaces of the cycled electrodes (Figure 5.13h and l), which may be derived from the oxidation of dissolved lithium polysulfides and their rearrangement on the conductive matrixes. These results also suggest that the PPy@S/GA-VD composite has superior capability of trapping polysulfides inside the matrix and avoiding their dissolution during the charge/discharge process.

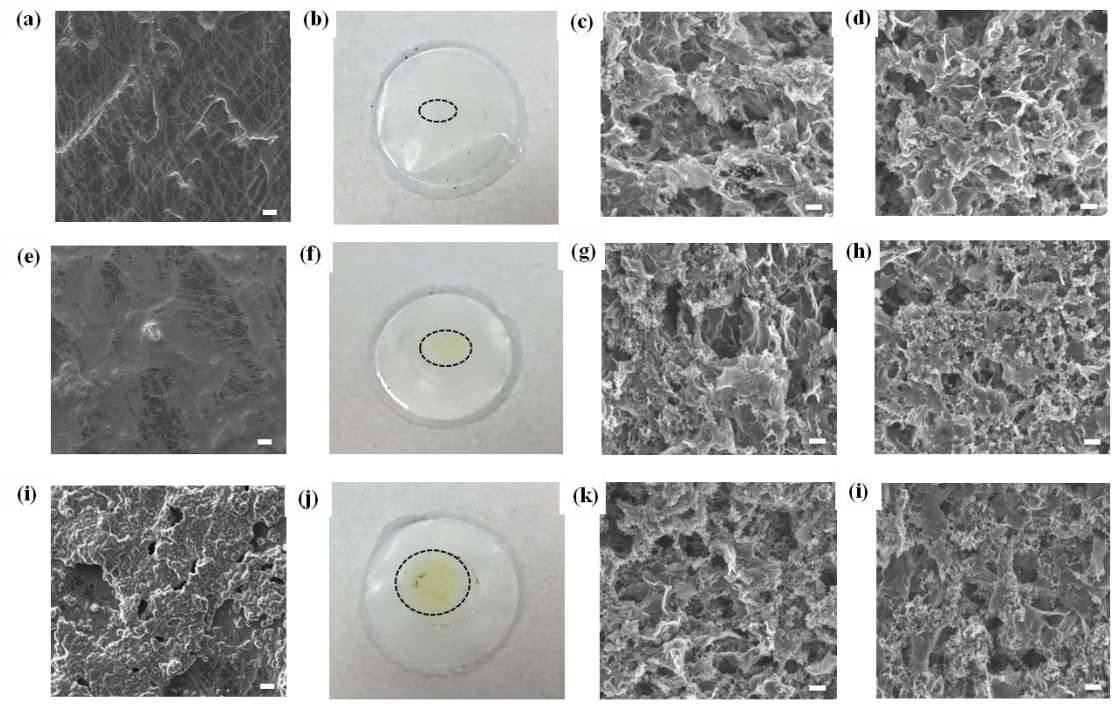

Figure 5.13. SEM images of (a, e, i) lithium anodes and (b, f, j) photographs of separators from the cells with PPy@S/GA-VD, PPy@S/GA-CD, and S/GA electrodes after 100 cycles, respectively. SEM images of PPy@S/GA-VD electrode (c) before and (d) after 100 cycles; SEM images of PPy@S/GA-CD electrode (g) before and (h) after 100 cycles; SEM images of S/GA electrode (k) before and (l) after 100 cycles. Scale bar: 10 μm (a, e, i); Scale bar: 2 μm (c, d, g, h, k, l).

The excellent electrochemical performance of PPy@S/GA-VD electrode should be ascribed to the unique design of its structure, as shown in Figure 1, which illustrates the

advantages of vapor phase deposition method for obtaining the uniform PPy layer and crumpled morphology of PPy@S/GA-VD composite to improve the utilization of active materials and ensure good cycling stability. The sulfur particles are initially encapsulated by the graphene nanosheets in the in-situ self-assembly process. After that, a uniform PPy layer fully covered the S/GA composite in the course of the vapor phase deposition process, which can act as container to efficiently block polysulfide penetration and suppress polysulfide dissolution by strong chemical adsorption, delivering long and stable cycling performance. In addition, the PPy layer could also buffer the volume expansion of sulfur and maintain the integrity of the electrode during cycling due to its excellent mechanical elasticity,[192] which can be demonstrated by the SEM images of PPy@S/GA-VD electrode after 100 cycles, indicating that its same original structure is maintained as before cycling (Figure 5.13c and d). A crumpled and shrunken graphene matrix was produced by vapor phase deposition process. This specially designed structure enhances the interface contact between the sulfur and the conductive agent, and it also provide fast electron transport, as can be confirmed by the electrochemical impedance spectra (Figure 5.14). Due to the synergistic effects of the 3D graphene matrix and the PPy layer, the designed PPy@S/GA-VD electrode delivered high specific capacity and excellent cycling stability.

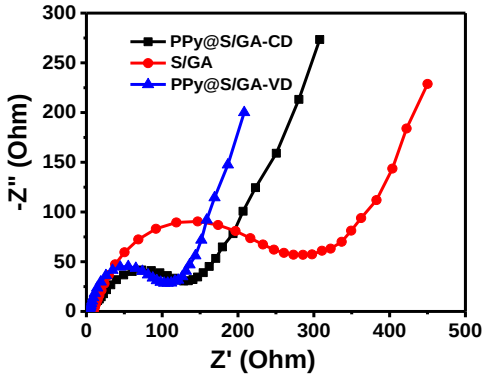

Figure 5.14. Electrochemical impedance spectra of PPy@S/GA-VD, PPy@S/GA-VD, and S/GA composites before cycling.

Table 5.2. Comparisons of cycling performances of this work with the reported polypyrrole-based cathode for Li-S batteries.

Materials	1st discharge capacity (mA h g^{-1})	Cycle number	Capacity after the reported cycles (mA h g^{-1})	Capacity delay rate (per cycle)	Refs.
PPy coated S/GA	828.2 (0.5 C)	500	698 (0.5 C)	0.03%	**This work**
PPy/S@PPy +PPy-separator	1144 (0.2 C)	200	994 (0.2 C)	0.06%	[249]
PPy coated S@GCS	925 (0.5 C)	100	750 (0.5 C)	0.19%	[85]
S/PPy-MnO_2 nanotubes	850 (1C)	500	550 (1C)	0.07%	[250]
PPy coated AB/S	847 (0.5 C)	200	630 (0.5 C)	0.13%	[210]
PPy coated S spheres	961 (0.2 C)	50	530 (0.2 C)	0.9%	[211]
Core-shell PPy@S	1142 (0.1 C)	100	725 (0.1 C)	0.36%	[212]
PPy@S@PPy	800 (0.1 C)	50	550 (0.1 C)	0.62%	[149]
sulfur-polypyrrole composite	1043 (0.06 C)	30	500 (0.06 C)	1.7%	[213]
PPy@MnO_2@S sphere	930.2 (0.5C)	500	704.1 (0.5C)	0.048%	[251]
Core-shell S@PPy nanoparticles sandwiched in rGO	908.7 (0.2 C)	200	538.7 (0.2 C)	0.18%	[252]
3D ordered porous S/PPy composites	1225 (0.1 C)	100	751 (0.1 C)	0.38%	[253]
Sulfur-Polypyrrole composites	1085 (1C)	100	617 (1C)	0.43%	[254]

Polypyrrole warped mesoporous C/S composites	1099 (0.2C)	100	880 (0.2C)	0.2%	[255]
S/polypyrrole hollow nanosphere with wrinkled shell	1074.2 (0.5C)	100	781.5 (0.5C)	0.27%	[256]
S/Al_2O_3/PPy ternary hybrid	868 (1C)	100	565 (1C)	0.35%	[257]
S anchored on interconnected PPy nanofiber network	958 (0.5C)	50	547 (0.5C)	0.85%	[258]
Polypyrrole grafted rGO-S nanocomposite	991.5 (1C)	400	626.7 (1C)	0.09%	[223]
graphene-Polypyrrole/sulfur-Graphene sandwich structure	1165 (0.1 C)	50	680 (0.1 C)	0.83%	[218]

5.4 Conclusions

In summary, a porous integrated sulfur/graphene aerogel with uniform PPy coating layer was designed via vapor phase deposition method as cathode material for Li-S batteries. The sulfur particles are encapsulated and firmly sealed by conductive graphene nanosheets, which not only provides a 3D conductive network to improve the utilization of sulfur and shorten electronic transfer distance, but also physically trapped dissolved polysulfides. More importantly, the uniform PPy layer coated on the outside of S/GA composites act as chemical adsorbent agent for polysulfides to mitigate the shuttle effect and ensure a long stable cycling performance due to due to its unique chain structure and inter- and/or intra-chain bonding with polysulfides. The as-prepared PPy@S/GA-VD electrode exhibits excellent rate and cycling capability, delivering a high capacity of 1167 and 409.1 mA h g^{-1} at 0.2 C and 5 C, respectively. At 0.5 C, it still can maintain a capacity of 698 mA h g^{-1} after 500 cycles with an ultra-slow decay rate of 0.03% per cycle. A very simple vapor phase deposition strategy was designed to moderate the shuttle effect and enhance the reaction kinetics of sulfur, which could shed light on the fabrication of long-life Li-S batteries in future.

CHAPTER 6 A LARGE-SCALE SYNTHESIZED LI_2S-POLYPYRROLE HYBRID AND POLYPYRROLE-TREATED SEPARATOR FOR LI-S BATTERIES

6.1 Introduction

Over the past few decades, the emerging applications of electric vehicles and grid energy-storage systems have raised an urgent demand for rechargeable batteries with high energy density.[215, 259] Although lithium ion batteries have been commercialized and applied into cell phones, portable computers, wearable devices *et al.*, the current energy density of lithium ion batteries with oxide-based cathode,[23, 260, 261] such as $LiFePO_3$, $LiCoO_2$ and $LiMn_2O_4$, is not sufficient for long distance driving EVs (*i.e.* > 300 km) and grid-scale energy storage.[36, 216, 262] The lithium-sulfur (Li-S) battery with low-cost and low toxic sulfur as cathode has drawn much attention in recent years due to its high theoretical specific capacity (1675 mAh g^{-1}) and energy density (2600 Wh kg^{-1}).[10, 22, 263] However, the practical application of Li-S batteries has been hampered by several inherent drawbacks,[15, 217, 227, 264, 265] such as, the poor electronic conductivity of S and Li_2S (the final discharge products), the dissolution of intermediate products (*i.e.* long-chain lithium polysulfides) into electrolyte and the large volume expansion (80%) of sulfur during discharge/charge process. All above-mentioned problems could result in low specific capacity and unstable cycling performance. In addition, the sulfur cathode should be paired with lithium metal anode to fabricate Li-S battery, which may cause fire or explosion safety concerns due to the formation of dendrites on lithium anode.

Compared with sulfur cathode, the fully lithiated Li_2S with a high specific capacity of 1166 mA h g^{-1} is a promising option for Li-S cathode material,[266, 267] which can paired with lithium-free anode (e.g., Si, Sn, C) to alleviate the safety issues.[164, 268, 269] Moreover, unlike sulfur undergoing volume expansion, Li_2S shrinks initially in the first delithiation process, which can empty spaces for subsequent volume expansion and maintain the mechanical stability of electrodes. In addition, Li_2S possess a high melting point (938 °C), providing the possibility of making some modification at high temperature.[270, 271] However, the Li_2S also faces the same drawbacks of poor electronic conductivity and dissolution of intermediate products into electrolyte, resulting in low utilization of active materials and fast capacity fading.[267] And Li_2S needs to be activated in the first charging process due to the high potential barrier because of phase nucleation of the two-phase reaction between Li_2S and polysulfides.[269, 272]

To solve these problems, tremendous efforts have been made, including combining Li_2S with various conductive materials,[14, 273-275] designing novel cell structures[166, 276] and adding additives in electrolyte.[176] Among them, conductive carbonaceous materials are widely used to encapsulate Li_2S to improve the conductivity of Li_2S and physically trap lithium polysulfides. However, the nonpolar carbon materials have low binding energy with polar polysulfides, resulting in inferior ability to trap and confine them during cycling.[74] Therefore, searching suitable conductive matrixes with the strong chemical interaction with Li_2S_n species is important to improve conductivity and suppress the shuttle effect. Polypyrrole (PPy), as a conducting polymer, is widely used as matrixes for Li-S batteries, which not only act as a conducting agent to improve the electronic conductivity of active materials, but also efficiently trapped polysulfides due to its unique chain structure and nitrogen atoms in PPy.[73, 149, 249, 250] Y. Cui's group reported a polypyrrole encapsulated Li_2S cathode material via in situ polymerization method,

which delivered a high discharge capacity of 785 mA h g^{-1} with stable cycling over 400 cycles due to the strong Li-N interaction between N atoms in PPy and Li_2S.[277] Meanwhile, inserting an interlayer between cathode and separator is also an effective way to improve the stability of cycling performance. Lee and his coworks present a graphene film directly coated onto a Li_2S cathode, which could fasten the lithium ion transportation and successfully mitigate the dissolution of polysulfides.[276] As results, the Li_2S cathode delivered an initial discharge capacities of 1029.21 mA h g^{-1}, and a good capacity retention of 75.3% over 300 cycles at 2C. Although excellent results have been achieved by many groups, the preparation processes of cathode are always very complicated, including either multistep reactions or/and high temperature calcination.[163, 273, 278] In addition, Li_2S is very sensitive to moisture and the complicated preparation processes must be operated in glovebox, which is highly cost and hamper its large-scale commercialization. Thus, a facile and up-scaled method is necessary to prepare advanced Li_2S cathode for Li-S batteries.

In this study, we prepare a Li_2S-polypyrrole (PPy) hybrid using a simple ball-milling method, which is cost-effective and easily to be scaled-up. By adjusting the ball-milling time, submicron-sized Li_2S would be obtained, which is uniformly dispersed in the PPy nanofibers framework. The small sized Li_2S could shorten lithium ion diffusion distance, resulting in fast kinetic reaction and high specific capacity. In addition, a PPy-coated separator was applied instead of a commercial separator. The PPy layer coated on the separator acts as a fishing net to capture dissolved polysulfides and mitigate the shuttle effect, which can enhance the cycling stability of Li-S batteries. Moreover, the PPy layer coated on the separator also acts as an upper current collector, which can reduce the effective resistance of Li_2S cathode and accelerate the kinetics of the electrochemical reactions. As a result, the cell with prepared Li_2S-PPy cathode and

PPy-coated separator delivers an initial discharge capacity of 885.5 mA h g^{-1} and retains a capacity of 529.7 mA h g^{-1} after 200 cycles at 0.2 C.

6.2 Experimental section

Synthesis of PPy nanofiber: PPy nanofiber was synthesized via an oxidative chemical polymerization method. The pyrrole was distilled before use. In a typical process, 0.72 g hexadecyl trimethyl ammonium bromide (CTAB) was dissolved in 200 mL of 1 M HCl aqueous solution. Then, 0.25 g sodium p-toluene sulfonate and 0.33 g distilled pyrrole were added into the above solution successively, and the solution was precooled in an ice bath (0-5 °C) maintained for 0.5 h under constant magnetic stirring. Meanwhile, 1.13 g ammonium persulfate was dissolved in 20 ml distilled water, which was then dropped into the pyrrole-containing solution. The whole solution was reacted for 12 h in an ice bath (0-5 °C) under magnetic stirring. After that, the black product was collected by vacuum filtration and washed with 1 M HCl and distilled water several times, followed by drying at 60 °C for 12 h in a vacuum oven. Finally, the obtained black powder was denoted as PPy nanofiber.

Synthesis of Li_2S-PPy composites: Because the Li_2S is very sensitive to moisture and air, the synthesis process and materials preparation were conducted in an argon atmosphere. Commercial Li_2S with prepared PPy nanofiber was firstly mixed at a ratio of 70:30, then put into ball milling jar in glovebox. The mixture was ball-milled with a rotating speed of 300 rpm for different time (i.e. 5h, 6h and 7h), with a 10:1 ball to Li_2S weight ratio. After that the prepared Li_2S-PPy hybrids were collected for further physical and electrochemical performance.

*Physical characterizations***:** For physical and morphological characterization of the composite, X-ray diffraction patterns (XRD, GBC MMA 017) were collected over a 2θ

range of 10° - 80° with a scan rate of 2° min^{-1}. The morphologies of the samples and corresponding element mapping images were examined by field emission scanning electron microscopy (JEOL: FESEM-7500).

Electrochemical measurements: For electrochemical performance evaluation of Li_2S-PPy composites, the 2032-coin cells were assembled in an argon filled glovebox with the level of H_2O and O_2 below 0.1 ppm. The Li_2S-PPy electrode was made by mixing 80 wt% Li_2S-PPy hybrid with 10 wt% carbon black and 10 wt% poly(vinylidene fluoride) (PVDF) binder in N-methyl-2-pyrrolidinone (NMP) solvent. Then the slurry was spread on the carbon paper with a diameter of 12 mm using a doctor blade. The PPy coated separator was prepared mixing 90% PPy nanofiber with 10% PVDF in NMP, then directly coated on the commercial separator using a doctor blade. The electrodes and PPy-separators were dried in a vacuum oven at 60 °C for overnight. The mass loading of the Li_2S in electrode and PPy nanofiber on separator was 2 and 0.3 mg cm^{-2}, respectively. The electrolyte was 1 M lithium bis(trifluoromethanesulfonyl)imide (LiTFSI) in 1,3-dioxolane (DOL)/1,2-dimethoxyethane (DME) (1:1 by volume) containing 0.1 M $LiNO_3$ as additive. The amount of electrolyte used in coin cell is 15 uL g^{-1} based on the Li_2S amount in electrodes.Electrochemical impedance spectroscopy (EIS) and cyclic voltammetry (CV) measurements were performed on a Biologic VMP 3 electrochemical workstation over a frequency range of 10 mHz to 100 kHz, and the scan rate was 0.1 mV s^{-1} within a 1.7 V to 2.8 V voltage window. The coin cell cycling performance and rate capability were carried out with a LAND battery test system at different C rate (1 C = 1675 mA g-1) within the voltage range of 1.7-2.8 V.

6.3 Results and discussion

6.3.1 Structure and morphology

Figure 6.1 shows X-ray diffraction (XRD) patterns of PPy nanofibers, commercial Li_2S and Li_2S-PPy hybrids with different ball milling time. A representative broad peak of polypyrrole was observed, indicating the amorphous structure of PPy nanofibers.[258] Compared with the commercial Li_2S patterns, all ball-milled Li_2S-PPy samples only show the typical diffraction peaks of Li_2S and no other impurity peaks were detected, which indicates that no chemical reaction had taken place during the ball milling process. Furthermore, the poor intensity of diffraction peaks after ball-milling was observed, confirming the smaller average particle size of the Li_2S powder and the successful coverage by PPy nanofibers after the ball milling.[275]

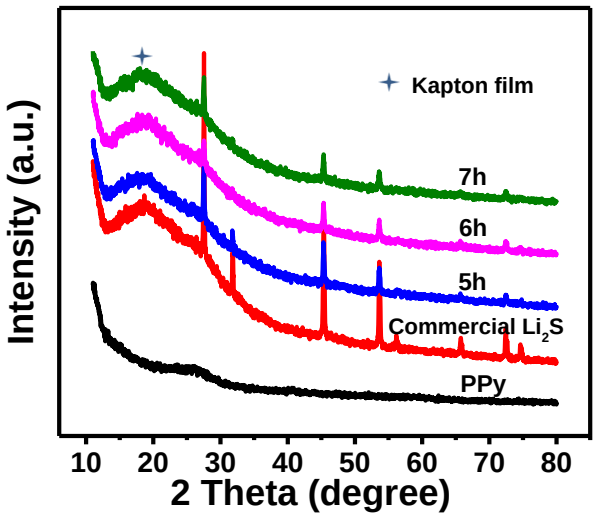

Figure 6.1. XRD patterns of PPy, commercial Li_2S and Li_2S-PPy composites with different ball milling time.

Field emission SEM (FESEM) micrographs of the Li_2S-PPy hybrids with different ball milling time along with commercial Li_2S material are presented in Figure 6.2, which

clearly shows the size change of Li_2S during the ball milling process. Compared with the commercial Li_2S (Figure 6.2a), the size of Li_2S in Li_2S-PPy-5h was dramatically reduced and the Li_2S with a micron size were uniformly dispersed into the PPy nanofibers matrix (Figure 6.2b). With increasing the ball-milling time, the Li_2S size in Li_2S-PPy-6h composites reduced to nanosized, which was firmly adhered to and covered by the PPy nanofibers, as shown in Figure 6.2c. This morphology will increase the contact area between Li_2S and PPy, which will not only improve the conductivity of Li_2S, but also enhance the interaction between PPy and polysulfides to suppress the shuttle effect. When the ball-milling time increased to 7h, the Li_2S agglomerated together and the PPy nanofibers was destroyed to short length, shown in Figure 6.2d, which could result in poor conductivity and decrease the utilization of active materials. From the SEM images, the Li_2S-PPy-6h composites were expected to show better electrochemical performance than other two samples.

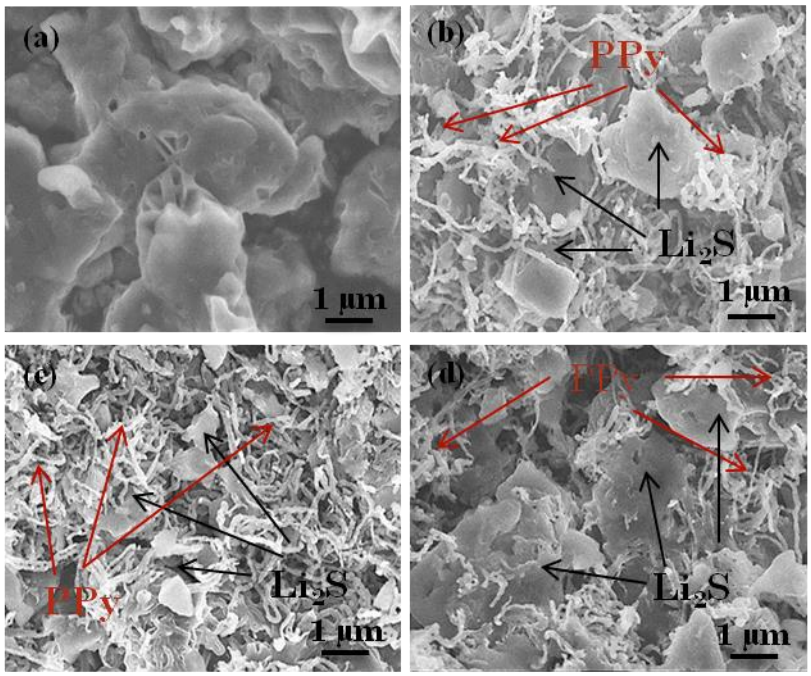

Figure 6.2. The FESEM images of (a) commercial Li_2S, (b) Li_2S-PPy-5h, (c) Li_2S-PPy-6h and (d) Li_2S-PPy-7h composites.

To value the electrochemical performance of Li_2S-PPy composites, a 3D carbon paper was applied as current collector in our study. Figure 6.3a and b show the top-view and side-view SEM images of carbon paper, which possesses 3D microporous layered network structure. It is suitable to load more active materials than the normal 2D Al foil current collector. Figure 6.3 c and d shows the top-view and side-view SEM images of Li_2S-PPy-6h cathode, which revealed that the active materials were successfully penetrated into each layer of carbon framework and the pores of carbon paper were filled by Li_2S-PPy composites. As a result, a large amount of active materials (~ 3 mg cm^{-2}) was loaded in each cathode, which is much higher than most reported works using Al foil as current collector.[279-281]

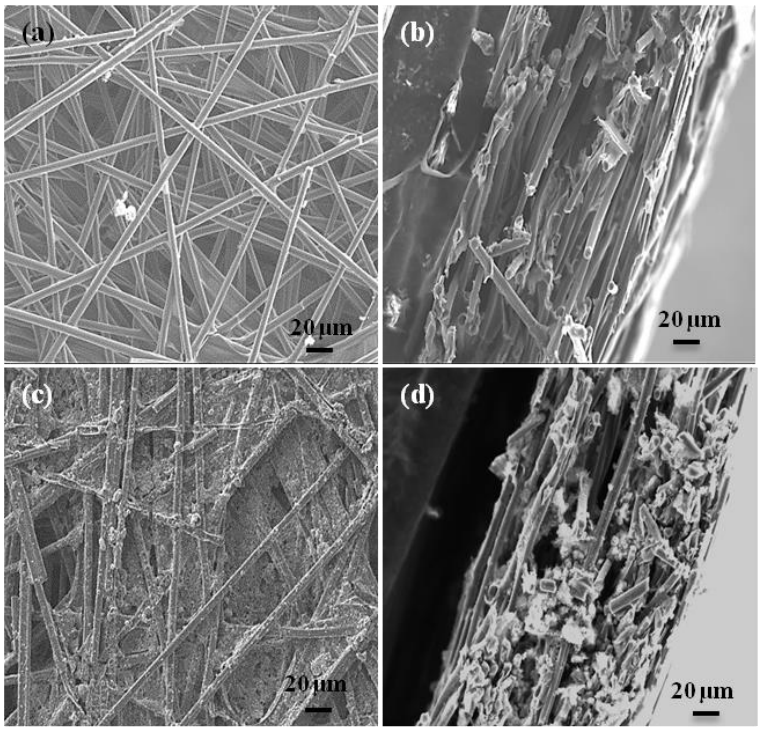

Figure 6.3. FESEM image of (a) top view and (b) side view of carbon paper; FESEM image of (a) top view and (b) side view of Li_2S-PPy-6h cathode.

6.3.2 Electrochemical characterizations

To measure the electrochemical performance of Li_2S-PPy composites, the Li_2S-PPy cathode was firstly activated to overcome the potential barrier of Li_2S at the first cycles by applying a high cut-off voltage.[269] Figure 6.4a shows the first charge-discharge profile of the activation process for Li_2S-PPy-6h at a current density of 0.05 C. At the beginning of charging profiles, the voltage was rapidly increased to 2.7 V and then decreased followed by gradually increasing to 4V. The initial rapidly increasement of voltage is known as the initial potential barrier of Li_2S.[282] The activation charge-discharge profiles of Li_2S-PPy-5h and Li_2S-PPy-7h composites were also shown in Figure 6.5. The potential barrier of Li_2S-PPy-6h composites is much smaller than that of the reminding two samples, which can be ascribed to the small size of Li_2S and the firm contact between Li_2S particles and conductive PPy nanofibers.

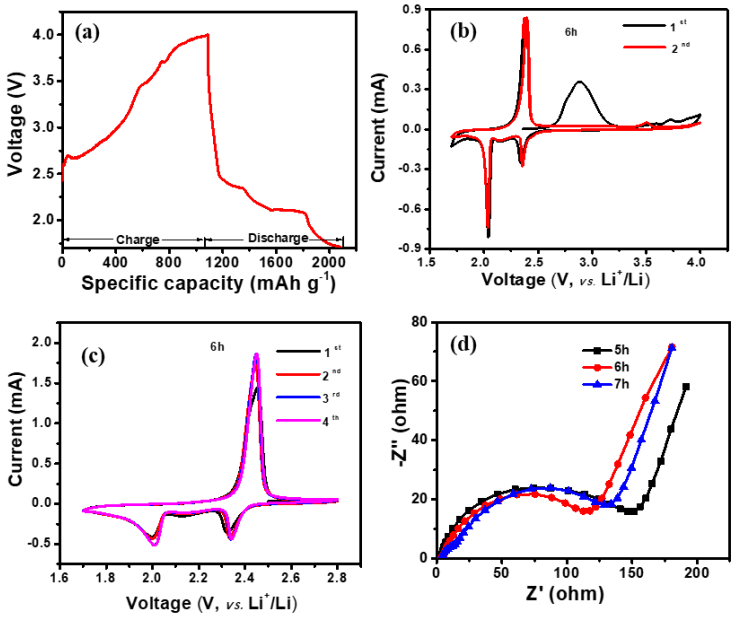

Figure 6.4. (a) Charge-discharge profile of first cycle for activation of Li_2S-PPy-6h; CV profiles of Li_2S-PPy-6h (b) the first two cycles at 0.05 mV s^{-1}, (c) the subsequent CV

profiles after activation at 0.1 mV s^{-1}, (d) electrochemical impedance spectra (EIS) of Li_2S-PPy composite with different time.

Figure 6.4b shows the CV curves of Li_2S-PPy-6h composites at a current density of 0.05 mV s^{-1}. In the initial sweep, an oxidation peak at ~2.85 V was observed, which is related to the potential barrier needed to be overcome to activate Li_2S. The Li_2S-PPy-7h, Li_2S-PPy-5h and pure Li_2S cathodes also show a high oxidation peak in the first charging process, as shown in Figure 6.6 a, c and e, which loaded at 3.0 V, 3.1 V and 3.8 V, respectively. These results indicate that the potential barrier of Li_2S-PPy-6h is a little bit lower than that of Li_2S-PPy-7h and Li_2S-PPy-5h composites and much lower than that of pure Li_2S, which is certified that the small size of Li_2S and the uniform coverage of PPy will reduce the energy barrier related to the phase nucleation of polysulfides.[269, 283] After the first scanning to 4 V, the potential barrier disappears in the next cycling, indicating the Li_2S was successfully activated in the first cycle and no need to be activated in the following cycles.

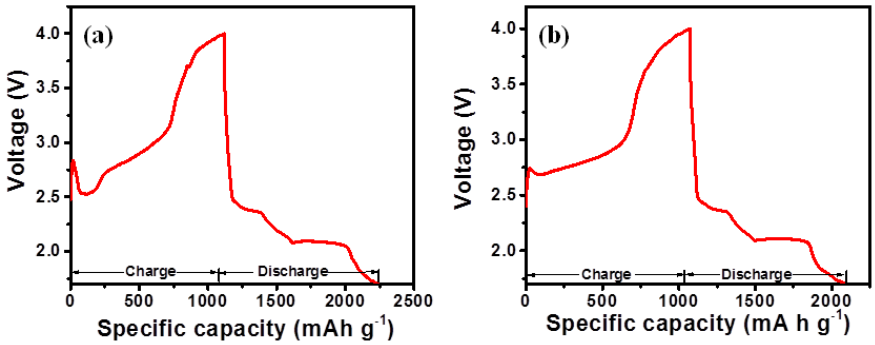

Figure 6.5. The Charge-discharge profile of first cycle for activation of Li_2S-PPy composite: (a) 7h and (b) 5h.

After activation, the CV profiles of Li_2S-PPy and pure Li_2S cathodes at a scanning rate of 0.1 mV s^{-1} are shown in Figure 6.4c and Figure 6.6. All electrodes show two typical

cathodic peaks and one anodic peak. The first cathodic peak located at about 2.3 V represents the reduction of sulfur to soluble long-chain polysulfides (Li_2S_n, $2 < n \leq 8$), and the second cathodic peak at ~2.0 V is due to the further reduction of soluble polysufides to lithium sulfides (Li_2S_2/Li_2S). At around 2.5 V, the anodic peak reveals the conversion from lithium sulfides to lithium polysulfides, and finally to sulfur.[195] However, the CV profiles of the Li_2S-PPy-6h display a higher current in the redox process compared with that of remining electrodes, indicating the fast electron transfer and quick reaction kinetics in Li_2S-PPy-6h composites.[284] Electrochemical impedance spectroscopy (EIS) measurements were conducted to characterize the internal resistance and charge-transfer process. The Nyquist plots of the Li_2S-PPy composites with different ball milling time before cycling are shown in Figure 6.4d, which are both composed of a depressed semicircle from the high frequency region to the mid-frequency region and an inclined line in the low frequency region, which are ascribed to the charge-transfer resistance (R_{ct}) and the mass-transfer process, respectively.[285] The EIS results indicate that Li_2S-PPy-6h cathode exhibits the lowest charge transfer resistance, which can be contributed to uniform dispersion of small size Li_2S in the PPy nanofibers matrixes.

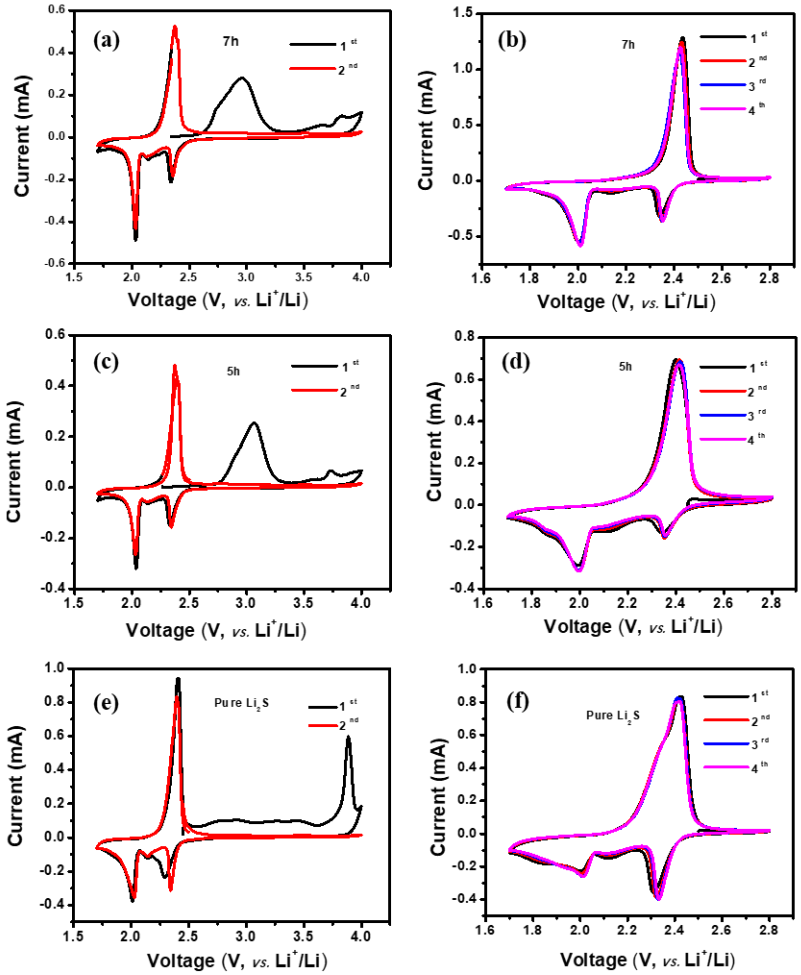

Figure 6.6. The first and second CV profiles of Li_2S-PPy composites with (a) 7h, (b) 5h and (c) pure Li_2S composites at a scan rate of 0.05 mV s^{-1}; The subsequent CV profiles of Li_2S-PPy composites with (a) 7h, (b) 5h and (c) pure Li_2S composites at a scan rate of 0.1 mV s^{-1}.

Figure 6.7a shows typical charge-discharge profiles for the Li_2S-PPy hybrids and pure Li_2S cathodes at 0.1 C. All the samples show two discharge plateaus, the one at~2.37 V corresponding to the lithiation of sulfur to long-chain lithium polysulfides, and the flat one at ~ 2.05 V corresponding to the further reduction of the long-chain polysulfides to Li_2S_2 or Li_2S. In the charging process, one plateau was observed, relating to the reversible reaction from Li_2S to sulfur, which is consistent with the CV results. In comparison, the Li_2S-PPy-6h show a higher reduction potential and a lower oxidation

potential with lower polarization than other samples, which suggests a kinetically efficient reaction process with a small barrier due to the good contact between PPy with smaller Li_2S particles.[208] The rate capability of the Li_2S-PPy hybrids is shown in Figure 6.7b. The Li_2S-PPy-6h hybrid shows the highest capacities at all current density, delivering a specific capacity of 791.7, 673.1, 570.3, 481.5 and 359.7 mA h g^{-1} at 0.1 C, 0.2 C, 0.5 C, 1 C and 2 C, respectively. When the current density was suddenly recovered back to 0.1 C, a capacity of 670 mA h g^{-1} is still obtained. In comparison, the Li_2S-PPy-5h hybrid only delivered a capacity of 160.8 mA h g^{-1} at 2 C. The Li_2S-PPy-7h hybrid shows capacities of 606.3, 495, 414.9, 355.6 and 277.2 mA h g^{-1} at 0.1 C, 0.2 C, 0.5 C, 1 C and 2 C, respectively, which is all lower than that of the Li_2S-PPy-6h hybrid. The cycling performance and the coulombic efficiency of the Li_2S-PPy hybrids and pure Li_2S composites at 0.1 C are shown in Figure 6.7c. The Li_2S-PPy-6h delivered an initial capacity of 797.8 mA h g^{-1} and maintained 384.6 mA h g^{-1} after 200 cycles with a capacity retention of 48.2%. However, the capacity after 200 cycles were only 289.4, 204.4 and 164.5 mA h g^{-1} for Li_2S-PPy-7h, Li_2S-PPy-5h and pure Li_2S electrodes, which is much lower than that of Li_2S-PPy-6h composites. In addition, the coulombic efficiencies of pure Li_2S electrode (less than 95%) is lower than that of Li_2S-PPy hybrids (~100%), which is supposed to the continuous polysulfides dissolution into electrolyte during cycling. These results indicate that the PPy nanofiber could effectively trap the dissolved polysulifdes, improving the utilization of active materials and mitigating the shuttle effect.

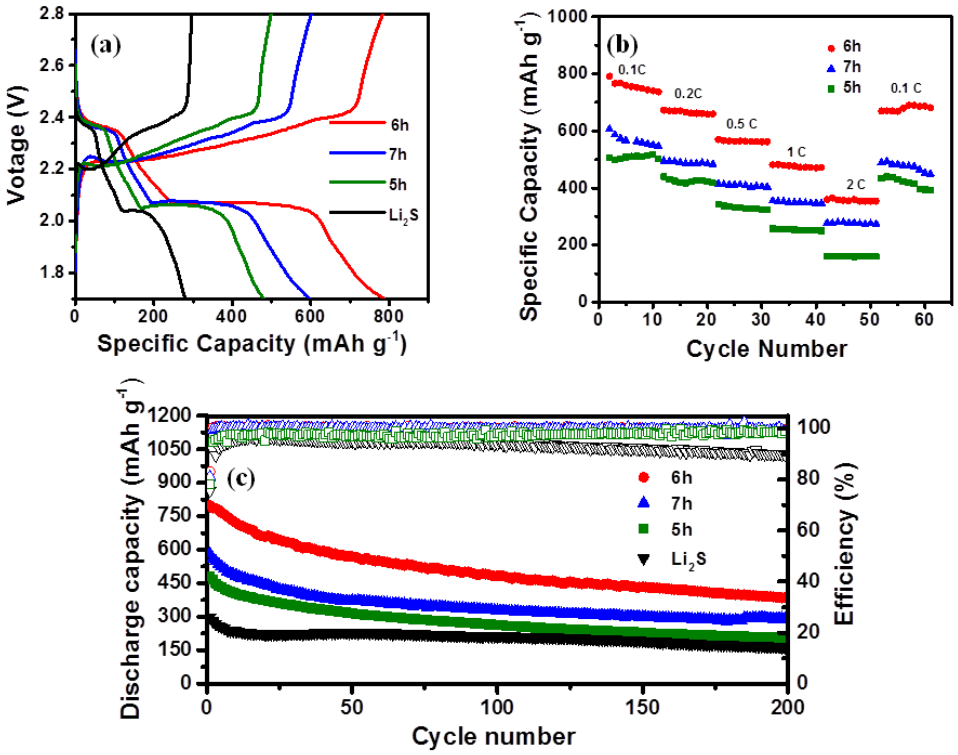

Figure 6.7. (a) Charge-discharge profiles, (b) rate capability and (c) cycling performance at 0.1 of Li_2S-PPy composites with different ball milling time.

In order to further improve the cycling stability of Li_2S-PPy-6h composites, a PPy nanofiber coated separator (PPy-separator) was applied instead of a normal commercial separator in our following experiments. The PPy-separator was prepared by directly coating the PPy nanofiber slurry on commercial separator via a simple doctor blade method, which is simple and cost-effective. Most importantly, the PPy layer on the separator can act as fishing net, effectively blocking the dissolved polysulfides within the cathode side, due to the strong Li-N interaction between N atoms in PPy and lithium polysulfides. To understand the impact of the PPy-separator on the electrochemical performance of Li_2S-PPy-6h cathode, EIS measurements was performed on Li-S batteries consisting of Li_2S-PPy-6h cathode with PPy-separator and with normal separator before cycling, as shown in Figure 6.8a. After coating PPy layer on the

commercial separator, the charge transfer resistances of the Li-S batteries dramatically decrease. Because the PPy layer acting as an upper current collector can keep tight contact between active material and separator on the nanoscale to reduce the contact resistances and accelerate the kinetics of the electrochemical reactions.[126] Figure 6.8b shows the cycling performance of Li_2S-PPy-6h cathode with PPy-separator and with normal separator at 0.1 C. Compared with the Li-S batteries with normal separator, the Li-S batteries with the PPy-separator shows a higher specific capacity and more stable cycling performance, indicating that the PPy layers between the cathode and the separator can effectively capture polysulfides and improve utilization of Li_2S. The initial discharge capacity of the Li-S battery with PPy-separator is 885.5 mA h g^{-1}, which still maintains at 529.7 mA h g^{-1} after 200 cycles, with a capacity retention rate of about 59.8%, much higher than that of cells with normal separator (48.2%). The high capacity and stable cycling performance is contributed to the PPy layer between cathode and separator, which can not only reduce the charge transfer resistance, but also trap the polysulfide to improve the active materials utilization and suppress their dissolution.

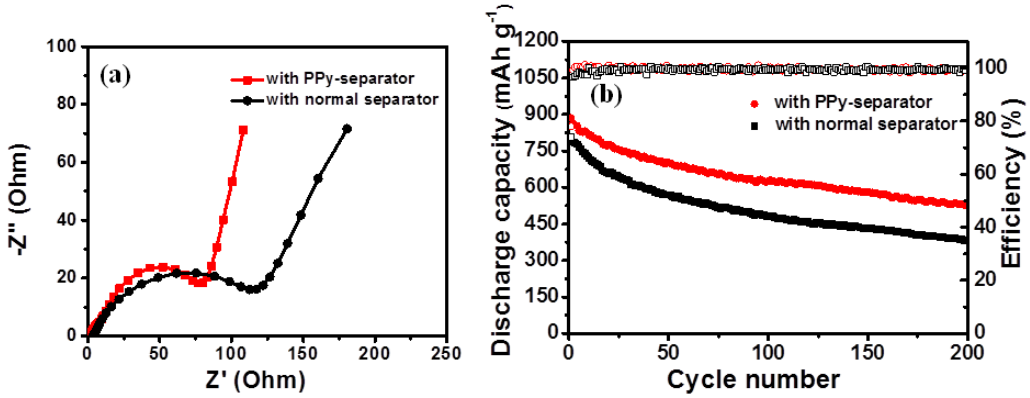

Figure 6.8. (a) Electrochemical impedance spectra (EIS) and (b) cycling performance at 0.1 C of Li-S cells with Li_2S-PPy-6h cathode and PPy-coated separator or normal separator.

6.4 Conclusions

A facile and up-scaled ball milling method was reported to prepare Li_2S-PPy hybrids. By adjusting the ball milling time, the Li_2S-PPy composites with 6h ball milling time show the best electrochemical performance. Because the Li_2S-PPy-6h composites display the smallest Li_2S size, and the smaller Li_2S particles were uniformly distributed in the PPy nanofiber matrixes, which could improve the tight contact between conductive agent and active materials. The PPy nanofibers matrix could not only improve the conductivity of Li_2S, but also trap polysulfides to reduce the dissolution due to the strong chemical bonding between PPy and ploysulifdes. In addition, a 3D carbon paper was used as current collector instead of 2D Al foil current collector, which could increase the loading amount of active materials. For further improving the cycling stability, a PPy-coated separator was prepared by directly coating PPy nanofiber slurry on the commercial separator, which is simple and cost-effective. After using the PPy-separator, the specific capacity and cycling performance of Li-S cell both enhanced, delivering an initial capacity of 885.5 mA h g^{-1} at 0.1 C, which still maintained at 529.7 mA h g^{-1} after 200 cycles with a capacity retention rate of about 59.8%, which is higher than that (48.2%) of Li-S cell with normal commercial separator. The excellent cycling stability can be ascribed to PPy layer between cathode and separator, which is acted as fishing net to capture dissolved polysulfides and improve their reuse. This work is hopefully helpful to prepared large-scaled submicrosized Li_2S composites as a high-performed Li-S cathode material with high active material loading amount.

CHAPTER 7 A CONDUCTIVE POLYMER DERIVED N-DOPED CARBON NANOFIBERS SUPPORTED LI_2S COATING LAYER FOR LI-S BATTERIES WITH HIGH MASS LOADING

7.1 Introduction

In recent years, lithium-sulfur (Li-S) batteries have been attracted much attention due to their high theoretical capacity (1675 mAh g^{-1}) and energy density (2600 Wh kg^{-1}) as well as the abundance and low cost of sulfur cathode materials.[10, 286-288] However, the practical application of Li-S batteries was hindered by their innate defects, such as the insulating nature of sulfur and its discharge product (Li_2S), the shuttle effect of polysulfides during cycling and the volume expansion (80%) of sulfur during discharge process, which lead to low utilization of active materials and fast capacity fading.[14, 289, 290] In addition, the sulfur cathode should be paired with metal lithium anode, which could cause safety concerns. Compared with sulfur, lithium sulfide (Li_2S) can be paired with lithium-free anode,[164, 291] such as silicon, tin, carbon et. al, relieving the safety problems related to lithium anode. Moreover, the Li_2S firstly undergoes volume shrink in the initial charge process,[292-294] which could release some voids to buffer the volume expansion, rendering the structure integrity of cathode materials during cycling.

Like S cathode, the Li_2S also faces many difficulties during its commercialization process,[163, 269, 295] such as the poor conductivity and the dissolution of polysulfides, leading to low capacity and poor cycling stability. Besides, there is an activation energy barrier needed to be overcome in the initial charge process of Li_2S cathode.[163] To deal with these obstacles, electrolyte modification including exploring solid-state electrolyte,[296-298] adding additives[299-301] (lithium nitrate, lithium iodide, transition-metal

salts, etc.) have successfully relieved the shuttle effect and improved the cycling stability of Li_2S cathode. In addition, great efforts have been made to synthesize nanosized Li_2S,[174, 302-304] because the nanosized Li_2S usually possess a smaller activation energy barrier and higher conductivity with higher specific capacity than the commercial Li_2S.[275]

At present, there are two commonly used methods to synthesize Li_2S nanoparticle due to moisture sensitivity and reactivity of Li_2S. One method is to ball-mill commercially available large particles of Li_2S with conductive additives; another method is to react Li_2SO_4 with carbon precursor at high-temperature (~ 900 °C). Although, the synthesized Li_2S-C composites were also show promising electrochemical performance, these methods both show their own drawbacks: the ball-milled method directly used commercial Li_2S particles combined with conductive agent, which is expensive for the large-scale commercialization of Li_2S cathode; the high-temperature method required complicated facilities and procedures, which is not possible to fulfil large-scaled production. In addition, the solid-state reduction methods usually are hard to achieve uniform Li_2S particle distribution on conductive agents. Given all these considerations, solution-based synthetic methods usually could obtain small size and uniform particle distribution compared with the above-mentioned methods. For example, Li_2S spheres with a uniform size of 0.5 um can be synthesized by the solution-based chemical lithiation of S;[278] some other advanced Li_2S-carbon composites including CNT-Li_2S, graphene-Li_2S and C-Li_2S have been obtained by the simple infiltration of Li_2S-ethanol solutions,[305, 306] which were all shown uniform distribution of Li_2S nanoparticles in these composites. Therefore, it is necessary to find a facile method to synthesize nanosized Li_2S and realize the uniform distribution of Li_2S on conductive matrixes at the same time.

In order to enhance the cycling stability of Li_2S cathode, the Li_2S nanoparticles should be combined with conductive matrix (e.g. carbonaceous materials, polymer or metal-based materials) to physically or chemically trap polysulfides.[277, 307-312] Among them, heteroatom-doped carbon materials have been attracted much attention due to the strong chemical bonding between heteroatom-functional group with polysulfides to trap dissolved polysulfides. For example, Yu's group designed a nitrogen and phosphorus codoped carbon framework to support Li_2S nanoparticles for Li-S batteries.[174] The results indicated that the heteroatom doping can suppress the shuttle effect through strong interaction between heteroatoms and polysulfides, resulting in stable cycling performance. Meanwhile, heteroatom doping in the carbon framework plays an important role in improving the reaction kinetics, as it may help catalyse the redox reactions of sulfur species to reduce electrochemical polarization and enhance the ionic conductivity of Li_2S. Therefore, using chemical adsorbents to trap dissolved polysulfides is essential to obtain advanced Li_2S cathode.

In this paper, we design a facile and solution-based synthetic method to prepare Li_2S nanoparticles coated N-doped carbon nanofiber derived from polypyrrole. Due to the solution-based procedures, the Li_2S layer was uniformly coated on the carbon framework without any aggregation. The small sized Li_2S possesses a relatively lower activation barriers and could shorten lithium ion diffusion distance, resulting in fast kinetic reaction and high specific capacity. In addition, the N-doped carbon nanofiber as matrixes could chemically trap dissolved polysulfide and improve the utilization of active materials due to the strong interaction between N atom and Li atom in lithium polysulfides. Moreover, high mass loading electrode (~ 3 mg cm^{-2}) with high capacity and long cycle life were also obtained to satisfy the requirements of commercial

batteries, which delivers an initial discharge capacity of 705.5 mA h g^{-1} and retains a capacity of 479.3 mA h g^{-1} after 200 cycles at 0.2 C.

7.2 Experimental section

Synthesis of N-doped carbon (N-C) nanofibers: The nitrogen doped carbon nanofibers were derived from polypyrrole nanofibers. The PPy nanofibers was synthesized *via* an oxidative chemical polymerization method, which was elaborated by our previous paper.[249] For the synthesis of N-doped carbon nanofibers, the prepared PPy nanofibers were heated at 600 °C for 2 h under Ar atmosphere with a heating rate of 5 °C min^{-1}.

Synthesis of sulfur coated N-C nanofibers (S@N-C): 15 mg N-doped carbon nanofiber was added into 1 mL toluene solution containing 30 mg sulfur at 60 °C, and then the raw S/N-C nanofiber was obtained after evaporating the toluene at 80 °C for 10 hours. To realize the uniform dispersion of S on N-C nanofibers, the raw S/N-C nanofiber were sealed in an autoclave and heated at 155 ºC for 10 h.

Synthesis of lithium sulfide coated N-C nanofibers (Li_2S@N-C): 50 mg obtained S@N-C nanofibers and a certain amount of n-Butyllithium was put into a small vial with a cap and then heated to 110 °C for 4 h. After the reaction, the cap was taken off to degas the excessive n-Butyllithium. After that, the obtained black powders were recorded as Li_2S coated N-C nanofibers (Li_2S@N-C). Since the Li_2S was very sensitive to moisture, the whole process was conducted in an argon filled glovebox with the levels of H_2O and O_2 both < 0.1 ppm.

Physical Characterizations： For physical and morphological characterization of the composite, X-ray diffraction patterns (XRD, GBC MMA 017) were collected over a 2θ range of 10° - 80° with a scan rate of 2° min^{-1}. The morphologies of the samples and

corresponding element mapping images were examined by field emission scanning electron microscopy (JEOL: FESEM-7500) and transmission electron microscopy (TEM, JEM-2100UHR, JEOL). Thermogravimetric analysis (TGA) was performed in air using a SETARAM instrument to estimate the amount of sulfur in the sample.

Electrochemical measurements： For electrochemical performance evaluation of Li_2S@N-C composites, the 2032-coin cells were assembled in an argon filled glovebox with the level of H_2O and O_2 below 0.1 ppm. The Li_2S@N-C electrode was made by mixing 80 wt% Li_2S@N-C hybrid with 10 wt% carbon black and 10 wt% poly(vinylidene fluoride) (PVDF) binder in N-methyl-2-pyrrolidinone (NMP) solvent. Then the slurry was spread on the Al foil with a diameter of 12 mm using a doctor blade. Then, the electrodes were dried in a vacuum oven at 60 °C for overnight. The mass loading of the Li_2S on electrode could be adjusted from 1 to 3 mg cm^{-2}. The electrolyte was 1 M lithium bis(trifluoromethanesulfonyl)imide (LiTFSI) in 1,3-dioxolane (DOL)/1,2-dimethoxyethane (DME) (1:1 by volume) containing 0.1 M $LiNO_3$ as additive. The amount of electrolyte used in coin cell is 15 uL g^{-1} based on the Li_2S amount in electrodes. Electrochemical impedance spectroscopy (EIS) and cyclic voltammetry (CV) measurements were performed on a Biologic VMP3 electrochemical workstation over a frequency range of 10 mHz to 100 kHz, and the scan rate was 0.1 mV s^{-1} within a 1.7 V to 2.8 V voltage window. The coin cell cycling performance and rate capability were carried out with a LAND battery test system at different C rate (1 C = 1675 mA g^{-1}) within the voltage range of 1.7-2.8 V.

7.3 Results and discussion

7.3.1 Structure and morphology

The preparation process for the Li_2S@N-C nanofibers is illustrated in Figure 7.1. First, PPy nanofibers were prepared via a polymerization method.[249] Then, the N-doped carbon nanofibers was obtained by a thermal treatment of PPy nanofibers at 600 °C for 2 h. After that, the sulfur layer was coated on the N-doped carbon nanofibers by a simple evaporation of S-toluene solution followed by vacuum redistribution. Finally, the S@N-C nanofiber was lithiated by n-Butyllithium at 110 °C for 4 h in a glovebox to obtain Li_2S@N-C nanofibers.

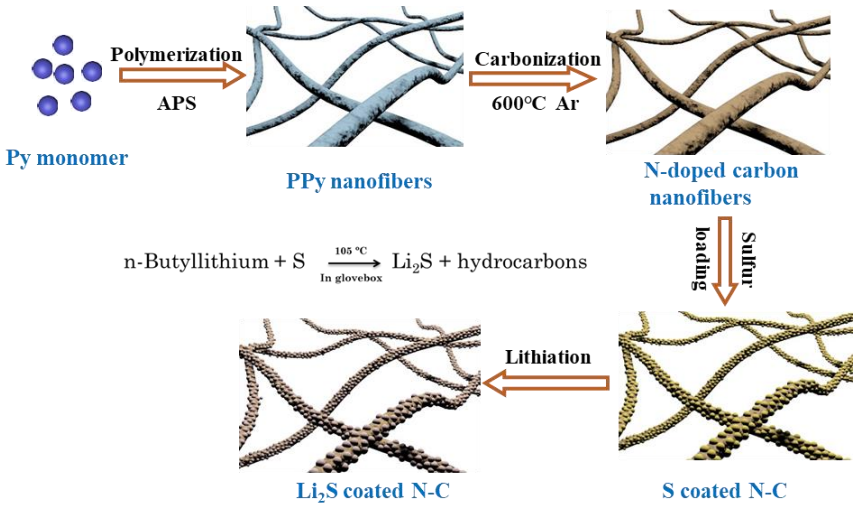

Figure 7.1. Schematic for the fabrication of the Li_2S@N-C nanofibers

The morphologies of the prepared materials were investigated by the Field Emission Scanning Electron Microscope (FESEM) micrographs. Figure 7.2a shows the SEM images of prepared PPy nanofibers with a homogeneous diameter of 100 nm. After the thermal treatment, the N-doped carbon nanofibers preserves the original morphology of PPy nanofibers, but the surface of N-doped carbon nanofibers become rougher due to the release of gas during high temperature (Figure 7.2b), which can increase the surface

area and make the deposition of sulfur feasible. After the sulfur coating, the S@N-C nanofiber composite keeps the nanofiber morphology and the surface becomes relatively smooth, indicating the successful loading of sulfur layer on the N-C nanofiber (Figure 7.2c). Figure 7.2d shows the SEM images of the Li_2S@N-C nanofibers, which show the same morphology with that of S@N-C nanofibers, and there is no obvious agglomeration of nanoparticles, indicating the uniform distribution of Li_2S on the surface of N-C nanofibers. Transmission electron microscopy (TEM) was further used to investigate the structure of Li_2S@N-C nanofibers. As shown in Figure 7.2e, Li_2S@N-C nanofibers maintain the fibrous structure of S@N-C nanofibers, which is consistent with the SEM image in Figure 7.2d. The HRTEM reveals that Li_2S nanoparticles with a particle size less than 5 nm are tightly embedded in the N-doped porous carbon matrixes. The corresponding elemental maps of carbon, nitrogen, and sulfur in Figure 7.2g further confirm the homogeneous distribution of elements in the Li_2S@N-C nanofibers, indicating the uniform distribution of Li_2S on N-C nanofibers.

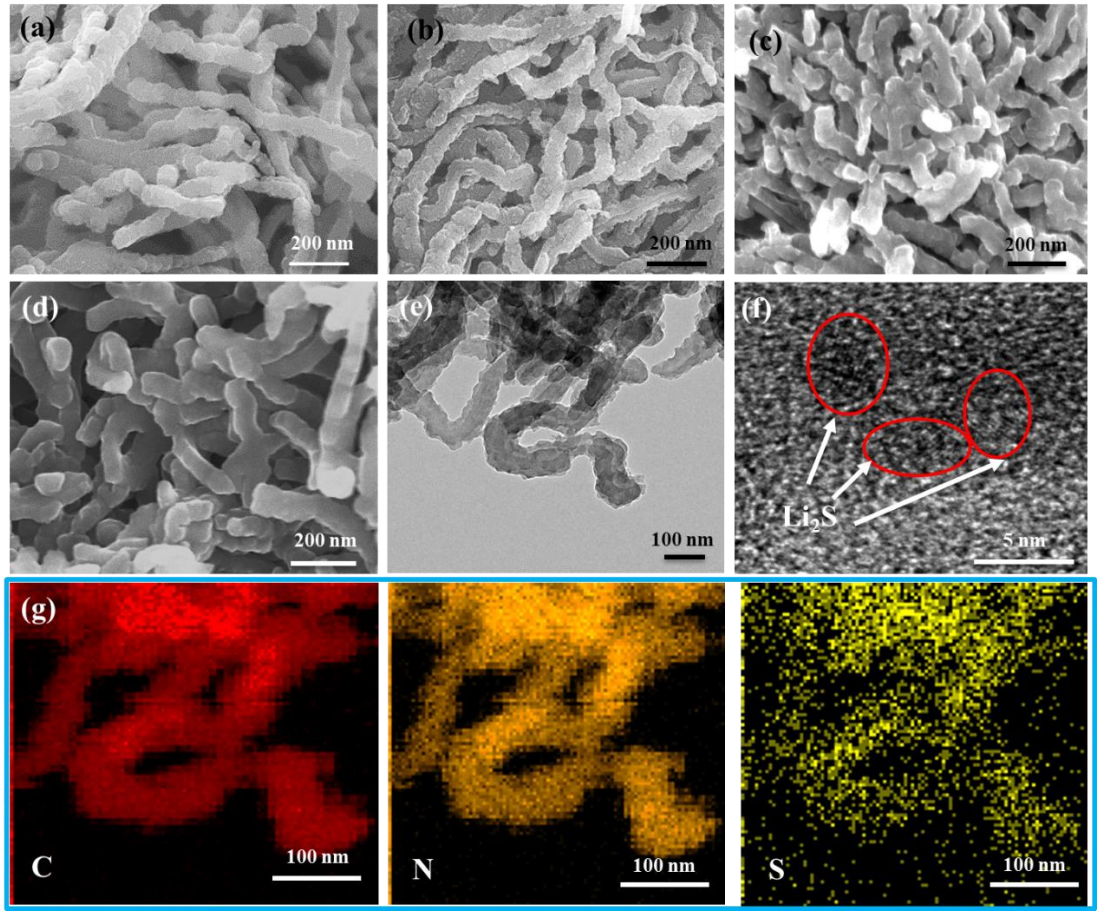

Figure 7.2. SEM images of (a) PPy nanofibers, (b) N-doped carbon nanofibers, (c) Li_2S@N-C nanofibers and (d) Li_2S@N-C nanofibers, (e) TEM and (f) HRTEM images of Li_2S@N-C nanofibers and (g) corresponding element mapping.

The crystalline structures of the prepared samples were confirmed by X-ray diffraction (XRD) patterns, as shown in Figure 7.3a. The N-doped carbon nanofibers only show a broad peak between 20-30°, indicating its amorphous structure. And the pronounced peaks in the S@N-C sample can be indexed to the orthorhombic sulfur (JCPDS card No: 08-0427) with high crystallinity. After reaction with n-Butyllithium, sulfur is converted into cubic phase of Li_2S (JCPDS card No. 77-2145) without other crystal impurity and no sulfur residual, indicating the completely conversion from sulfur to Li_2S. Raman spectroscopy was applied to further characterize the successful synthesis of Li_2S in the

composites, as shown in Figure 7.3b. We see that the Raman spectrum of pristine Li_2S shows the characteristic T2g phonon mode of Li_2S at 372 cm^{-1} corresponding to Li-S bond vibrations.[277, 313] Two typical graphitic peaks are clearly observed from the N-doped carbon nanofibers at around 1355 cm^{-1} and 1597 cm^{-1}, corresponding to the D band and the G band, respectively.[314] The Raman spectrum of the Li_2S@N-C nanofibers shows both the catachrestic peaks of Li_2S and N-doped carbon, indicating the successful loading Li_2S on the surface of N-doped carbon nanofibers, which is consistent with the element mapping results in Figure 7.2g. Thermogravimetric analysis (TGA) was performed under pure argon atmospheres to determine the content of sulfur in the S@N-C composites. Because the Li_2S was obtained from the lithiation of sulfur, the content of Li_2S in the Li_2S@N-C nanofibers can be calculated from the content of sulfur. As shown in Figure 7.3c, the content of sulfur in S@N-C composites is 64%, which means the content of Li_2S in the Li_2S@N-C composites is 68%.

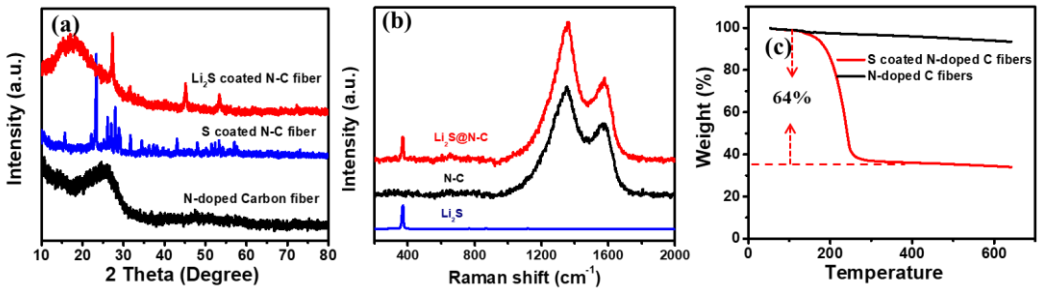

Figure 7.3. (a) the XRD patterns of prepared N-doped carbon nanofibers, S@N-C nanofibers and Li_2S@N-C nanofibers; (b) Raman spectra of commercial Li_2S, N-doped carbon nanofibers and Li_2S@N-C nanofibers; (c) TGA curves of N-doped carbon nanofibers, S@N-C nanofibers.

7.3.2 Electrochemical characterization

The electrochemical performance of prepared Li_2S@N-C composites and commercial Li_2S was first investigated by the cyclic voltammetry (CV) measurements, as shown in Figure 7.4a and b. Due to the energy barrier in the first charging process, the electrodes were first activated using a high cut-off voltage of 4V.[269] From the Figure 7.4a and b, the Li_2S@N-C and pure Li_2S electrodes both show one typical anodic peak and two typical cathodic peaks. The first cathodic peak located at about 2.3 V represents the reduction of sulfur to soluble long-chain polysulfides (Li_2S_n, $2 < n \leqslant 8$), and the second cathodic peak at ~2.0 V is due to the further reduction of soluble polysufides to lithium sulfides (Li_2S_2/Li_2S). At around 2.5 V, the anodic peak reveals the conversion from lithium sulfides to lithium polysulfides, and finally to sulfur.[195] However, the Li_2S@N-C electrode shows a small oxidation peak at ~3.5 V in the first charging process, which is related to the potential barrier needed to activate Li_2S cathode. The pure Li_2S electrode also shows a broad oxidation peak loaded at 3.7 V in the first charging process, as shown in Figure 7.4b, which is much large than that of Li_2S@N-C electrode. These results indicate that the potential barrier of Li_2S@N-C electrode is a little bit lower than that of pure Li_2S electrode, which can be ascribed to the small size of Li_2S coated on the N-doped carbon nanofibers and the uniform distribution of Li_2S on the carbon nanofibers.[269, 283] After the first activation, these electrodes both can normally work in the following cycles just like sulfur cathode, which means that the Li_2S electrode was successfully activated by the high cut-off voltage.

The charge-discharge profiles are also shown in Figure 7.4c and d. For the Li_2S@N-C electrode, the cut-off voltage was set as 3.6V, while for the pure Li_2S electrode, the cut-off voltage was set as 4V. As we can see, in the first charging process, the voltage

was rapidly increased and then decreased followed by gradually increasing to the cut-off voltage. The initial rapidly increasement of voltage is known as the initial potential barrier of Li_2S.[282] The potential barrier of Li_2S@N-C electrode is a little bit smaller than that of pure Li_2S electrode, which is consistent with the results of CV measurements. After activation, the charge-discharge profiles of Li_2S@N-C and pure Li_2S electrode both show two discharge plateaus, the one at~2.3 V corresponding to the lithiation of sulfur to long-chain lithium polysulfides, and the flat one at ~ 2.05 V corresponding to the further reduction of the long-chain polysulfides to Li_2S_2 or Li_2S. In the charging process, one plateau was observed, relating to the reversible reaction from Li_2S to sulfur, which is consistent with the CV results. These results indicate that a cut-off voltage of 3.6 V is enough for Li_2S@N-C electrode to active Li_2S, which can be ascribed to small size and uniform distribution of prepared Li_2S.

The cycling performance of Li_2S@N-C and pure Li_2S electrode with a mass loading of 1 mg cm^{-2} is also compared in the Figure 7.6a. The electrode was first performed for 10 cycles at 0.1 C in order to fully active the Li_2S cathode, then cycled at 0.2 C. The Li_2S@N-C electrode delivers a much higher specific capacity than that of pure Li_2S electrode. The pure Li_2S electrode shows dramatic capacity fading in the first 20 cycles, delivering a discharge capacity of 1017.3 mA h g^{-1} in the first cycle at 0.1 C and decreasing to 550.5 mA h g^{-1} after 20 cycles at 0.2 C. Compared to pure Li_2S electrode, the Li_2S@N-C electrode shows relatively stable cycling performance with an initial specific capacity of 1036.6 mA h g^{-1} at 0.1 C, and a high capacity of 704.2 mA h g^{-1} is still maintained after 200 cycles. From the above results, the cycling stability of Li_2S@N-C electrode is significantly improved compared with the pure Li_2S electrode, suggesting that the N-doped carbon nanofibers could efficiently adsorb lithium

polysulfides, mitigate the shuttle effect of active materials. In addition, the small size and uniform distribution of prepared Li_2S could improve the utilization of Li_2S.

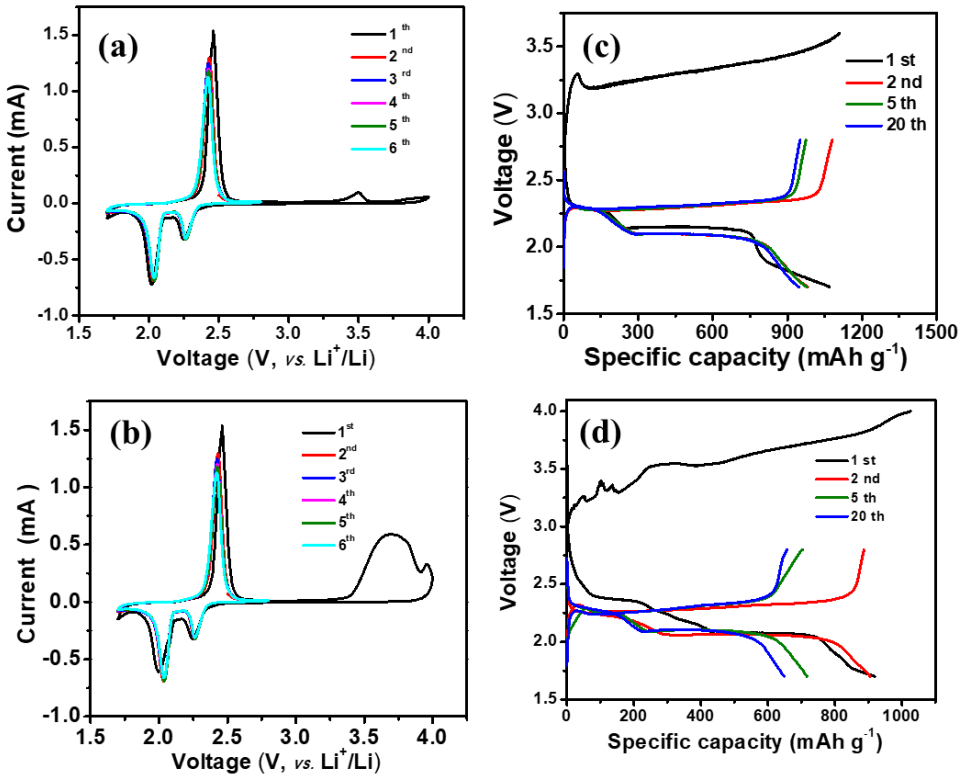

Figure 7.4. The CV profiles of (a) Li_2S@N-C and (b) pure Li_2S at 0.05 mV s^{-1}; the Charge-discharge profiles of (c) Li_2S@N-C and (d) pure Li_2S electrodes at different current density.

To validate the mitigative effect of N-doped carbon on the dissolution of polysulfides during the charge/discharge process, the cells were disassembled in fully charged state after 50 cycles, and the cycled Li_2S@N-C and pure Li_2S electrodes were soaked in dioxolane/dimethoxyethane (DOL/DME) (v:v = 1:1) solution for 12 hours, and the absorption spectra of the obtained solutions were collected using ultraviolet-visible (UV-vis) spectroscopy. The colour changes of the DOL/DME solutions exposed to the different electrodes were recorded using digital photographs, as shown in the insertion of

Figure 7.5. The cycled Li_2S@N-C electrode solution shows the lighter yellow colour compared with the pure Li_2S electrode, indicating a little bit lower content of polysulfides in the cycled Li_2S@N-C electrode and most polysulfides was absorbed by the N-doped carbon nanofibers. The UV-vis spectra of the obtained solutions were performed. The intensity of the adsorption peak of Li_2S@N-C electrode is lower than the pure Li_2S electrode, which indicates that the N-doped carbon could efficiently anchor and reduce the dissolution of polysulfides, as well as improving the utilization of the active materials, resulting a high specific capacity and stable cycling performance.

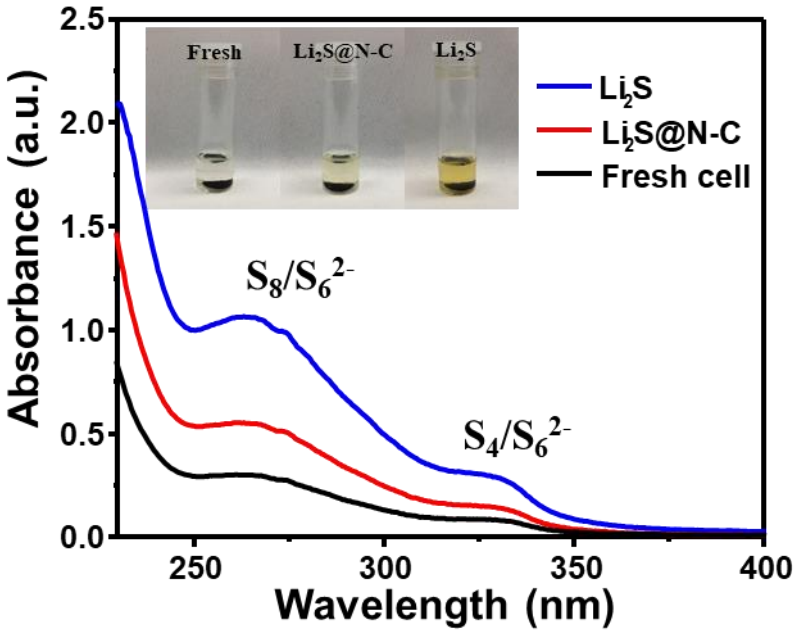

Figure 7.5. The UV/vis absorption spectra of DOL/DME solutions with cycled Li_2S@N-C and pure Li_2S electrodes after 50 cycles; Insertion show the colour of solutions with different electrodes.

For the practical application, the loading amount of active materials is very important because the discharge capacity of the electrode highly depended on the active materials loading. The controlled cathodes with different Li_2S loadings amount of 1, 2 and 3 mg

cm^{-2} were evaluated, as shown in Figure 7.6a. The electrodes were first fully activated at 0.1 C for 10 cycles, then cycled at 0.2 C for 200 cycles. As we can see, with the increasing of Li_2S loading, the specific capacities are decreasing. The Li_2S@N-C composites with a mass loading of 1 mg cm^{-2} deliver a highest specific discharge capacity of 1036.6 mA h g^{-1} at the first cycle, and a high capacity of 704.2 mA h g^{-1} is still maintained after 200 cycles at 0.2 C. After 200 cycles, Li_2S@N-C composites with a mass loading of 2 mg cm^{-2} and 3 mg cm^{-2} also show a specific capacity of 602.5 mA h g^{-1} and 479.3 mA h g^{-1}, respectively. These results indicate that the thick electrode could prevent the rapid transfer of electrons during active materials and reduce the utilization of active materials. But the Li_2S@N-C electrode with a mass loading of 3 mg cm^{-2} still delivers higher specific capacity than that of pure Li_2S with a mass loading of 3 mg cm^{-2}, which can be ascribed to the small size of Li_2S and the conductive N-doped carbon nanofibers, which both are beneficial to the fast transportation of electrons and improve the utilization of Li_2S. The rate capability of the Li_2S@N-C composites with different mass loading is shown in Figure 6b. The Li_2S@N-C composites with a mass loading of 1 mg cm^{-2} show the highest capacities at all current density, delivering a specific capacity of 1106.4, 880.3, 769.6, 683.9, 571.4, and 489.3 mA h g^{-1} at 0.1 C, 0.2 C,0.3 C, 0.5 C, 1 C and 2 C, even the current density is increased to 5 C, the specific capacity still can be reached to 380.4 mA h g^{-1}. When the current density was suddenly recovered back to 0.1 C, a capacity of 887.5 mA h g^{-1} is still obtained. In comparison, the Li_2S@N-C composites with a mass loading of 2 mg cm^{-2} still can delivered a capacity of 233 mA h g^{-1} at 5 C. The Li_2S@N-C composites with a mass loading of 3 mg cm^{-2} shows capacities of 916.2, 677, 598.1, 505.4, 376.8, 321 and 139 mA h g^{-1} at 0.1 C, 0.2 C, 0.3 C, 0.5 C, 1 C, 2 C and 5 C, respectively. The Li_2S@N-C electrode with high mass loading show good cycling stability and excellent rate capability, which can

be attributed to the following reasons: first, the small size of Li_2S prepared by solution-based method could possess small energy barrier in the first charging process,

which is easier to be activated and improve the utilization; Second, the N-doped carbon could absorb the dissolved polysulfides through strong chemical bonds, enhancing the reuse of active materials.

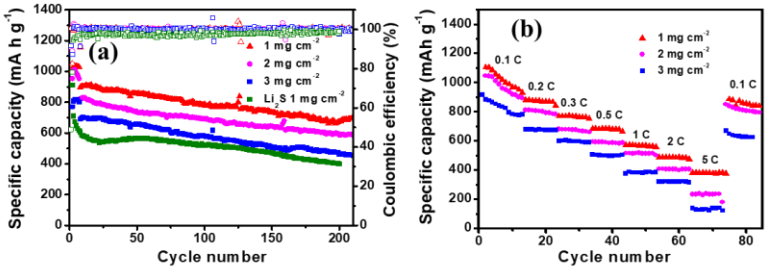

Figure 7.6. The (a) cycling performance and (b) rate capability of different electrode with different mass loading of active materials.

Table 7.1 Comparisons of cycling performances of this work with the reported Li_2S electrode for Li-S batteries.

Materials description	Li_2S content (wt%)	Li_2S loading (mg cm^{-2})	1st discharge capacity (mAh g^{-1})	Cycle number	Capacity after the reported cycles (mAh g^{-1})	Refs.
Li_2S coated N-C	68%	1	1036.6 (0.2 C)	200	704.2 (0.2 C)	This work
Li_2S/CB/NC	72%	1	1029 (0.2 C)	100	650 (0.2 C)	315
Carbon coated Li_2S/CB	70%	0.8	1020 (0.1 C)	200	665.4 (0.1 C)	309
Li_2S-rGO	66%	0.96	982 (0.1 C)	100	315 (0.1 C)	316
Li_2S/MWCNT	N/A	0.9	843 (0.2 C)	100	705 (0.2 C)	317
Li_2S-rGO paper	60%	1.5	1119 (0.1 C)	150	816 (0.1 C)	318
Li_2S-C	62%	N/A	330 (0.5 C)	40	280 (0.5 C)	319
Li_2S-C_{PAN}	~80%	1.7	~500 (0.01 C)	50	~380 (0.01 C)	320

7.4 Conclusions

In summary, a facile solution-based chemical method was reported to prepare Li_2S@N-C composites. Compared with the solid-based method and thermal treatment method, the solution-based method could obtain small size of Li_2S particle and uniform distribution on the matrixes without agglomeration, which could improve the tight contact between conductive agent and active materials. The N-doped carbon nanofibers matrix derived from PPy nanofibers could not only improve the conductivity of Li_2S, but also trap polysulfides to reduce the dissolution due to the strong chemical bonding between nitrogen atom and ploysulifdes. In addition, a Li_2S@N-C electrode with high mass loading of 3 mg cm^{-2} was prepared to show their possibility for practical application of our prepared samples, which delivered a high specific capacity of 916.2 mA h g^{-1} at 0.1 C and 321 mA h g^{-1} at 2 C, which is higher than that of pure Li_2S electrode with a mass loading of 1 mg cm^{-2}. The excellent cycling stability and rate capability can be ascribed to small size and uniform distribution of Li2S particles on the N-doped carbon nanofibers. This work is hopefully helpful to open a new sight for preparing nanosized Li_2S composites as a high-performed Li-S cathode material with high active material loading amount.

CHAPTER 8 CONCLUSIONS AND OUTLOOK

8.1 General conclusion

This doctoral work investigated four kinds of cathode materials for the rechargeable Li-S battery: sulfur coated PPy nanofibers as cathode materials with a PPy modified separator, uniform PPy coated sulfur/graphene aerogel, Li_2S-PPy composites, and Li_2S coated N-doped carbon nanofiber. The synthesis, physical features and electrochemical performances of these electodes were thoroughly characterized. The above obtained materials exhibited enhanced electrochemical performances, in terms of increased capacity, suppressed shuttle effect and stable cycling performance. These improvements are ascribed to the reasonable structure design and the strong chemical interaction of PPy, N-doped carbon and polysulfides, which are helpful for confining polysulfides into the cathode region and restraining the shuttle effect. A summary of the results are provided in the following sections.

A free-standing sulfur-PPy cathode and a PPy nanofiber coated separator were designed for flexible Li-S battery. The prepared PPy film not only has a rough surface, which can enhance adhesion of the active materials and trap dissolved polysulfides, but also possesses elastic property, which can accommodate the volume expansion and maintain the integrity of electrode during cycling. On the other hand, the PPy-separator not only acts as a reservoir for soluble lithium polysulfides, but also acts as an upper current collector to accelerate the kinetics of the electrochemical reactions. Moreover, PPy is electrochemically active and could contribute capacity to Li-S batteries. Benefiting from the above advantages, the flexible Li-S battery can deliver an initial discharge capacity

of 987 mA h g^{-1} and retains a capacity of 785 mA h g^{-1} after 20 cycles at 0.1 C. After repeated bending for 10 times, the capacity remains almost the same. In addition, the soft-packaged Li-S battery could power a device containing 24 white LEDs regardless of before or after bending, indicating its great potential application in flexible electronics. We believe that this flexible electrode structure may provide guidance for fabricating high energy, flexible electrochemical energy-storage devices.

A porous integrated sulfur/graphene aerogel with uniform PPy coating layer was designed via vapor phase deposition method as cathode material for Li-S batteries. The sulfur particles are encapsulated and firmly sealed by conductive graphene nanosheets, which not only provides a 3D conductive network to improve the utilization of sulfur and shorten electronic transfer distance, but also physically trapped dissolved polysulfides. More importantly, the uniform PPy layer coated on the outside of S/GA composites act as chemical adsorbent agent for polysulfides to mitigate the shuttle effect and ensure a long stable cycling performance due to due to its unique chain structure and inter- and/or intra-chain bonding with polysulfides. The as-prepared PPy@S/GA-VD electrode exhibits excellent rate and cycling capability, delivering a high capacity of 1167 and 409.1 mA h g^{-1} at 0.2 C and 5 C, respectively. At 0.5 C, it still can maintain a capacity of 698 mA h g^{-1} after 500 cycles with an ultra-slow decay rate of 0.03% per cycle. A very simple vapor phase deposition strategy was designed to moderate the shuttle effect and enhance the reaction kinetics of sulfur, which could shed light on the fabrication of long-life Li-S batteries in future.

A facile and up-scaled ball milling method was reported to prepare Li_2S-PPy hybrids. By adjusting the ball milling time, the Li_2S-PPy composites with 6h ball milling time show the best electrochemical performance. Because the Li_2S-PPy-6h composites display the smallest Li_2S size, and the smaller Li_2S particles were uniformly distributed in the PPy nanofiber matrixes, which could improve the tight contact between conductive agent and active materials. The PPy nanofibers matrix could not only improve the conductivity of Li_2S, but also trap polysulfides to reduce the dissolution due to the strong chemical bonding between PPy and ploysulifdes. In addition, a 3D carbon paper was used as current collector instead of 2D Al foil current collector, which could increase the loading amount of active materials. For further improving the cycling stability, a PPy-coated separator was prepared by directly coating PPy nanofiber slurry on the commercial separator, which is simple and cost-effective. After using the PPy-separator, the specific capacity and cycling performance of Li-S cell both enhanced, delivering an initial capacity of 885.5 mA h g^{-1} at 0.1 C, which still maintained at 529.7 mA h g^{-1} after 200 cycles with a capacity retention rate of about 59.8%, which is higher than that (48.2%) of Li-S cell with normal commercial separator. The excellent cycling stability can be ascribed to PPy layer between cathode and separator, which is acted as fishing net to capture dissolved polysulfides and improve their reuse.

A facile solution-based chemical method was reported to prepare Li_2S@N-C composites. Compared with the solid-based method and thermal treatment method, the solution-based method could obtain small size of Li_2S particle and uniform distribution on the matrixes without agglomeration, which could improve the tight contact between conductive agent and active materials. The N-doped carbon nanofibers matrix derived from PPy nanofibers could not only improve the conductivity of Li_2S, but also trap

polysulfides to reduce the dissolution due to the strong chemical bonding between nitrogen atom and ploysulifdes. In addition, a Li_2S@N-C electrode with high mass loading of 3 mg cm^{-2} was prepared to show their possibility for practical application of our prepared samples, which delivered a high specific capacity of 916.2 mA h g^{-1} at 0.1 C and 321 mA h g^{-1} at 2 C, which is higher than that of pure Li_2S electrode with a mass loading of 1 mg cm^{-2}. The excellent cycling stability and rate capability can be ascribed to small size and uniform distribution of Li_2S particles on the N-doped carbon nanofibers. This work is hopefully helpful to open a new sight for preparing nanosized Li_2S composites as a high-performed Li-S cathode material with high active material loading amount.

8.2 Outlook

Although some advances in improving the cycling stability of Li-S batteries have been made, there is still a long way to go to realize practically commercial applications of Li-S batteries. The low loading amount of active materials, short-term and unsatisfying the cycling performance, poor rate capability have hindered their further development. Therefore, exploring low-cost, high conductive matrixes and designing bifunctional separators to increase the utilization and loading mass of active materials, suppress the shuttle effect, improve the cycling stability are the primary task in the future to develop advanced Li-S batteries. The research strategy to fabricate high performance cathodes presented in this thesis could be of considerable interest and is expected to bring some inspiration to other researchers.

A flexible PPy film was assembled in Chapter 4, which acts as a bendable current collector to load sulfur active materials. Due to the rough surface of PPy film, active material strongly adhered on to avoid the peel-off of active materials during cycling.

This could offer a possibility to synthesize other 3D flexible conductive materials acting as current collector, especially some metal oxides/sulfides decorated graphene film. Because the conductivity of graphene is much higher than other carbonaceous materials, the metal oxides/sulfides have strong chemically interaction with LiPSs, and the unique 3D structure could load high amount of active materials. These maybe is a promising cathode material for high-performed Li-S batteries. In addition, PPy nanofiber was widely used in this thesis due to its high conductivity and unique chain-structure, which can also be used into other kinds of energy storage systems, such as sodium-ion batteries, lithium/sodium-air batteries et. al.

In addition to these, some further research efforts could be conducted based on the thesis as follows:

The method to prepare sulfur/graphene hydrogel in chapter 5 need to be modified in the following research works. Chemical synthesis of smaller sized sulfur particles will be better than directing using commercial sulfur powder. Because small particles could increase the contact area of sulfur with conductive agent, further improving the utilization of active materials and specific capacity.

Compared with sulfur, Li_2S can be paired with lithium-free anode to avoid the safety concerns related to metal lithium. In chapter 6, a simple ball milling method was applied to prepare Li_2S-PPy composites. Although the electrochemical performance is better than the pure Li_2S nanoparticles, it is not satisfactory. Novel synthesis method to prepare Li_2S nanostructures is highly needed, which could decrease the initial potential barrier. Moreover, a high cut-off voltage (4V) was applied to active the Li_2S in the first charging process, which may have some negative effect on the stability of electrolyte. Some catalyst can be added into cathode to low this barrier, such as metal sulfides have

been applied as an effective catalyst. Exploring some novel catalysts (metal carbides/ nitride) to low the potential barrier as well as fasten the redox reaction of polysulfides is a promising strategy to enhance the electrochemical performance of Li_2S cathode. In-situ characterization methods, including in-situ SEM, TEM, Raman, XRD, and synchrotron techniques, therefore, are essential for investigating the reaction mechanism.

In addition, the full Li-S batteries based on Li_2S cathode and lithium-free anode such as silicon, tin or carbon can be assembled and study their electrochemical performance. With the above mentioned challenges and insufficiencies solved, a brighter future for the next generation of batteries is expected to come.

REFERENCES

1. Z. Liu, D. Guan, W. Wei, S. J. Davis, P. Ciais, J. Bai, S. Peng, Q. Zhang, K. Hubacek and G. Marland, *Nature*, 2015, **524**, 335.
2. D. Larcher and J.-M. Tarascon, *Nature chemistry*, 2015, **7**, 19.
3. V. Khare, S. Nema and P. Baredar, *Renewable and Sustainable Energy Reviews*, 2016, **58**, 23-33.
4. G. N. Lewis and F. G. Keyes, *Journal of the American Chemical Society*, 1913, **35**, 340-344.
5. J. W. Fergus, *Journal of Power Sources*, 2010, **195**, 939-954.
6. W.-J. Zhang, *Journal of Power Sources*, 2011, **196**, 13-24.
7. S. S. Zhang, *Journal of Power Sources*, 2006, **162**, 1379-1394.
8. N. Nitta, F. Wu, J. T. Lee and G. Yushin, *Materials today*, 2015, **18**, 252-264.
9. M. S. Whittingham, *Chemical Reviews*, 2004, **104**, 4271-4302.
10. A. Manthiram, Y. Fu, S.-H. Chung, C. Zu and Y.-S. Su, *Chemical Reviews*, 2014, **114**, 11751-11787.
11. A. Manthiram, Y. Fu and Y.-S. Su, *Accounts of Chemical Research*, 2012, **46**, 1125-1134.
12. M. Wild, L. O'neill, T. Zhang, R. Purkayastha, G. Minton, M. Marinescu and G. Offer, *Energy & Environmental Science*, 2015, **8**, 3477-3494.
13. Y. Yang, G. Zheng and Y. Cui, *Chemical Society Reviews*, 2013, **42**, 3018-3032.
14. R. Fang, S. Zhao, Z. Sun, D. W. Wang, H. M. Cheng and F. Li, *Advanced Materials*, 2017, **29**, 1606823.
15. H.-J. Peng, J.-Q. Huang and Q. Zhang, *Chemical Society Reviews*, 2017, **46**, 5237-5288.
16. M.-K. Song, E. J. Cairns and Y. Zhang, *Nanoscale*, 2013, **5**, 2186-2204.
17. D. Aurbach, *Journal of The Electrochemical Society*, 2018, **165**, Y1-Y1.
18. J. Xu, T. Lawson, H. Fan, D. Su and G. Wang, *Advanced Energy Materials*, 2018, **8**, 1702607.
19. S. H. Chung, C. H. Chang and A. Manthiram, *Advanced Functional Materials*, 2018, 1801188.
20. J. Zhang, H. Huang, J. Bae, S. H. Chung, W. Zhang, A. Manthiram and G. Yu, *Small Methods*, 2018, **2**, 1700279.
21. H. J. Peng, J. Q. Huang, X. B. Cheng and Q. Zhang, *Advanced Energy Materials*, 2017, **7**, 1700260.
22. H. J. Peng, J. Q. Huang, X. B. Cheng and Q. Zhang, *Advanced Energy Materials*, 2017, **7**, 1770141.
23. Q. Pang, X. Liang, C. Y. Kwok and L. F. Nazar, *Nature Energy*, 2016, **1**, 16132.
24. J. Song, Z. Yu, M. L. Gordin and D. Wang, *Nano Letters*, 2016, **16**, 864-870.
25. Y. Xiang, J. Li, J. Lei, D. Liu, Z. Xie, D. Qu, K. Li, T. Deng and H. Tang, *ChemSusChem*, 2016, **9**, 3023-3039.
26. Q. Pang, X. Liang, C. Kwok and L. F. Nazar, *Journal of The Electrochemical Society*, 2015, **162**, A2567-A2576.
27. J. Liu, W. Li, L. Duan, X. Li, L. Ji, Z. Geng, K. Huang, L. Lu, L. Zhou and Z. Liu, *Nano Letters*, 2015, **15**, 5137-5142.
28. Y.-S. Su, 2013.
29. J. Park, J. Moon, C. Kim, J. H. Kang, E. Lim, J. Park, K. J. Lee, S.-H. Yu, J.-H. Seo and J. Lee, *NPG Asia Materials*, 2016, **8**, e272.

30. D. Su, D. Zhou, C. Wang and G. Wang, *Advanced Functional Materials*, 2018, 1800154.
31. R. Elazari, G. Salitra, A. Garsuch, A. Panchenko and D. Aurbach, *Advanced Materials*, 2011, **23**, 5641-5644.
32. X. Ji and L. F. Nazar, *Journal of Materials Chemistry*, 2010, **20**, 9821-9826.
33. G. Zheng, Y. Yang, J. J. Cha, S. S. Hong and Y. Cui, *Nano Letters*, 2011, **11**, 4462-4467.
34. X. Ji, K. T. Lee and L. F. Nazar, *Nature Materials*, 2009, **8**, 500.
35. G. Li, J. Sun, W. Hou, S. Jiang, Y. Huang and J. Geng, *Nature Communications*, 2016, **7**, 10601.
36. P. G. Bruce, S. A. Freunberger, L. J. Hardwick and J.-M. Tarascon, *Nature Materials*, 2012, **11**, 19.
37. G. Zhou, Springer, 2017, **7**, 75-94.
38. X. A. Chen, Z. Xiao, X. Ning, Z. Liu, Z. Yang, C. Zou, S. Wang, X. Chen, Y. Chen and S. Huang, *Advanced Energy Materials*, 2014, **4**, 1301988.
39. L. Suo, Y.-S. Hu, H. Li, M. Armand and L. Chen, *Nature Communications*, 2013, **4**, 1481.
40. A. Hayashi, T. Ohtomo, F. Mizuno, K. Tadanaga and M. Tatsumisago, *Electrochemistry Communications*, 2003, **5**, 701-705.
41. M. R. Busche, P. Adelhelm, H. Sommer, H. Schneider, K. Leitner and J. Janek, *Journal of Power Sources*, 2014, **259**, 289-299.
42. G. Zhou, D.-W. Wang, F. Li, P.-X. Hou, L. Yin, C. Liu, G. Q. M. Lu, I. R. Gentle and H.-M. Cheng, *Energy & Environmental Science*, 2012, **5**, 8901-8906.
43. G. Zhou, L. Li, C. Ma, S. Wang, Y. Shi, N. Koratkar, W. Ren, F. Li and H.-M. Cheng, *Nano Energy*, 2015, **11**, 356-365.
44. Z. W. Seh, W. Li, J. J. Cha, G. Zheng, Y. Yang, M. T. McDowell, P.-C. Hsu and Y. Cui, *Nature Communications*, 2013, **4**, 1331.
45. Z. Li, Y. Huang, L. Yuan, Z. Hao and Y. Huang, *Carbon*, 2015, **92**, 41-63.
46. W. Zhou, Y. Yu, H. Chen, F. J. DiSalvo and H. c. D. Abruña, *Journal of the American Chemical Society*, 2013, **135**, 16736-16743.
47. Y. Yang, G. Yu, J. J. Cha, H. Wu, M. Vosgueritchian, Y. Yao, Z. Bao and Y. Cui, *ACS Nano*, 2011, **5**, 9187-9193.
48. X. Liu, J. Q. Huang, Q. Zhang and L. Mai, *Advanced Materials*, 2017, **29**, 1601759.
49. S. Xin, L. Gu, N.-H. Zhao, Y.-X. Yin, L.-J. Zhou, Y.-G. Guo and L.-J. Wan, *Journal of the American Chemical Society*, 2012, **134**, 18510-18513.
50. Z. Li, L. Yuan, Z. Yi, Y. Sun, Y. Liu, Y. Jiang, Y. Shen, Y. Xin, Z. Zhang and Y. Huang, *Advanced Energy Materials*, 2014, **4**, 1301473.
51. H. J. Peng, J. Q. Huang, M. Q. Zhao, Q. Zhang, X. B. Cheng, X. Y. Liu, W. Z. Qian and F. Wei, *Advanced Functional Materials*, 2014, **24**, 2772-2781.
52. Z. Li, Y. Jiang, L. Yuan, Z. Yi, C. Wu, Y. Liu, P. Strasser and Y. Huang, *ACS Nano*, 2014, **8**, 9295-9303.
53. X. Li, Y. Cao, W. Qi, L. V. Saraf, J. Xiao, Z. Nie, J. Mietek, J. G. Zhang, B. Schwenzer and J. Liu, *Journal of Materials Chemistry*, 2011, **21**, 16603-16610.
54. J. Zheng, G. Guo, H. Li, L. Wang, B. Wang, H. Yu, Y. Yan, D. Yang and A. Dong, *ACS Energy Letters*, 2017, **2**, 1105-1114.
55. Y. Zhao, W. Wu, J. Li, Z. Xu and L. Guan, *Advanced Materials*, 2014, **26**, 5113-5118.
56. Z. Li, H. B. Wu and X. W. D. Lou, *Energy & Environmental Science*, 2016, **9**, 3061-3070.

57. N. Brun, K. Sakaushi, L. Yu, L. Giebeler, J. Eckert and M. M. Titirici, *Physical Chemistry Chemical Physics*, 2013, **15**, 6080-6087.
58. C. Zhang, H. B. Wu, C. Yuan, Z. Guo and X. W. Lou, *Angewandte Chemie*, 2012, **51**, 9594-9594.
59. R. Raccichini, A. Varzi, S. Passerini and B. Scrosati, *Nature Materials*, 2015, **14**, 271-279.
60. G. Hu, C. Xu, Z. Sun, S. Wang, H. M. Cheng, F. Li and W. Ren, *Advanced Materials*, 2016, **28**, 1603-1609.
61. S. Lu, Y. Cheng, X. Wu and J. Liu, *Nano Letters*, 2013, **13**, 2485-2489.
62. H. Wang, Y. Yang, Y. Liang, J. T. Robinson, Y. Li, A. Jackson, Y. Cui and H. Dai, *Nano Letters*, 2011, **11**, 2644-2647.
63. L. Zhu, H.-J. Peng, J. Liang, J.-Q. Huang, C.-M. Chen, X. Guo, W. Zhu, P. Li and Q. Zhang, *Nano Energy*, 2015, **11**, 746-755.
64. Y. Qiu, W. Li, W. Zhao, G. Li, Y. Hou, M. Liu, L. Zhou, F. Ye, H. Li and Z. Wei, *Nano Letters*, 2014, **14**, 4821.
65. C. Tang, Q. Zhang, M. Q. Zhao, J. Q. Huang, X. B. Cheng, G. L. Tian, H. J. Peng and F. Wei, *Advanced Materials*, 2014, **26**, 6100-6105.
66. G. Zhou, Y. Zhao and A. Manthiram, *Advanced Energy Materials*, 2015, **5**.
67. J. Song, M. L. Gordin, T. Xu, S. Chen, Z. Yu, H. Sohn, J. Lu, Y. Ren, Y. Duan and D. Wang, *Angewandte Chemie International Edition*, 2015, **54**, 4325-4329.
68. Y. Qiu, W. Li, W. Zhao, G. Li, Y. Hou, M. Liu, L. Zhou, F. Ye, H. Li and Z. Wei, *Nano Letters*, 2014, **14**, 4821-4827.
69. W. Deng, A. Hu, X. Chen, S. Zhang, Q. Tang, Z. Liu, B. Fan and K. Xiao, *Journal of Power Sources*, 2016, **322**, 138-146.
70. F. Wu, J. Li, Y. Tian, Y. Su, J. Wang, W. Yang, N. Li, S. Chen and L. Bao, *Sci Rep-Uk*, 2015, **5**.
71. C.-P. Yang, Y.-X. Yin, H. Ye, K.-C. Jiang, J. Zhang and Y.-G. Guo, *ACS Applied Materials & Interface*, 2014, **6**, 8789-8795.
72. G. Xu, B. Ding, P. Nie, L. Shen, J. Wang and X. Zhang, *Chemistry-A European Journal*, 2013, **19**, 12306-12312.
73. F. Sun, J. Wang, H. Chen, W. Li, W. Qiao, D. Long and L. Ling, *Applied Materials & Interfaces*, 2013, **5**, 5630-5638.
74. G. Zheng, Q. Zhang, J. J. Cha, Y. Yang, W. Li, Z. W. Seh and Y. Cui, *Nano Letters*, 2013, **13**, 1265-1270.
75. J. Wang, K. Yue, X. Zhu, K. L. Wang and L. Duan, *Physical Chemistry Chemical Physics*, 2016, **18**, 261-266.
76. L. Xiao, Y. Cao, J. Xiao, B. Schwenzer, M. H. Engelhard, L. V. Saraf, Z. Nie, G. J. Exarhos and J. Liu, *Advanced Materials*, 2012, **24**, 1176-1181.
77. G. C. Li, G. R. Li, S. H. Ye and X. P. Gao, *Advanced Energy Materials*, 2012, **2**, 1238-1245.
78. L. Yin, J. Wang, J. Yang and Y. Nuli, *Journal of Materials Chemistry*, 2011, **21**, 6807-6810.
79. L. Yin, J. Wang, F. Lin, J. Yang and Y. Nuli, *Energy & Environmental Science*, 2012, **5**, 6966-6972.
80. J. Wang, J. Chen, K. Konstantinov, L. Zhao, S. H. Ng, G. Wang, Z. Guo and H. Liu, *Electrochim Acta*, 2006, **51**, 4634-4638.
81. Y. Fu and A. Manthiram, *The Journal of Physical Chemistry C*, 2012, **116**, 8910-8915.
82. F. Wu, J. Chen, R. Chen, S. Wu, L. Li, S. Chen and T. Zhao, *The Journal of Physical Chemistry C*, 2011, **115**, 6057-6063.

83. B. Oschmann, J. Park, C. Kim, K. Char, Y.-E. Sung and R. Zentel, *Chemistry of Materials*, 2015, **27**, 7011-7017.
84. W. Li, Q. Zhang, G. Zheng, Z. W. Seh, H. Yao and Y. Cui, *Nano Letters*, 2013, **13**, 5534-5540.
85. Y. Dong, S. Liu, Z. Wang, Y. Liu, Z. Zhao and J. Qiu, *Nanoscale*, 2015, **7**, 7569-7573.
86. W. Bao, D. Su, W. Zhang, X. Guo and G. Wang, *Advanced Functional Materials*, 2016, **26**, 8746-8756.
87. J. T. Lee, Y. Zhao, S. Thieme, H. Kim, M. Oschatz, L. Borchardt, A. Magasinski, W. I. Cho, S. Kaskel and G. Yushin, *Advanced Materials*, 2013, **25**, 4573-4579.
88. Z. Cui, C. Zu, W. Zhou, A. Manthiram and J. B. Goodenough, *Advanced Materials*, 2016, **28**, 6926-6931.
89. M.-S. Song, S.-C. Han, H.-S. Kim, J.-H. Kim, K.-T. Kim, Y.-M. Kang, H.-J. Ahn, S. Dou and J.-Y. Lee, *Journal Electrochemical Society*, 2004, **151**, A791-A795.
90. Y. Choi, B. Jung, D. Lee, J. Jeong, K. Kim, H. Ahn, K. Cho and H. Gu, *Physica Scripta*, 2007, **2007**, 62.
91. X. Ji, S. Evers, R. Black and L. F. Nazar, *Nature Communications*, 2011, **2**, 325.
92. Z. Zhang, Q. Li, S. Jiang, K. Zhang, Y. Lai and J. Li, *Chemistry-A European Journal*, 2015, **21**, 1343-1349.
93. Z. Xiao, Z. Yang, L. Wang, H. Nie, M. e. Zhong, Q. Lai, X. Xu, L. Zhang and S. Huang, *Advanced Materials*, 2015, **27**, 2891-2898.
94. J. Y. Hwang, H. M. Kim, S. K. Lee, J. H. Lee, A. Abouimrane, M. A. Khaleel, I. Belharouak, A. Manthiram and Y. K. Sun, *Advanced Energy Materials*, 2016, **6**, 1501480.
95. B. Ding, L. Shen, G. Xu, P. Nie and X. Zhang, *Electrochimica Acta*, 2013, **107**, 78-84.
96. Z. W. Seh, W. Li, J. J. Cha, G. Zheng, Y. Yang, M. T. McDowell, P.-C. Hsu and Y. Cui, *Nature Communications*, 2013, **4**, 1331.
97. Q. Pang, D. Kundu, M. Cuisinier and L. Nazar, *Nature Communications*, 2014, **5**, 4759.
98. T. Xinyong, W. Jianguo, Y. Zhuogao, C. Qiuxia, Z. Guangyuan, G. Yongping, H. Hui, X. Yang, L. Chu and Z. Wenkui, *Nano Letters*, 2014, **14**, 5288-5294.
99. Z. Li, J. Zhang and X. W. Lou, *Angewandte Chemie International Edition*, 2015, **54**, 12886-12890.
100. Q. Fan, W. Liu, Z. Weng, Y. Sun and H. Wang, *Journal of the American Chemical Society*, 2015, **137**, 12946-12953.
101. Q. Qu, T. Gao, H. Zheng, Y. Wang, X. Li, X. Li, J. Chen, Y. Han, J. Shao and H. Zheng, *Advanced Materials Interfaces*, 2015, **2**, 1500048.
102. W. Li, J. Hicks-Garner, J. Wang, J. Liu, A. F. Gross, E. Sherman, J. Graetz, J. J. Vajo and P. Liu, *Chemistry of Materials*, 2014, **26**, 3403-3410.
103. N. Hu, X. Lv, Y. Dai, L. Fan, D. Xiong and X. Li, *ACS Applied Materials & Interfaces*, 2018, **10**, 18665-18674..
104. X. Li, Y. Lu, Z. Hou, W. Zhang, Y. Zhu, Y. Qian, J. Liang and Y. Qian, *ACS Applied Materials & Interfaces*, 2016, **8**, 19550-19557.
105. C. Zhao, C. Shen, F. Xin, Z. Sun and W. Han, *Materials Letters*, 2014, **137**, 52-55.
106. R. Ponraj, A. G. Kannan, J. H. Ahn and D.-W. Kim, *ACS Applied Materials & Interfaces*, 2016, **8**, 4000-4006.

107. J. Zhang, P. Gu, J. Xu, H. Xue and H. Pang, *Nanoscale*, 2016, **8**, 18578-18595.
108. X. Gu, C.-j. Tong, B. Wen, L.-m. Liu, C. Lai and S. Zhang, *Electrochimica Acta*, 2016, **196**, 369-376.
109. H. Cheng, S. Wang, D. Tao and M. Wang, *Functional Materials Letters*, 2014, **7**, 1450020.
110. X. Liu, J. Q. Huang, Q. Zhang and L. Mai, *Advanced Materials*, 2017, **29**, 1601759.
111. L. Ma, S. Wei, H. L. Zhuang, K. E. Hendrickson, R. G. Hennig and L. A. Archer, *Journal of Materials Chemistry A*, 2015, **3**, 19857-19866.
112. Q. Pang, D. Kundu and L. F. Nazar, *Materials Horizons*, 2016, **3**, 130-136.
113. Z. Yuan, H.-J. Peng, T.-Z. Hou, J.-Q. Huang, C.-M. Chen, D.-W. Wang, X.-B. Cheng, F. Wei and Q. Zhang, *Nano Letters*, 2016, **16**, 519-527.
114. J. Liu, X. Zheng, Z. Shi and S. Zhang, *Ionics*, 2014, **20**, 659-664.
115. X. Li, L. Chu, Y. Wang and L. Pan, *Materials Science and Engineering: B*, 2016, **205**, 46-54.
116. S. S. Zhang and D. T. Tran, *Journal of Materials Chemistry A*, 2016, **4**, 4371-4374.
117. Y. Lu, X. Li, J. Liang, L. Hu, Y. Zhu and Y. Qian, *Nanoscale*, 2016, **8**, 17616-17622.
118. K. Sun, D. Su, Q. Zhang, D. C. Bock, A. C. Marschilok, K. J. Takeuchi, E. S. Takeuchi and H. Gan, *Journal of The Electrochemical Society*, 2015, **162**, A2834-A2839.
119. S. Bai, X. Liu, K. Zhu, S. Wu and H. Zhou, *Nature Energy*, 2016, **1**, 16094.
120. Y.-S. Su and A. Manthiram, *Nature Communications*, 2012, **3**, 1166.
121. H. Yao, K. Yan, W. Li, G. Zheng, D. Kong, Z. W. Seh, V. K. Narasimhan, Z. Liang and Y. Cui, *Energ Environ Sci*, 2014, **7**, 3381-3390.
122. H. Wang, W. Zhang, H. Liu and Z. Guo, *Angewandte Chemie International Edition*, 2016, **55**, 3992-3996.
123. Z. Jin, K. Xie, X. Hong, Z. Hu and X. Liu, *Journal of Power Sources*, 2012, **218**, 163-167.
124. M. Gu, J. Lee, Y. Kim, J. S. Kim, B. Y. Jang, K. T. Lee and B.-S. Kim, *RSC Advances*, 2014, **4**, 46940-46946.
125. Z. Zhang, Y. Lai, Z. Zhang, K. Zhang and J. Li, *Electrochim Acta*, 2014, **129**, 55-61.
126. Y.-S. Su and A. Manthiram, *Chemical Communications*, 2012, **48**, 8817-8819.
127. S.-H. Chung and A. Manthiram, *Chemical Communications*, 2014, **50**, 4184-4187.
128. W. Lin, Y. Chen, P. Li, J. He, Y. Zhao, Z. Wang, J. Liu, F. Qi, B. Zheng and J. Zhou, *Journal of the Electrochemical Society*, 2015, **162**, A1624-A1629.
129. G. Ma, Z. Wen, Q. Wang, S. Chen, P. Peng, J. Jin and X. Wu, *Journal of Power Sources*, 2015, **273**, 511-516.
130. K. Zhang, F. Qin, J. Fang, Q. Li, M. Jia, Y. Lai, Z. Zhang and J. Li, *Journal of Solid State Electrochemistry*, 2014, **18**, 1025-1029.
131. X. Qian, L. Jin, D. Zhao, X. Yang, S. Wang, X. Shen, D. Rao, S. Yao, Y. Zhou and X. Xi, *Electrochimica Acta*, 2016, **192**, 346-356.
132. K. Dokko, N. Tachikawa, K. Yamauchi, M. Tsuchiya, A. Yamazaki, E. Takashima, J.-W. Park, K. Ueno, S. Seki and N. Serizawa, *Journal of The Electrochemical Society*, 2013, **160**, A1304-A1310.
133. S. S. Zhang, *Electrochemistry Communications*, 2006, **8**, 1423-1428.

134. J. Gao, M. A. Lowe, Y. Kiya and H. c. D. Abruña, *The Journal of Physical Chemistry C*, 2011, **115**, 25132-25137.
135. B. Zhang, X. Qin, G. Li and X. Gao, *Energy & Environmental Science*, 2010, **3**, 1531-1537.
136. W. Zhang, D. Qiao, J. Pan, Y. Cao, H. Yang and X. Ai, *Electrochimica Acta*, 2013, **87**, 497-502.
137. M. R. Kaiser, S. Chou, H. K. Liu, S. X. Dou, C. Wang and J. Wang, *Advanced Materials*, 2017, **29**, 1700449.
138. H.-S. Ryu, H.-J. Ahn, K.-W. Kim, J.-H. Ahn, K.-K. Cho, T.-H. Nam, J.-U. Kim and G.-B. Cho, *Journal of Power Sources*, 2006, **163**, 201-206.
139. J.-W. Choi, J.-K. Kim, G. Cheruvally, J.-H. Ahn, H.-J. Ahn and K.-W. Kim, *Electrochimica Acta*, 2007, **52**, 2075-2082.
140. J. Wang, J. Yang, J. Xie, N. Xu and Y. Li, *Electrochemistry Communications*, 2002, **4**, 499-502.
141. J. Hassoun and B. Scrosati, *Advanced Materials*, 2010, **22**, 5198-5201.
142. M. Nagao, A. Hayashi and M. Tatsumisago, *Electrochimica Acta*, 2011, **56**, 6055-6059.
143. J. E. Trevey, Y. S. Jung and S.-H. Lee, *Electrochimica Acta*, 2011, **56**, 4243-4247.
144. J. Zheng, M. Gu, H. Chen, P. Meduri, M. H. Engelhard, J.-G. Zhang, J. Liu and J. Xiao, *Journal of Materials Chemistry A*, 2013, **1**, 8464-8470.
145. J. H. Shin and E. J. Cairns, *Journal of Power Sources*, 2008, **177**, 537-545.
146. S. Kim, Y. Jung and S.-J. Park, *Electrochimica Acta*, 2007, **52**, 2116-2122.
147. X. Liang, Z. Wen, Y. Liu, M. Wu, J. Jin, H. Zhang and X. Wu, *Journal of Power Sources*, 2011, **196**, 9839-9843.
148. S. S. Zhang, *Electrochimica Acta*, 2012, **70**, 344-348.
149. X. Liang, M. Zhang, M. R. Kaiser, X. Gao, K. Konstantinov, R. Tandiono, Z. Wang, H.-K. Liu, S.-X. Dou and J. Wang, *Nano Energy*, 2015, **11**, 587-599.
150. G. Ma, Z. Wen, M. Wu, C. Shen, Q. Wang, J. Jin and X. Wu, *Chemical Communications*, 2014, **50**, 14209-14212.
151. C. Huang, J. Xiao, Y. Shao, J. Zheng, W. D. Bennett, D. Lu, L. V. Saraf, M. Engelhard, L. Ji and J. Zhang, *Nature Communications*, 2014, **5**, 3015.
152. R. Cao, W. Xu, D. Lv, J. Xiao and J. G. Zhang, *Advanced Energy Materials*, 2015, **5**, 1402273.
153. S. Xiong, K. Xie, Y. Diao and X. Hong, *Electrochimica Acta*, 2012, **83**, 78-86.
154. F. Ding, W. Xu, G. L. Graff, J. Zhang, M. L. Sushko, X. Chen, Y. Shao, M. H. Engelhard, Z. Nie and J. Xiao, *Journal of the American Chemical Society*, 2013, **135**, 4450-4456.
155. X. Zhang, W. Wang, A. Wang, Y. Huang, K. Yuan, Z. Yu, J. Qiu and Y. Yang, *Journal of Materials Chemistry A*, 2014, **2**, 11660-11665.
156. D. Lin, Y. Liu, Z. Liang, H.-W. Lee, J. Sun, H. Wang, K. Yan, J. Xie and Y. Cui, *Nature Nanotechnology*, 2016, **11**, 626.
157. Y. Liu, D. Lin, Z. Liang, J. Zhao, K. Yan and Y. Cui, *Nature Communications*, 2016, **7**, 10992.
158. Y. Yan, Y. X. Yin, S. Xin, J. Su, Y. G. Guo and L. J. Wan, *Electrochimica Acta*, 2013, **91**, 58-61.
159. F. Ye, Y. Hou, M. Liu, W. Li, X. Yang, Y. Qiu, L. Zhou, H. Li, Y. Xu and Y. Zhang, *Nanoscale*, 2015, **7**, 9472-9476.
160. C. Wang, X. Wang, Y. Yang, A. Kushima, J. Chen, Y. Huang and J. Li, *Nano Letters*, 2015, **15**, 1796-1802.

161. C. Y. Nan, Z. Lin, H. G. Liao, M. K. Song, Y. D. Li and E. J. Cairns, *Journal of the American Chemical Society*, 2014, **136**, 4659-4663.
162. G. Zhou, J. Sun, Y. Jin, W. Chen, C. Zu, R. Zhang, Y. Qiu, J. Zhao, D. Zhuo and Y. Liu, *Advanced Materials*, 2017, **29**, 1603366.
163. G. Zhou, H. Tian, Y. Jin, X. Tao, B. Liu, R. Zhang, Z. W. Seh, D. Zhuo, Y. Liu and J. Sun, *Proceedings of the National Academy of Sciences*, 2017, **114**, 840-845.
164. Y. Yang, M. T. McDowell, A. Jackson, J. J. Cha, S. S. Hong and Y. Cui, *Nano Letters*, 2010, **10**, 1486-1491.
165. Y. Hwa, J. Zhao and E. J. Cairns, *Nano Letters*, 2015, **15**, 3479-3486.
166. Y. Fu, Y. S. Su and A. Manthiram, *Advanced Energy Materials*, 2014, **4**, 1300655.
167. K. Cai, M.-K. Song, E. J. Cairns and Y. Zhang, *Nano Letters*, 2012, **12**, 6474-6479.
168. Y. Chen, S. Lu, J. Zhou, W. Qin and X. Wu, *Advanced Functional Materials*, 2017, **27**, 1700987.
169. Y. Yang, G. Y. Zheng, S. Misra, J. Nelson, M. F. Toney and Y. Gui, *Journal of the American Chemical Society*, 2012, **134**, 15387-15394.
170. H. Yuan, X. Chen, G. Zhou, W. Zhang, J. Luo, H. Huang, Y. Gan, C. Liang, Y. Xia and J. Zhang, *ACS Energy Letters*, 2017, **2**, 1711-1719.
171. G. Zhou, J. Sun, Y. Jin, W. Chen, C. Zu, R. Zhang, Y. Qiu, J. Zhao, D. Zhuo and Y. Liu, *Advanced Materials*, 2017, **29**, 1603366.
172. X. Wang, X. Bi, S. Wang, Y. Zhang, H. Du and J. Lu, *Acs Applied Materials & Interfaces*, 2018, **10**, 16552-16560.
173. F. Wu, T. P. Pollard, E. Zhao, Y. Xiao, M. Olguin, O. Borodin and G. Yushin, *Energy & Environmental Science*, 2018, **11**, 807-817.
174. J. Zhang, Y. Shi, Y. Ding, L. Peng, W. Zhang and G. Yu, *Advanced Energy Materials*, 2017, **7**, 1602876.
175. J. Hassoun and B. Scrosati, *Angewandte Chemie International Edition*, 2010, **49**, 2371-2374.
176. M. Liu, Y. Ren, H. Jiang, C. Luo, F. Kang and T. Zhao, *Nano Energy*, 2017, **40**, 240-247.
177. K. Zhang, L. Wang, Z. Hu, F. Cheng and J. Chen, *Scientific Reports*, 2014, **4**, 6467.
178. S. Zheng, Y. Chen, Y. Xu, F. Yi, Y. Zhu, Y. Liu, J. Yang and C. Wang, *ACS Nano*, 2013, **7**, 10995-11003.
179. Y. Chen, J. Cao, M. Zheng, X. Ke, H. Ji, J. Liu and G. Ji, *Chemistry Letters*, 2006, **35**, 700-701.
180. C. Weidenthaler, *Nanoscale*, 2011, **3**, 792-810.
181. G. Du, 2011.
182. H. Nishide and K. Oyaizu, *Science*, 2008, **319**, 737-738.
183. G. Zhou, F. Li and H.-M. Cheng, *Energy & Environmental Science*, 2014, **7**, 1307-1338.
184. J.-M. Tarascon and M. Armand, *Nature*, 2001, **414**, 359-367.
185. V. Etacheri, R. Marom, R. Elazari, G. Salitra and D. Aurbach, *Energy & Environmental Science*, 2011, **4**, 3243-3262.
186. J. Cheng, B. Wang, H. L. Xin, C. Kim, F. Nie, X. Li, G. Yang and H. Huang, *Journal of Materials Chemistry A*, 2014, **2**, 2701-2707.
187. L. Hu, H. Wu, F. La Mantia, Y. Yang and Y. Cui, *ACS Nano*, 2010, **4**, 5843-5848.

188. J. Liu, K. Song, P. A. van Aken, J. Maier and Y. Yu, *Nano Letters*, 2014, **14**, 2597-2603.
189. Q. Sun, X. Fang, W. Weng, J. Deng, P. Chen, J. Ren, G. Guan, M. Wang and H. Peng, *Angewandte Chemie*, 2015, **127**, 10685-10690.
190. J. Cao, C. Chen, Q. Zhao, N. Zhang, Q. Lu, X. Wang, Z. Niu and J. Chen, *Advanced Materials*, 2016, **28**, 9629-9636.
191. J. Wang, C. O. Too, D. Zhou and G. G. Wallace, *Journal of Power Sources*, 2005, **140**, 162-167.
192. M. D. Hager, P. Greil, C. Leyens, S. van der Zwaag and U. S. Schubert, *Advanced Materials*, 2010, **22**, 5424-5430.
193. S.-H. Chung and A. Manthiram, *The Journal of Physical Chemistry Letters*, 2014, **5**, 1978-1983.
194. C.-H. Chang, S.-H. Chung and A. Manthiram, *Journal of Materials Chemistry A*, 2015, **3**, 18829-18834.
195. R. Fang, S. Zhao, Z. Sun, D. W. Wang, H. M. Cheng and F. Li, *Advanced Materials*, 2017, **29**, 1606823.
196. T.-G. Jeong, Y. H. Moon, H.-H. Chun, H. S. Kim, B. W. Cho and Y.-T. Kim, *Chemical Communications*, 2013, **49**, 11107-11109.
197. M. R. Kaiser, J. Wang, X. Liang, H.-K. Liu and S.-X. Dou, *Journal of Power Sources*, 2015, **279**, 231-237.
198. I. Sultana, M. Rahman, S. Li, J. Wang, C. Wang, G. G. Wallace and H.-K. Liu, *Electrochim Acta*, 2012, **60**, 201-205.
199. L. Wang, S. Dou, J. Xu, H. K. Liu, S. Wang, J. Ma and S. X. Dou, *Chemical Communications*, 2015, **51**, 11791-11794.
200. C. Zu and A. Manthiram, *Advanced Energy Materials*, 2013, **3**, 1008-1012.
201. L. Zhang, L. Ji, P.-A. Glans, Y. Zhang, J. Zhu and J. Guo, *Physical Chemistry Chemical Physics*, 2012, **14**, 13670-13675.
202. J. Shao, X. Li, L. Zhang, Q. Qu and H. Zheng, *Nanoscale*, 2013, **5**, 1460-1464.
203. X. Li, M. Rao, H. Lin, D. Chen, Y. Liu, S. Liu, Y. Liao, L. Xing, M. Xu and W. Li, *Journal of Materials Chemistry A*, 2015, **3**, 18098-18104.
204. C. Wang, W. Wan, J.-T. Chen, H.-H. Zhou, X.-X. Zhang, L.-X. Yuan and Y.-H. Huang, *Journal of Materials Chemistry A*, 2013, **1**, 1716-1723.
205. G. Zheng, Y. Yang, J. J. Cha, S. S. Hong and Y. Cui, *Nano Letters*, 2011, **2011**, 4462.
206. G. Zhou, E. Paek, G. S. Hwang and A. Manthiram, *Nat Commun*, 2015, **6**, 7760.
207. N. A. Canas, K. Hirose, B. Pascucci, N. Wagner, K. A. Friedrich and R. Hiesgen, *Electrochim Acta*, 2013, **97**, 42-51.
208. G. Zhou, S. Pei, L. Li, D. W. Wang, S. Wang, K. Huang, L. C. Yin, F. Li and H. M. Cheng, *Advanced Materials*, 2014, **26**, 625-631.
209. N. Nakamura, T. Yokoshima, H. Nara, T. Momma and T. Osaka, *Journal of Power Sources*, 2015, **274**, 1263-1266.
210. W. Qin, B. Fang, S. Lu, Z. Wang, Y. Chen, X. Wu and L. Han, *RSC Advances*, 2015, **5**, 13153-13156.
211. Y. Fu and A. Manthiram, *RSC Advances*, 2012, **2**, 5927-5929.
212. Y. Xie, H. Zhao, H. Cheng, C. Hu, W. Fang, J. Fang, J. Xu and Z. Chen, *Applied Energy*, 2016, **175**, 522-528.
213. J. E. Hyun, P.-C. Lee and I. Tatsumi, *Electrochimica Acta*, 2015, **176**, 887-892.
214. G. Ma, Z. Wen, Q. Wang, C. Shen, P. Peng, J. Jin and X. Wu, *Journal of Power Sources*, 2015, **273**, 511-516.
215. B. Dunn, H. Kamath and J.-M. Tarascon, *Science*, 2011, **334**, 928-935.

216. Y. X. Yin, S. Xin, Y. G. Guo and L. J. Wan, *Angewandte Chemie International Edition*, 2013, **52**, 13186-13200.
217. H. J. Peng, J. Q. Huang, X. B. Cheng and Q. Zhang, *Advanced Energy Materials*, 2017, **7**, 1700260.
218. J. Rao, R. Xu, T. Zhou, D. Zhang and C. Zhang, *Journal of Alloys and Compounds*, 2017, **728**, 376-382.
219. X.-X. Peng, Y.-Q. Lu, L.-L. Zhou, T. Sheng, S.-Y. Shen, H.-G. Liao, L. Huang, J.-T. Li and S.-G. Sun, *Nano Energy*, 2017, **32**, 503-510.
220. C. Tang, B. Q. Li, Q. Zhang, L. Zhu, H. F. Wang, J. L. Shi and F. Wei, *Advanced Functional Materials*, 2016, **26**, 577-585.
221. J. Zhang, C. P. Yang, Y. X. Yin, L. J. Wan and Y. G. Guo, *Advanced Materials*, 2016, **28**, 9539-9544.
222. L. Borchardt, M. Oschatz and S. Kaskel, *Chemistry-A European Journal*, 2016, **22**, 7324-7351.
223. W. Qian, Q. Gao, H. Zhang, W. Tian, Z. Li and Y. Tan, *Electrochimica Acta*, 2017, **235**, 32-41.
224. W. Ai, W. Zhou, Z. Du, Y. Chen, Z. Sun, C. Wu, C. Zou, C. Li, W. Huang and T. Yu, *Energy Storage Materials*, 2017, **6**, 112-118.
225. S. Li, X. Xia, Y. Wang, X. Wang and J. Tu, *Journal of Power Sources*, 2017, **342**, 224-230.
226. Y. Ye, F. Wu, Y. Liu, T. Zhao, J. Qian, Y. Xing, W. Li, J. Huang, L. Li and Q. Huang, *Advanced Materials*, 2017, **7**, 1602543.
227. Z. Zhang, L. L. Kong, S. Liu, G. R. Li and X. P. Gao, *Advanced Energy Materials*, 2017, **7**, 160254.
228. J.-Q. Huang, Q. Zhang and F. Wei, *Energy Storage Materials*, 2015, **1**, 127-145.
229. J. Y. Hwang, H. M. Kim, S. K. Lee, J. H. Lee, A. Abouimrane, M. A. Khaleel, I. Belharouak, A. Manthiram and Y. K. Sun, *Advanced Energy Materials*, 2016, **6**, 1501480.
230. Y. Fan, Z. Yang, W. Hua, D. Liu, T. Tao, M. M. Rahman, W. Lei, S. Huang and Y. Chen, *Advanced Energy Materials*, 2017, **7**, 1602380.
231. S. S. Zhang, *Journal of Power Sources*, 2013, **231**, 153-162.
232. S. Xiong, K. Xie, E. Blomberg, P. Jacobsson and A. Matic, *Journal of Power Sources*, 2014, **252**, 150-155.
233. T. Yamada, S. Ito, R. Omoda, T. Watanabe, Y. Aihara, M. Agostini, U. Ulissi, J. Hassoun and B. Scrosati, *Journal of The Electrochemical Society*, 2015, **162**, A646-A651.
234. Q. Pang, X. Liang, C. Y. Kwok and L. F. Nazar, *Nature Energy*, 2016, **1**, 16132.
235. Y. Yang, M. Qiu, L. Liu, D. Su, Y. Pi and G. Yan, *Nano*, 2016, **11**, 1650124 .
236. K. Yang, Q. Gao, Y. Tan, W. Tian, W. Qian, L. Zhu and C. Yang, *Chemistry-A European Journal*, 2016, **22**, 3239-3244.
237. Y. L. Ding, P. Kopold, K. Hahn, P. A. van Aken, J. Maier and Y. Yu, *Advanced Functional Materials*, 2016, **26**, 1112-1119.
238. C. Shen, J. Xie, M. Zhang, M. A. Hendrickson, E. J. Plichta and J. P. Zheng, *ECS Transactions*, 2017, **77**, 457-465.
239. J. Guo, Y. Xu and C. Wang, *Nano Letters*, 2011, **11**, 4288-4294.
240. H. Wang, Y. Yang, Y. Liang, J. T. Robinson, Y. Li, A. Jackson, Y. Cui and H. Dai, *Nano Letters*, 2011, **11**, 2644-2647.
241. R. Fang, S. Zhao, S. Pei, X. Qian, P.-X. Hou, H.-M. Cheng, C. Liu and F. Li, *ACS Nano*, 2016, **10**, 8676-8682.

242. B. Papandrea, X. Xu, Y. Xu, C.-Y. Chen, Z. Lin, G. Wang, Y. Luo, M. Liu, Y. Huang and L. Mai, *Nano Research*, 2016, **9**, 240-248.
243. W. Zhou, X. Xiao, M. Cai and L. Yang, *Nano Letters*, 2014, **14**, 5250-5256.
244. A. T. Lawal and G. G. Wallace, *Talanta*, 2014, **119**, 133-143.
245. M. Wang, J. Wang, Y. Hou, D. Shi, D. Wexler, S. D. Poynton, R. C. Slade, W. Zhang, H. Liu and J. Chen, *ACS Applied Materials & Interfaces*, 2015, **7**, 7066-7072.
246. G. Li, J. Sun, W. Hou, S. Jiang, H. Yong and J. Geng, *Nature Communications*, 2016, **7**, 10601.
247. X. Hong, J. Jin, T. Wu, Y. Lu, S. Zhang, C. Chen and Z. Wen, *Journal of Materials Chemistry A*, 2017, **5**, 14775-14782.
248. X. L. Wei, M. F. And and A. J. Epstein, *Macromolecules*, 1999, **32**, 3114-3117.
249. F. Li, M. R. Kaiser, J. Ma, Z. Guo, H. Liu and J. Wang, *Energy Storage Materials*, 2018, **13**, 312-322.
250. J. Zhang, Y. Shi, Y. Ding, W. Zhang and G. Yu, *Nano Letters*, 2016, **16**, 7276-7281.
251. Y. Li, B. Shi, W. Liu, R. Guo, H. Pei, D. Ye, J. Xie and J. Kong, *Electrochimica Acta*, 2018, **260**, 912-920.
252. X. Zhou, F. Chen and J. Yang, *Journal of Energy Chemistry*, 2015, **24**, 448-455.
253. H. Li, Y. Wei, J. Ren, W. Zhang, C. Zhang and Y. Zhang, *Polymer*, 2018, **137**, 261-268.
254. P. Xin, B. Jin, H. Li, X. Lang, C. Yang, W. Gao, Y. Zhu, W. Zhang, S. Dou and Q. Jiang, *ChemElectroChem*, 2017, **4**, 115-121.
255. G. Ma, Z. Wen, J. Jin, Y. Lu, K. Rui, X. Wu, M. Wu and J. Zhang, *Journal of Power Sources*, 2014, **254**, 353-359.
256. Y. Liu, W. Yan, X. An, X. Du, Z. Wang, H. Fan, S. Liu, X. Hao and G. Guan, *Electrochimica Acta*, 2018, **271**, 67-76.
257. J. Xu, B. Jin, H. Li and Q. Jiang, *International Journal of Hydrogen Energy*, 2017, **42**, 20749-20758.
258. F. Yin, X. Liu, Y. Zhang, Y. Zhao, A. Menbayeva, Z. Bakenov and X. Wang, *Solid State Sciences*, 2017, **66**, 44-49.
259. J. B. Goodenough, *Accounts of Chemical Research*, 2012, **46**, 1053-1061.
260. B. Wang, W. Al Abdulla, D. Wang and X. Zhao, *Energy & Environmental Science*, 2015, **8**, 869-875.
261. L. Xue, S. V. Savilov, V. V. Lunin and H. Xia, *Advanced Functional Materials*, 2018, **28**, 1705836.
262. S. Evers and L. F. Nazar, *Accounts of Chemical Research*, 2012, **46**, 1135-1143.
263. A. Fotouhi, D. J. Auger, K. Propp, S. Longo and M. Wild, *Renewable and Sustainable Energy Reviews*, 2016, **56**, 1008-1021.
264. X. Liu, J. Q. Huang, Q. Zhang and L. Mai, *Advanced Materials*, 2017, **29**, 1601759.
265. Z. Sun, J. Zhang, L. Yin, G. Hu, R. Fang, H.-M. Cheng and F. Li, *Nature Communications*, 2017, **8**, 14627.
266. Y. Mi, W. Liu, X. Li, J. Zhuang, H. Zhou and H. Wang, *Nano Research*, 2017, **10**, 3698-3705.
267. S.-K. Lee, Y. J. Lee and Y.-K. Sun, *Journal of Power Sources*, 2016, **323**, 174-188.
268. Z. Lin, Z. Liu, N. J. Dudney and C. Liang, *ACS Nano*, 2013, **7**, 2829-2833.
269. Y. Yang, G. Zheng, S. Misra, J. Nelson, M. F. Toney and Y. Cui, *Journal of the American Chemical Society*, 2012, **134**, 15387-15394.

270. M. Yu, Z. Wang, Y. Wang, Y. Dong and J. Qiu, *Advanced Energy Materials*, 2017, **7**, 1700018.
271. J. Zhang, Y. Shi, Y. Ding, L. Peng, W. Zhang and G. Yu, *Advanced Energy Materials*, 2017, **7**, 1602876.
272. S. Meini, R. Elazari, A. Rosenman, A. Garsuch and D. Aurbach, *The journal of Physical Chemistry Letters*, 2014, **5**, 915-918.
273. G. Zhou, J. Sun, Y. Jin, W. Chen, C. Zu, R. Zhang, Y. Qiu, J. Zhao, D. Zhuo and Y. Liu, *Advanced Materials*, 2017, **29**, 1603366.
274. Y. Chen, S. Lu, J. Zhou, X. Wu, W. Qin, O. Ogoke and G. Wu, *Journal of Materials Chemistry A*, 2017, **5**, 102-112.
275. M. R. Kaiser, X. Liang, H.-K. Liu, S.-X. Dou and J.-Z. Wang, *Carbon*, 2016, **103**, 163-171.
276. V. Do, I. W. Nah, C. Lee, W. I. Cho and I. H. Oh, *Electrochimica Acta*, 2016, **210**, 1-6.
277. Z. W. Seh, H. Wang, P.-C. Hsu, Q. Zhang, W. Li, G. Zheng, H. Yao and Y. Cui, *Energy & Environmental Science*, 2014, **7**, 672-676.
278. C. Nan, Z. Lin, H. Liao, M.-K. Song, Y. Li and E. J. Cairns, *Journal of the American Chemical Society*, 2014, **136**, 4659-4663.
279. L. Wang, Y. Wang and Y. Xia, *Energy & Environmental Science*, 2015, **8**, 1551-1558.
280. F. Wu, H. Kim, A. Magasinski, J. T. Lee, H. T. Lin and G. Yushin, *Advanced Energy Materials*, 2014, **4**, 1551-1558.
281. Z. W. Seh, H. Wang, N. Liu, G. Zheng, W. Li, H. Yao and Y. Cui, *Chemical Science*, 2014, **5**, 1396-1400.
282. C. Zu, M. Klein and A. Manthiram, *The Journal of Physical Chemistry Letters*, 2014, **5**, 3986-3991.
283. J. Y. Koh, M.-S. Park, E. H. Kim, B. O. Jeong, S. Kim, K. J. Kim, J.-G. Kim, Y.-J. Kim and Y. Jung, *Journal of The Electrochemical Society*, 2014, **161**, A2133-A2137.
284. C. Zheng, S. Niu, W. Lv, G. Zhou, J. Li, S. Fan, Y. Deng, Z. Pan, B. Li and F. Kang, *Nano Energy*, 2017, **33**, 306-312.
285. J. Sun, Y. Sun, M. Pasta, G. Zhou, Y. Li, W. Liu, F. Xiong and Y. Cui, *Advanced Materials*, 2016, **28**, 9797-9803.
286. Z.-L. Xu, J.-K. Kim and K. Kang, *Nano Today*, 2018, **19**, 84-107.
287. Z. W. Seh, Y. Sun, Q. Zhang and Y. Cui, *Chemical Society Reviews*, 2016, **45**, 5605-5634.
288. A. Manthiram, S. H. Chung and C. Zu, *Advanced Materials*, 2015, **27**, 1980-2006.
289. S. Rehman, K. Khan, Y. Zhao and Y. Hou, *Journal of Materials Chemistry A*, 2017, **5**, 3014-3038.
290. X. Yang, X. Li, K. Adair, H. Zhang and X. Sun, *Electrochemical Energy Reviews*, 2018, **1**, 239-293.
291. J. Brückner, S. Thieme, F. Böttger‐Hiller, I. Bauer, H. T. Grossmann, P. Strubel, H. Althues, S. Spange and S. Kaskel, *Advanced Functional Materials*, 2014, **24**, 1284-1289.
292. Y. Tsao, M. Lee, E. C. Miller, G. Gao, J. Park, S. Chen, T. Katsumata, H. Tran, L.-W. Wang and M. F. Toney, *Joule*, 2019, **3**, 872-884.
293. S. Liang, Y. Xia, C. Liang, Y. Gan, H. Huang, J. Zhang, X. Tao, W. Sun, W. Han and W. Zhang, *Journal of Materials Chemistry A*, 2018, **6**, 9906-9914.

294. X. Wang, X. Bi, S. Wang, Y. Zhang, H. Du and J. Lu, *ACS Applied Materials & Interfaces*, 2018, **10**, 16552-16560.
295. D. Su, D. Zhou, C. Wang and G. Wang, *Advanced Functional Materials*, 2018, **28**, 1800154.
296. Q. Pang, A. Shyamsunder, B. Narayanan, C. Y. Kwok, L. A. Curtiss and L. F. Nazar, *Nature Energy*, 2018, **3**, 783.
297. R.-c. Xu, X.-h. Xia, X.-l. Wang, Y. Xia and J.-p. Tu, *Journal of Materials Chemistry A*, 2017, **5**, 2829-2834.
298. R.-c. Xu, X.-h. Xia, S.-h. Li, S.-z. Zhang, X.-l. Wang and J.-p. Tu, *Journal of Materials Chemistry A*, 2017, **5**, 6310-6317.
299. B. D. Adams, E. V. Carino, J. G. Connell, K. S. Han, R. Cao, J. Chen, J. Zheng, Q. Li, K. T. Mueller and W. A. Henderson, *Nano Energy*, 2017, **40**, 607-617.
300. G. G. Eshetu, X. Judez, C. Li, O. Bondarchuk, L. M. Rodriguez-Martinez, H. Zhang and M. Armand, *Angewandte Chemie International Edition*, 2017, **56**, 15368-15372.
301. F. Wu, J. T. Lee, N. Nitta, H. Kim, O. Borodin and G. Yushin, *Advanced Materials*, 2015, **27**, 101-108.
302. T. Yang, X. Wang, D. Wang, S. Li, D. Xie, X. Zhang, X. Xia and J. Tu, *Journal of Materials Chemistry A*, 2016, **4**, 16653-16660.
303. Y. Peng, Y. Zhang, Z. Wen, Y. Wang, Z. Chen, B.-J. Hwang and J. Zhao, *Chemical Engineering Journal*, 2018, **346**, 57-64.
304. M. Yu, Z. Wang, Y. Wang, Y. Dong and J. Qiu, *Advanced Energy Materials*, 2017, **7**, 1700018.
305. Y. Kim, H. Han, Y. Noh, J. Bae, M. H. Ham and W. B. Kim, *ChemSusChem*, 2019, **12**, 824-829.
306. F. Wu, J. T. Lee, E. Zhao, B. Zhang and G. Yushin, *ACS nano*, 2015, **10**, 1333-1340.
307. H. Yan, H. Wang, D. Wang, X. Li, Z. Gong and Y. Yang, *Nano Letters*, 2019, **19**, 3280-3287.
308. J. He, Y. Chen and A. Manthiram, *Advanced Energy Materials*, 2019, **9**, 1900584.
309. L. Chen, Y. Liu, F. Zhang, C. Liu and L. L. Shaw, *ACS Applied Materials & Interfaces*, 2015, **7**, 25748-25756.
310. F. Wu, T. P. Pollard, E. Zhao, Y. Xiao, M. Olguin, O. Borodin and G. Yushin, *Energy & Environmental Science*, 2018, **11**, 807-817.
311. C. Chen, D. Li, L. Gao, P. P. R. Harks, R.-A. Eichel and P. H. Notten, *Journal of Materials Chemistry A*, 2017, **5**, 1428-1433.
312. M. R. Kaiser, Z. Han, J. Liang, S.-X. Dou and J. Wang, *Energy Storage Materials*, 2019, 19,1-15.
313. B. Bertheville, H. Bill and H. Hagemann, *Journal of Physics: Condensed Matter*, 1998, **10**, 2155.
314. J. Wang, L. Liu, S. Chou, H. Liu and J. Wang, *Journal of Materials Chemistry A*, 2017, **5**, 1462-1471.
315. L. Chen, Y. Z. Liu, M. Ashuri, C. H. Liu and L. L. Shaw. *Journal of Materials Chemistry A*, 2014, **2**, 18026-18032.
316. K. Han, J. M. Shen, C. M.Hayner, H. Q. Ye, M. C. Kung, H. H. Kung, *Journal of Power Sources*, 2014, **251**, 331-337.
317. M. Wu, Y. Cui, Y. Z. Fu, *ACS Applied Materials & Interfaces*, 2015, **7**, 21479-21486.

318. C. Wang, X. S. Wang, Y. Yang, A. Kushima, J. T. Chen, Y. H. Huang, J. Li, *Nano Letter*, 2015, **15**, 1796-1802.
329. Z. Yang, J. Guo, S. K. Das, Y. Yu, Z. Zhou, H. D. Abruña, L. A. Archer, *Journal of Materials Chemistry A*, 2013, **1**, 1433-1440.
320. S. Jeong, D. Bresser, D. Buchholz, M. Winter, S. Passerini, *Journal of Power Sources*, 2013, **235**, 220-225.

APPENDIX A: LIST OF PUBLICATIONS

1. **F. Li**, M. R. Kaiser, J. M. Ma, Z. P. Guo, H. K. Liu and J. Z. Wang, Free-standing Sulfur-Polypyrrole Cathode in Conjunction with Polypyrrole-Coated Separator for Flexible Li-S Batteries, Energy storage materials, 2018, 13, 312-322.

2. **F. Li**, J. M. Ma, Y. Y. Hou, T. F. Zhou, W. H. Lai, J. Chen, Z. P. Guo, H. K. Liu and J. Z. Wang, Uniform Polypyrrole Layer Coated Sulfur/Graphene Aerogel via Vapor Phase Deposition Technique as Cathode Material for Li-S Batteries. (To be submitted)

3. **F. Li**, M. R. Kaiser, H. K. Liu and J. Z. Wang, Facile and Up-scaled Synthesis of Li_2S-Polypyrrole Hybrid as cathode for Lithium-Sulfur Batteries. (To be submitted)

4. **F. Li**, H. K. Liu and J. Z. Wang, A Conductive Polymer Derived N-doped Carbon Nanofibers Supported Li_2S Coating Layer for Li-S Batteries with High Mass Loading. (To be submitted)